MRI-BASED ASSESSMENT OF CORTICAL BONE MATRIX AND MINERAL PROPERTIES IN A CLINICAL SETTING

Xia Zhao

A DISSERTATION

in

Bioengineering

Presented to the Faculties of the University of Pennsylvania

in

Partial Fulfillment of the Requirements for the

Degree of Doctor of Philosophy

2019

Supervisor of Dissertation

_____

Felix W. Wehrli, PhD

Professor of Radiology

Co-Supervisor of Dissertation

_____

Hee Kwon Song, PhD

Associate Professor of Radiology

Graduate Group Chairperson

_____

Ravi Radhakrishnan, Ph.D.

Professor of Bioengineering

Dissertation Committee

Mona Al Mukaddam, MD, Assistant Professor of Clinical Medicine

Ravinder Reddy, PhD, Professor of Radiology

Chamith S. Rajapakse, PhD, Assistant Professor of Radiology

Hee Kwon Song, PhD, Associate Professor of Radiology

Felix W. Wehrli, PhD, Professor of Radiology

TO MY FAMILY

To mom and dad: I am deeply grateful to you for everything you had to do or go through in order for me to stand where I am today. You will be impressed by how I have been transformed during this process. Remember, you are the last ones I would like to disappoint in this world. This work is dedicated to you. I love you.

To my maternal grandparents: Although both of you passed away when I was a little child, your words and principles kept influencing me up till today. I hope that you will be pleased to see how I lived my life and proud of what I have become. I miss you.

To my parental grandparents: It's a great pity that I was not able to stay by your sides during the last few years of your lives. I just want you to know that I made it and am on my way home soon. I miss you, too.

To my cat Dun Dun: The unexpected encounter on April 9, 2014 has made you an important part of my life ever since. Thank you for your company along the way. Thank you for all the sweet memories. I love you.

ACKNOWLEGEMENT

I hereby express my upmost gratitude to my thesis advisor Dr. Hee Kwon Song. If it were not for him, I might never have the opportunity to study and work at such a world-class university and prestigious research institution in the first place. I still remember that the funding Dr. Song used to recruit me into the PhD program was originally budgeted for hiring a post-doctoral scholar, who would have been more competent and productive than I was. However, he decided to give that chance to me, for which I will be thankful for the rest of my life. Over the years of PhD training, I was influenced not only by his profound knowledge in MRI, but also by his virtues. The modesty, patience and tolerance that embodied in the way he treated people (especially me) set up a role model for me and helped shape my personality today.

My most sincere appreciation also goes to my thesis advisor Dr. Felix W. Wehrli. I do not only respect Dr. Wehrli as a learned scholar, but also admire him as a knowledgeable senior. His enormous enthusiasm about work taught me the attitude toward science as well as my future career, while his broad interests covering sports, arts, history etc. taught me the attitude toward life. In addition to the guidance I received from him during our regular project meetings, I enjoyed all our conversations about other topics very much too, be it on the porch of his home, on the lunch table or in his small yet well-decorated office.

Except for providing me with the opportunity to study and work in the Laboratory of Structural, Physiologic and Functional Imaging, Dr. Wehrli and Dr. Song also encouraged me to attend the international conferences every year and generously

supported the trips. The experiences of presenting in front of and interacting with researchers and experts from all over the globe honed my presentation skills and at the same time boosted my confidence. Furthermore, traveling around the world enriched my life experience while exposing to different cultures broadened my point of view. If the disciplinary knowledge, the attitude to research instilled in me will mostly benefit my future work, the values of the principles I learned from them and those unique experiences I had because of them will be reflected in all aspects of my life.

I also want to express my sincere gratitude to Dr. Ravinder Reddy, Dr. Mona Al Mukaddam and Dr. Chamith Rajapakse, for sparing precious time from their daily duty to serve on my thesis committee, and offering professional insights each time we met to make this work more sophisticated.

I would like to take this opportunity to thank Dr. Hyunyeol Lee as well, for all the inspiring discussions happened during our lunch and the joyful collaboration experience. Our lunchtime was one of the most delightful moments in a day. Thank Holly Stefanow, the associate director of our lab, for all the help she gave me and cat stories she shared with me.

ABSTRACT

MRI-BASED ASSESSMENT OF CORTICAL BONE MATRIX AND MINERAL PROPERTIES IN A CLINICAL SETTING

Xia Zhao

Felix W. Wehrli, Ph.D.

Hee Kwon Song, Ph.D.

As a pathological condition primarily afflicting the elderly, osteoporosis is becoming more prevalent with today's lengthened life expectancy. Osteoporosis-associated fractures are dangerous, often associated with lethal complications, and impose a huge economic burden on society. Unfortunately, current techniques used to diagnose the disease cannot provide reliable fracture risk prediction, as they rely upon apparent bone mineral density (BMD) only.

Recent advances in short echo time (TE) imaging have made it possible to examine different properties of bone with magnetic resonance imaging (MRI). Water bound to the collagen matrix (bound water, BW), water residing in the pore space (pore water, PW), and phosphorus (^{31}P) in bone mineral crystals have previously been proposed as surrogate markers for bone matrix density, porosity and mineral density, to be quantitatively imaged with either ^{1}H or ^{31}P ultra-short TE (UTE) or zero TE (ZTE) sequence.

In this dissertation, an integrated MRI protocol measuring both bone matrix and mineral properties *in vivo* was first designed and tested with clinical hardware. MRI-derived PW was negatively correlated with high resolution peripheral quantitative computed tomography (HR-pQCT) derived BMD, while bone mineral content based on MRI-derived phosphorus density was positively correlated with that based on HR-pQCT

BMD. Second, *in vivo* bone phosphorus relaxation times were studied in a small cohort of healthy volunteers (aged 29 to 65). The relative invariability of relaxation properties obviated the need for individual measurements in this healthy cohort. Third, gradient imperfections were found to introduce errors in UTE image-based bone water quantification and to undermine measurement agreement across scanners, therefore requiring correction. Finally, the suggested protocol was applied in an ongoing osteoporosis treatment study. Expected observations — elevated pore water, lowered bound water and phosphorus densities — were observed in the patient group relative to healthy controls in limited baseline data acquired thus far.

In conclusion, this dissertation proves the feasibility of measuring bone matrix and mineral surrogates in a clinical setting, and may aid in better predicting osteoporotic fractures.

TABLE OF CONTENTS

LIST OF TABLES

LIST OF FIGURES

PREFACE

Chapter 3 has been published as: Xia Zhao, Hee Kwon Song, Alan C. Seifert, Cheng Li, Felix W. Wehrli. Feasibility of assessing bone matrix and mineral properties *in vivo* by combined solid-state ^{1}H and ^{31}P MRI. PLOS ONE 12(3): e0173995. DOI: 10.1371/journal.pone.0173995

Chapter 4 has been published as: Xia Zhao, Hee Kwon Song, Felix W. Wehrli, *In vivo* bone ^{31}P relaxation times and their implications on mineral quantification. Magnetic Resonance in Medicine, 2018(80): 2514-2524. DOI: 10.1002/mrm.27230

Chapter 5 will be submitted to Magnetic Resonance in Medicine as: Xia Zhao, Hyunyeol Lee, Hee Kwon Song, Felix W. Wehrli. Impact of gradient imperfections on bone water quantification with UTE.

Xia Zhao

2019-05-23

CHAPTER 1: CORTICAL BONE PHYSIOLOGY AND PATHOLOGY

1.1 Cortical Bone Anatomy and Physiology

1.1.1 Macrostructure of Bone

As major components of the musculoskeletal system, most bones are comprised of a trabecular (or spongy, or cancellous) portion and a cortical (or compact) portion (**Figure 1.1**). Trabecular bone consists of trabeculae, in the shape of plates and rods organized in the direction of stress experienced by the bone, and is usually found on the inside of flat bones and at the ends of weight bearing bones. Cortical bone, on the other hand, forms the diaphysis of long bones and the exterior of other bones. The exact distribution and proportion of the two vary depending upon the overall function of the bone in question [1].

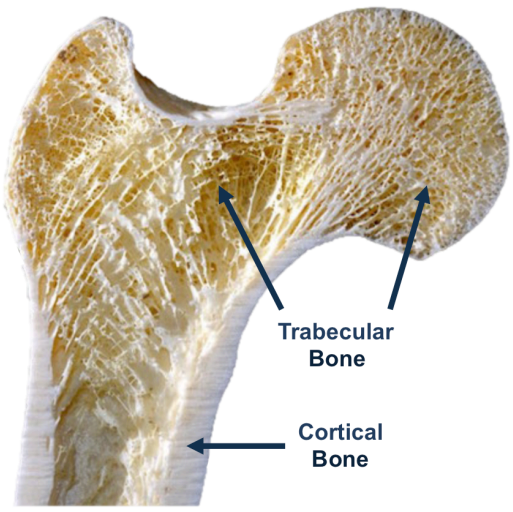

Figure 1.1 Photo showing the trabecular portion and cortical portion of a human femur at the metaphysis and epiphysis.

1.1.2 Microstructure of Cortical Bone

Cortical bone is composed of smaller structural and functional units called osteon (**Figure 1.2**). Osteons are made of concentric layers of mineralized collagenous sheets (lamellae), forming the Haversian canal at the center. Haversian canals house the blood vessels, lymph vessels and nerves that supply the bone tissue. Running perpendicular to Haversian canals, are Volkmann's canals, which connect osteons with each other and to the periosteum (exterior surface of cortical bone) and endosteum (interior surface of cortical bone). The many small holes interspersed within and between osteons are called lacunae. Lacunae accommodate osteocytes, a type of bone cell that develops from osteoblasts (bone forming cells, introduced in **Section 1.1.4**) trapped within the structure during the bone formation. The relationship between osteons, Haversian canals, and lacunae can be visualized in the microscopic image in **Figure 1.3**. Lacunae are connected to each other, and to the Harversian canal, via smaller canals termed canaliculi, constructing the lacuno-canalicular system. The lacuno-canalicular system nourishes osteocytes with nutrients and removes the metabolic wastes they produce. This system also allows for communication between osteocytes, believed to be the mechanism by which bone senses mechanical stimuli [2].

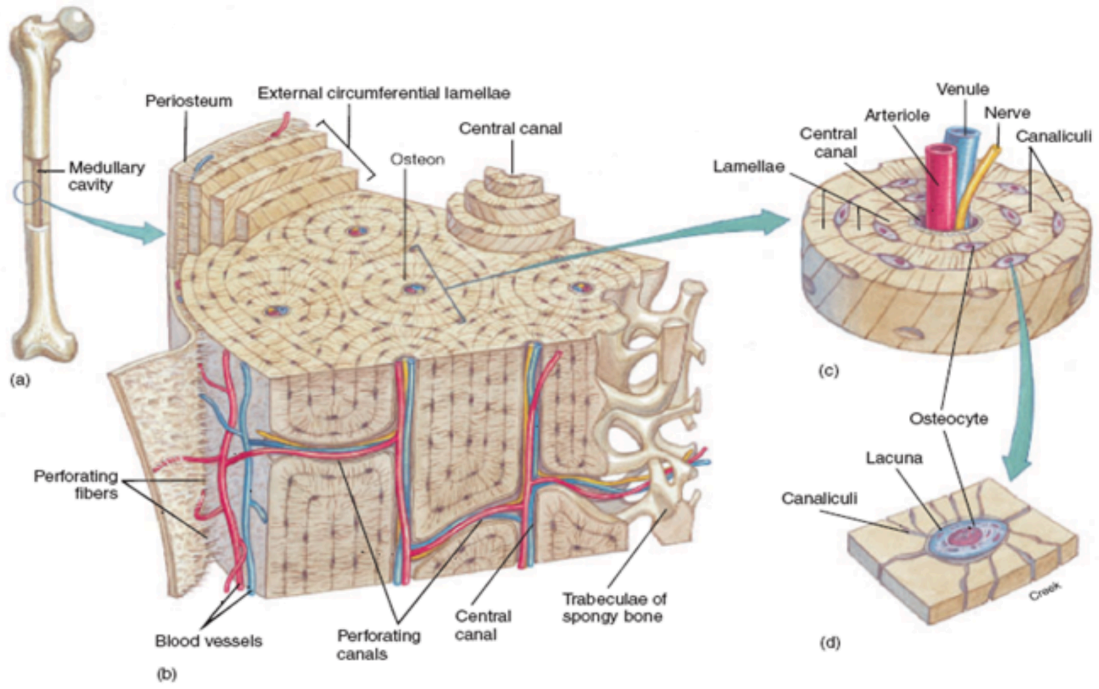

Figure 1.2 Hierarchical structure of human cortical bone [3].

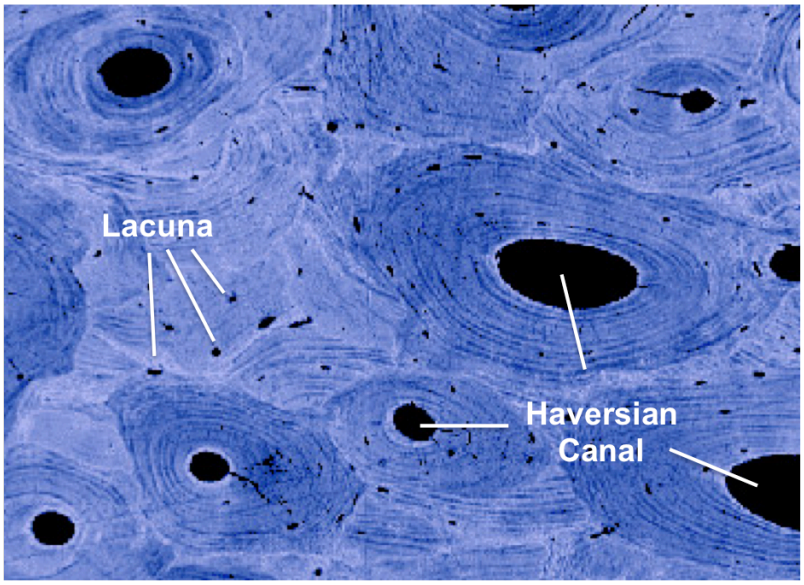

Figure 1.3 Microscopic image of human cortical bone [4]. Osteons are constructed from layers of lamella, forming the Haversian canal at the center. Lacunae are interspersed within and between osteons.

1.1.3 Composition of Bone Matrix

The non-cellular portion of bone breaks down further into two major constituents, the organic phase (the bone matrix) — mainly type I collagen, and the inorganic phase (often referred to as bone mineral) — hydroxyapatite (HA). Collagen accounts for about 20% to 40% of weight in adult bone while mineral accounts for another 50% to 70% [1]. The remaining mass is attributed to other substances such as cells and water (**Figure 1.4**).

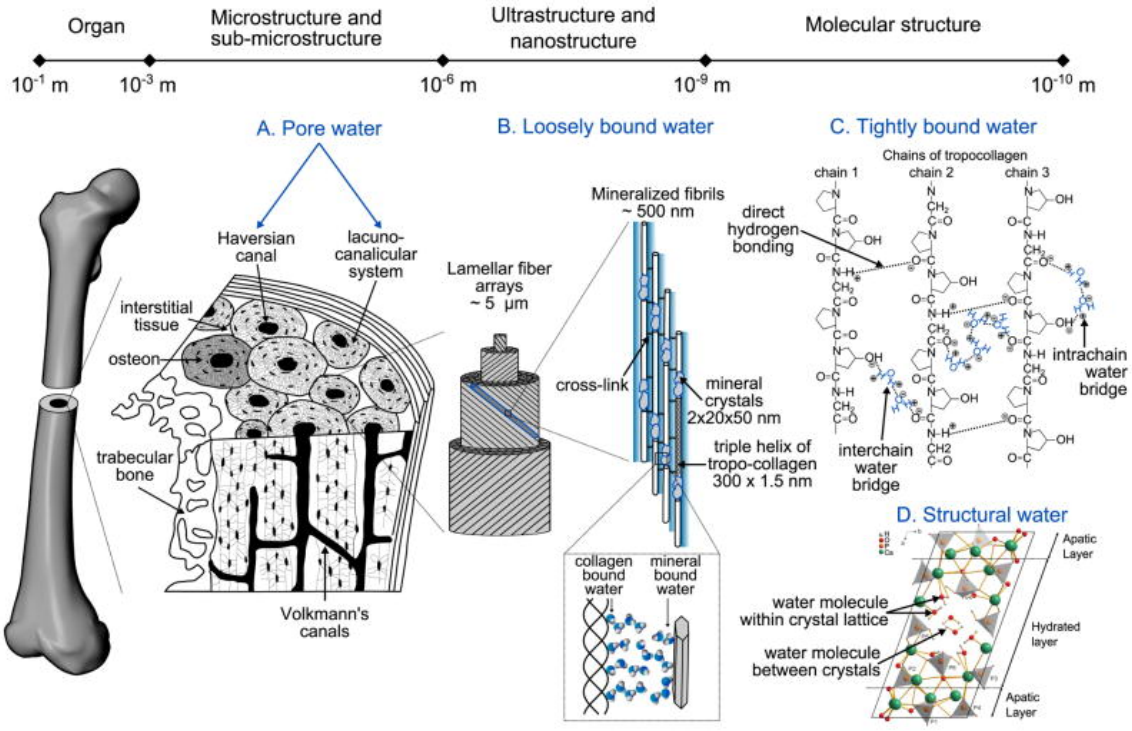

Figure 1.4 Anatomy of cortical bone matrix [5]. Three amino acids form a collagen molecule, by binding to each other via covalent bonds to create collagen fibril. Fibrils are subsequently organized into layers of lamella that construct individual osteons, the structural units of cortical bone. Mineral crystals are interspersed in the gaps between the collagen molecules to provide bone with rigidity. Water molecules bound to the matrix further reinforce the mechanical strength of this structure.

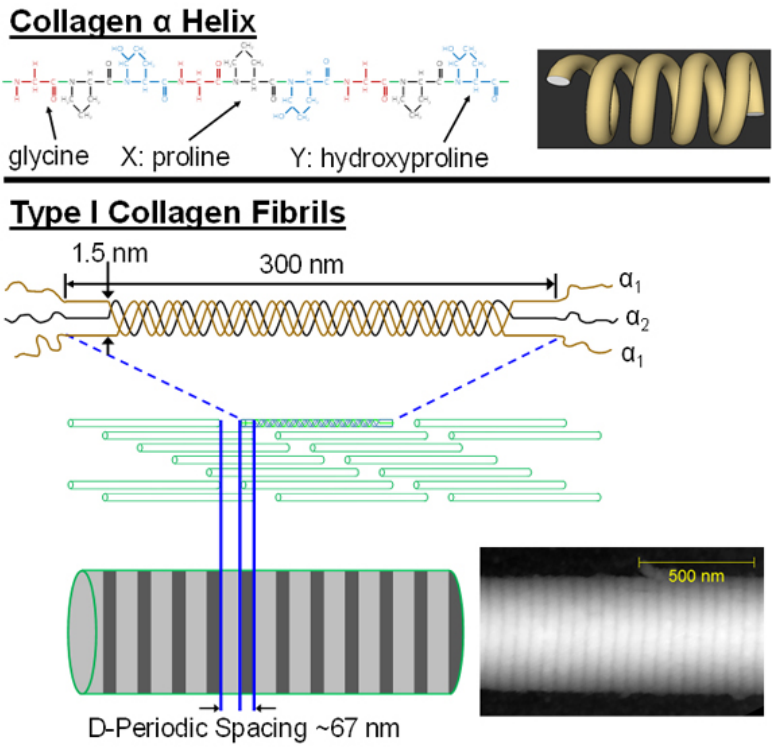

Figure 1.5 Structural hierarchy of collagen fiber [6]. Each collagen fibril consists of three amino acids intertwined with each other to form a triple helix. A collagen fiber is composed of a number of such fibrils. Collagen fibrils stack together in order to give the fiber its characteristic periodic spacing pattern under microscope.

As the fundamental building block of the matrix, each collagen fibril is made up of three amino acids (**Figure 1.5**). The amino acids are intertwined into triple helix structures that are attached to each other via covalent bonds to form fibers, which are further organized into a regular pattern to construct the matrix (**Figure 1.4**). The mineral crystals embedded in the spaces between collagen fibrils (**Figure 1.4**) are composed of a crystalline complex of calcium and phosphate (**Figure 1.6**) and store approximately 99% of the calcium and 80% of the phosphorus in the human body [7]. Collagen fiber provides bone with elasticity and flexibility while mineral crystal provides stiffness and rigidity [1]. In

addition, water molecules bound to the matrix contribute to the ductility and plasticity of bone [5]. Collectively, these structural components provide bone with its characteristic mechanical property.

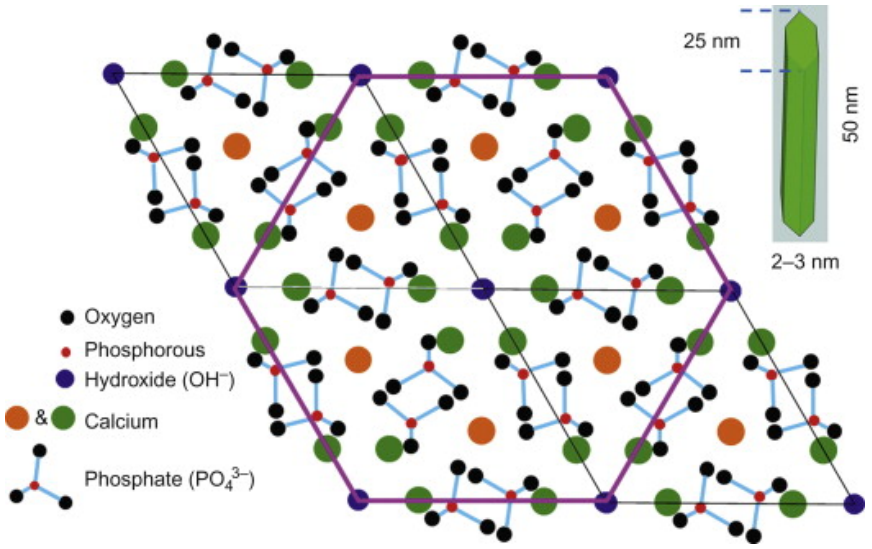

Figure 1.6 The major constituent of bone mineral is non-stoichiometric calcium apatite [6].

1.1.4 Bone Remodeling

Rather than being quiescent, bone tissue undergoes constant remodeling to repair micro-fractures from daily activity and in response to external stimuli such as mechanical stress and impact [1]. Two types of bone cells are involved in this process, osteoblasts and osteoclasts. Remodeling begins with the osteoclast dissolving the old bone tissue (bone resorption), followed by osteoblasts laying down the new bone matrix (bone deposition). The newly deposited matrix subsequently undergoes a primary (~ several weeks) and a secondary (~ several months) mineralization process to reach full mechanical competence [8]. The resorption of old bone tissue and deposition of new bone tissue ordinarily exist at a dynamic equilibrium to maintain total bone volume. However, in osteoporosis, the rate

of resorption can exceed that of deposition, leading to net loss of bone tissue and physical fragility.

1.2 Osteoporosis

1.2.1 Symptoms, Causes, and High Risk Population

Osteoporosis is a pathological condition characterized by loss of bone mass and compromised mechanical strength. Morphologically, it manifests as overall thinning of the cortex, trabecularization of the endosteal surface, and expansion of the pore system. Concurrently, increased turnover rate also results in less time for newly generated bone tissue to undergo proper secondary mineralization, As a consequence, a disproportionately large loss in strength results [9].

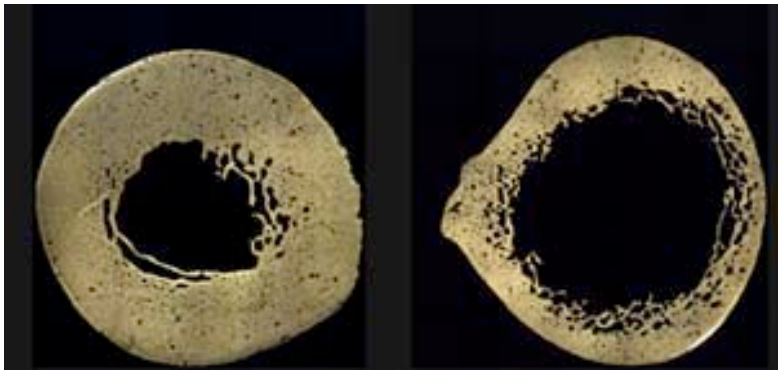

Figure 1.7 Cross section at the mid-shaft of the femur of an 84-year old female with advanced osteoporosis (right), compared to that of a healthy 17-year old female (left) [10].

A number of factors may contribute to osteoporosis, including genetic diseases, malnutrition, or hormonal abnormalities. Menopause, which typically occurs in women near the age of 50, causes depletion of estrogen, a hormone that suppresses osteoclastic activity while promoting osteoblastic activity [11]. This process breaks the subtle balance

between bone resorption and deposition, and eventually leads to a net loss of bone tissue. As such, women are more vulnerable to osteoporosis than are men [12].

1.2.2 Morbidity, Mortality and Economic Impact

Osteoporosis is a major health issue in the industrialized world. Since the disorder primarily afflicts the elderly, prevalence continues to grow in conjunction with increased life expectancy. Based on an overall 10.3% prevalence in 2010 in a population of 99 million aged 50 years or older, 10.2 million Americans were estimated to have the disease [12]. Further, the population over 50 years of age and with low bone mass — often the precursor of osteoporosis — is projected to reach 120 million in less than ten years from today [13]. Major consequences of osteoporosis include fractures of the vertebrae, wrist, humerus, and hip. Among these, fractures of the hip, which often involve a break at the femoral neck, are particularly traumatic. For many elderly people, a hip fracture may be life threatening. A number of studies have reported a substantial increase in mortality in the years following a hip fracture [14-17]. Worldwide, more than 200 million people were estimated to suffer from osteoporotic hip fractures [18]. In Europe and the United States, 30% of women are reported to be osteoporotic, while 40% of post-menopausal women and 30% of men are expected to experience an osteoporotic fracture during their lifetime [12, 19, 20]. The total cost of treatment was more than $19 billion in 2005 with this number projected to increase by 50% in 20 years [21].

1.3 Current Clinical Diagnosis Modalities

Currently, the standard diagnostic modality for osteoporosis is dual-energy x-ray absorptiometry (DXA). DXA relies on areal bone mineral density (BMD) at specific

anatomical locations, with the spine and hip being the most frequent exam sites. A BMD T-score equal to or lower than -2.5 is regarded as clinically indicative for osteoporosis [22]. However, this technique has several limitations. First, its inability to discern between bone tissue and pore space prevents it from reflecting the extent of porosity or the true degree of mineralization of bone (DMB) — mass of mineral per unit volume of matrix. Second, the two-dimensional (2D) projection nature of DXA subjects results of the exam to bias from bone size. Further, bone strength is a comprehensive outcome of a number of factors of which BMD is just one. So it is not surprising that DXA has a low fracture risk prediction accuracy — only 44% of non-vertebral fractures were found to occur in women categorized as osteoporotic by DXA [23]. In addition, the density-based DXA may also mistake osteoporosis for demineralizing disorders, which have completely different pathologies and require different treatment plans. Peripheral quantitative computed tomography (pQCT) is a technique that reports volumetric BMD based on three-dimensional (3D) projection images. The result is therefore not affected by bone shape and size [24]. The technique does visualize porosity to some extent although its power is limited to large pores only. Moreover, the increased amount of ionizing radiation patients are exposed to makes it unfavorable for repeated use in monitoring treatment response. Finally, although bone biopsy can determine both porosity and mineralization, it is not suitable for repeated use either due to the inherent invasiveness. Therefore, a technique able to accurately and non-invasively evaluate both the matrix and mineral phases of bone *in vivo* would be highly desirable.

The non-invasive nature and multi-nuclei imaging ability of magnetic resonance imaging (MRI) renders it a potential alternative. It has been shown that surrogates of bone

porosity [25, 26] and matrix density [27-30] can be quantitatively evaluated *in vivo* with solid-state ^{1}H MRI, while quantification of bone mineral using solid-state ^{31}P MRI has been shown in animal models [31-33] and human specimens [28]. The ratio between MRI-derived phosphorus and the matrix surrogate could even provide an indirect measure of true mineralization. Information on these different aspects of bone property might potentially lead to more reliable prediction of osteoporotic fracture risk.

CHAPTER 2: INTERROGATION OF BONE WITH MAGNETIC RESONANCE IMAGING

2.1 Magnetic Resonance Imaging of Bone

2.1.1 Principle of MRI

An MRI experiment begins by placing the object being imaged inside the scanner's main magnet, where the strong magnetic field (B_0) aligns nuclear moments of individual nuclei to form bulk magnetizations [34]. A radio frequency magnetic field (RF pulse, often referred to as B_1) oscillating at the Larmor frequency of the target nucleus (most commonly ^1H in clinical applications) is applied, perpendicular to the main magnetic field, to flip part of the magnetizations into transverse plane (excitation) such that they rotate about the main field. Such rotation induces an alternating current electric signal in the receiving coils, as governed by Faraday's law. In order to identify spatial locations of these nuclei, a set of gradient fields (encoding gradient) are superimposed on the main magnetic field to vary its strength in a spatially dependent manner. As a result, magnetizations from different locations precess at different frequencies, which is reflected in the frequencies and phases of the signal they produce. The electric signal induced in the receiving coils is subsequently digitized and collected through an analog to digital converter (ADC), forming the MRI raw data known as k-space. This entire sequence of hardware events, including application of the RF pulse, encoding gradients and the ADC, is termed a pulse sequence. A typical 3D Cartesian MRI sequence diagram is shown in **Figure 2.1**. Mathematically, the spatial distribution of nuclear spins within the imaged object and k-space are associated by Fourier transform, as illustrated in **Figure 2. 2**.

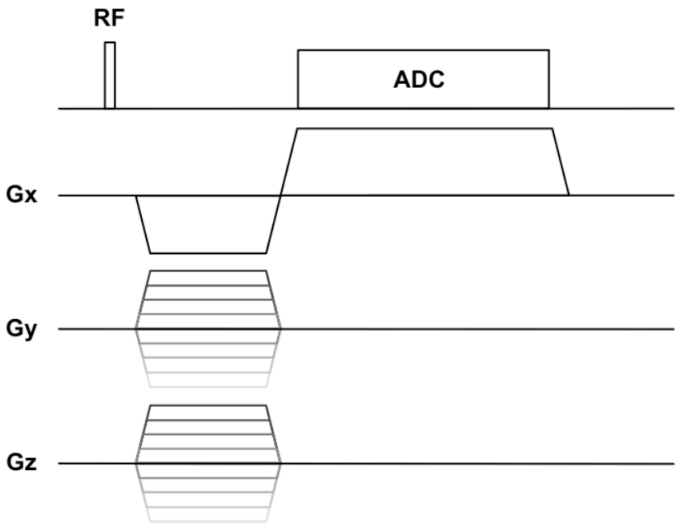

Figure 2.1 Diagram of a typical 3D Cartesian MRI sequence. Magnetizations are first excited by the RF pulse into transverse plane, where they rotate at spatially varying frequencies determined by encoding gradients (Gx, Gy and Gz) to produce signals with characteristic frequencies and phases, which are subsequently collected following digitization (ADC).

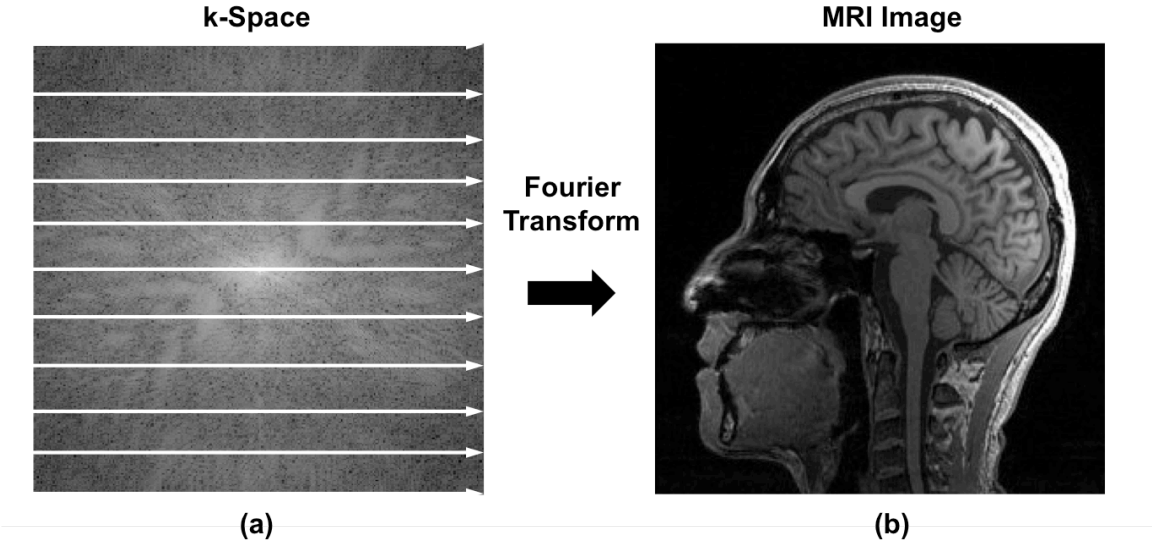

Figure 2.2 a) k-Space and b) MRI image are reciprocal spaces associated by the Fourier transform.

2.1.2 Time Constant T_1, T_2 and T_2*

The flipping of bulk magnetization by an RF pulse is equivalent to decomposing it into two orthogonal components: one perpendicular to and rotating about the main magnetic field (transverse magnetization) to create the MRI signal, the other remaining parallel to the main field (longitudinal magnetization). The exact amount of each component is dependent upon the flip angle (FA). Longitudinal magnetization tends to recover back to its original magnitude exponentially at a rate determined by time constant T_1 (longitudinal relaxation time), the time it takes for longitudinal magnetization to recover from zero to 63% of its original length (**Figure 2.3**) [35]. The transverse magnetization tends to decay away exponentially with time constant T_2 (transverse relaxation time), the time it takes for the transverse magnetization to reduce to 37% of its original value (**Figure 2.4**) [35]. The recovery of longitudinal magnetization and decay of transverse magnetization are termed longitudinal (or T_1) relaxation and transverse (or T_2) relaxation respectively. **Table 2.1** summarizes typical T_1 and T_2 values measured at 1.5 T and 3 T field strengths. T_2 relaxation occurs as a resultant loss of phase coherence (or dephasing) of spins within the system. In reality, however, the signal lifetime is significantly shorter than T_2 predicts because of factors such as main field inhomogeneity and susceptibility-induced local field distortion, [36], and is thus described by a more aggressive T_2* (effective transverse relaxation time) exponential decay as shown in **Figure 2.4**. The time from RF excitation to the collection of an echo is defined as echo time (TE), which is typically on the order of milliseconds in clinical MRI systems. A k-space is composed of multiple echoes as demonstrated in **Figure 2.2**, where each echo is represented by an arrow. Since the MRI signal progressively attenuates following excitation due to T_2 or

T_2* decay, the k-space is usually filled in with multiple excitations-acquisition cycles instead of all at once. The interval between two successive excitations is called repetition time (TR).

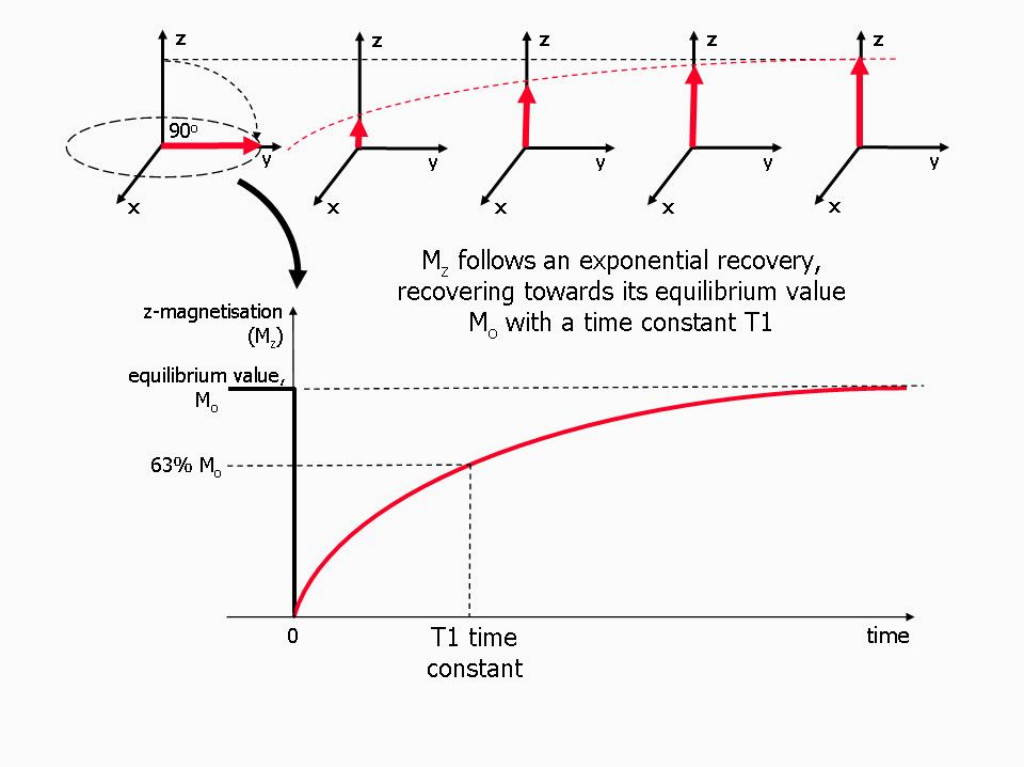

Figure 2.3 Illustration of T_1 relaxation [37]. Here, the entire magnetization is flipped into transverse plane by a 90° RF pulse, leaving no residual longitudinal magnetization at the end of the excitation. The longitudinal magnetization then recovers back to equilibrium value exponentially. The speed of the recovery process is determined by time constant T_1.

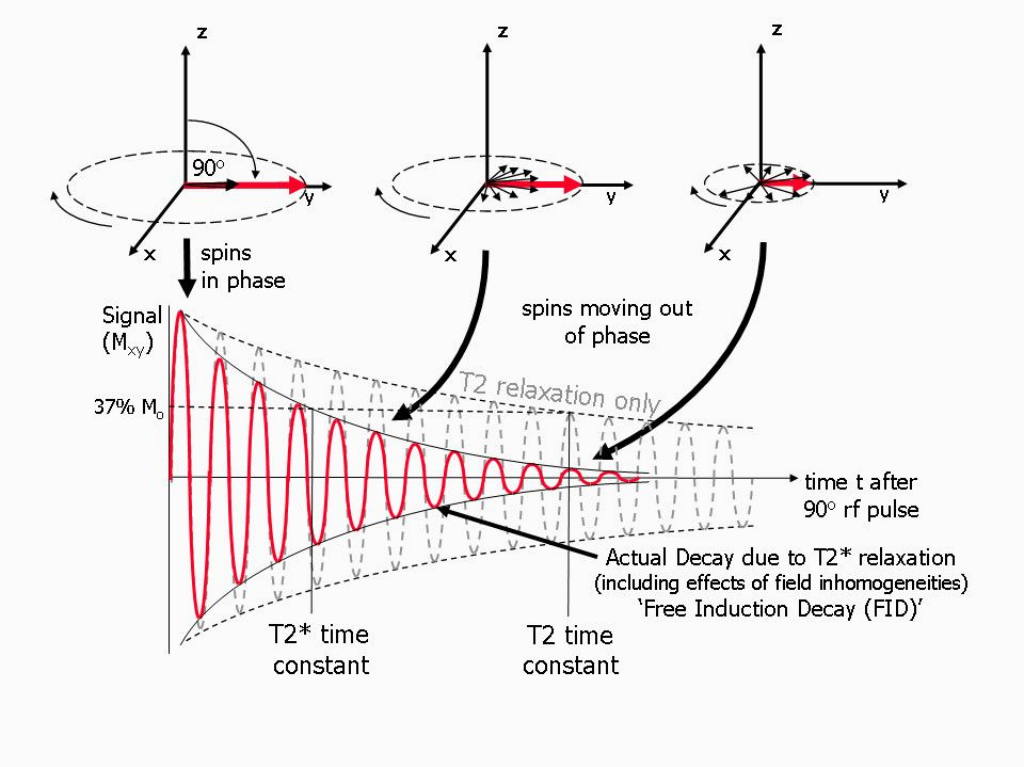

Figure 2.4 Illustration of T_2 and T_2* relaxation [37]. Immediately after being flipped into transverse plane by a 90° RF pulse, the transverse magnetization starts to decay as the constituent spins lose coherence, resulting in T_2 relaxation. Due to factors like field inhomogeneity and susceptibility-induced local field distortion, spins lose phase coherence more rapidly, leading to a more aggressive T_2* relaxation.

Table 2.1 T_1 and T_2 relaxation times of various human tissues measured at 1.5 T and 3 T [38].

Tissue	T_2 – 1.5 T (ms)	T_1 – 1.5 T (ms)	T_2 – 3 T (ms)	T_1 – 3 T (ms)
Liver	46 ± 6	576 ± 30	42 ± 3	812 ± 64
Skeletal Muscle	44 ± 6	1008 ± 20	50 ± 4	1412 ± 13
Heart	40 ± 6	1030 ± 34	47 ± 11	1471 ± 31
Kidney	55 ± 3	690 ± 30	56 ± 4	1194 ± 27
White Matter	72 ± 4	884 ± 50	69 ± 3	1084 ± 45
Gray Matter	95 ± 8	1124 ± 50	99 ± 7	1820 ± 114
Optic Nerve	77 ± 9	815 ± 30	78 ± 5	1083 ± 39
Spinal Cord	74 ± 6	745 ± 37	78 ± 2	993 ± 47
Blood	290 ± 30	1441 ± 120	275 ± 50	1932 ± 85

2.1.3 Surrogates for Bone Matrix and Mineral

Bone has very unfavorable relaxation properties compared to most human tissues. As illustrated by the proton (^{1}H) T_2 spectrum in **Figure 2.5**, three distinct pools of ^{1}H are readily identified: 50 μs < T_2 < 150 μs, corresponding to the collagen matrix itself; 150 μs < T_2 < 1 ms, corresponding to the water molecules bound to the collagen matrix (bound water, BW); and finally 1 ms < T_2 < 1 s, corresponding to the water molecules freely residing in the pore space (Haversian canal, Volkmann's canal and lacuno-canalicular system) within the matrix (pore water, PW). The bone matrix's extremely short T_2 is due to restricted molecular motion in the well-organized collagen structure, making it less efficient to average out the effect of local field inhomogeneity, and resulting in faster dephasing between spins and a consequent decay of transverse magnetization. Compared to the ^{1}H on collagen fiber, bound water has a certain degree of molecular motion that allows for a slightly longer T_2. Pore water has even more freedom of motion and therefore has the longest T_2 among the three. However, these values are still one to three orders of magnitude smaller than the T_2 of other tissues in human body (**Table 2. 1**) and are much shorter than the TE of clinical sequences. As a result, bone tissue always appears dark on conventional MRI images. Although directly capturing signal from bone matrix itself is restricted by hardware limitations of clinical MRI systems, the bound and pore water can be detected with special techniques. Earlier studies have demonstrated successful capture of the two water pools and their potential to serve as surrogates for matrix density and porosity of bone tissue, respectively [39, 40].

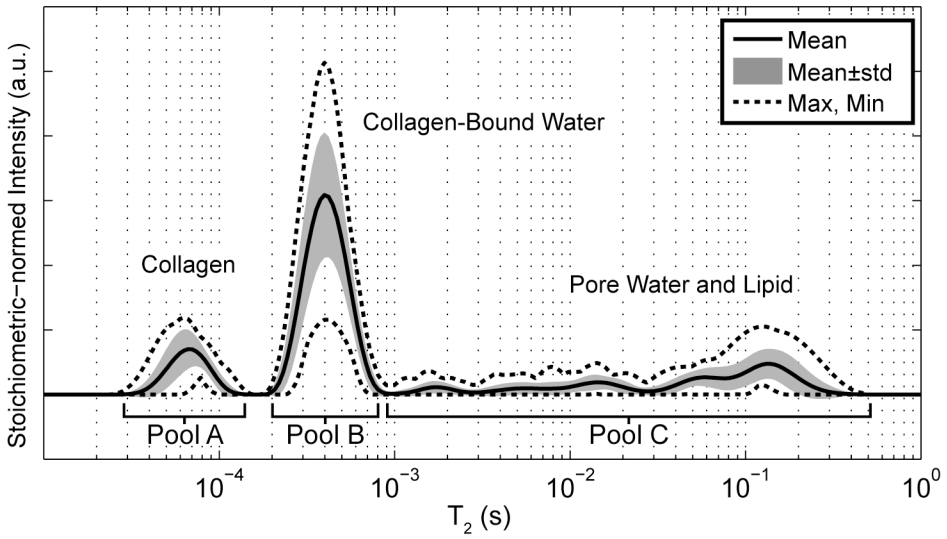

Figure 2.5 Averaged proton T_2 spectrum obtained from 40 human cortical bone samples [39].

Being a major component of bone mineral crystal (**Figure 1.4**) and directly proportional to the total amount of bone mineral content, the phosphorus nucleus (^{31}P) is also MR sensitive. In spite of having relaxation times even less favorable than bone water [41, 42], a number of studies have explored the feasibility of interrogating bone mineral via ^{31}P MRI [27, 31-33, 42-44].

2.2 Solid State MRI Techniques

Even though bone water and phosphorus are beyond the capability of conventional MRI techniques due to their extremely short transverse relaxation times, specially designed imaging sequences featuring extraordinarily short TE (solid-state imaging sequence) can be utilized. A couple of solid-state MRI techniques have been developed in response to challenges posed by species with extremely short effective transverse relaxation time.

2.2.1 Ultra-short Echo Time Imaging (UTE)

One such technique is ultra-short echo time (UTE) imaging [45]. In a typical UTE experiment (**Figure 2.6a**), the encoding gradient is switched on immediately after the transmit/receive dead time, and data acquisition is initiated on the ramp-up stage of the gradient. Each excitation and readout results in a half projection within the k-space. The orientation of the encoding gradient is altered from one TR to the next to cover the entire k-space (**Figure 2.7a**). As a result of ramp sampling, where the gradient is not at full strength, and k-space is traversed more slowly (but at an accelerating speed) as compared to when the gradient is fully ramped up, the center of k-space is more densely sampled as compared to the outer k-space.

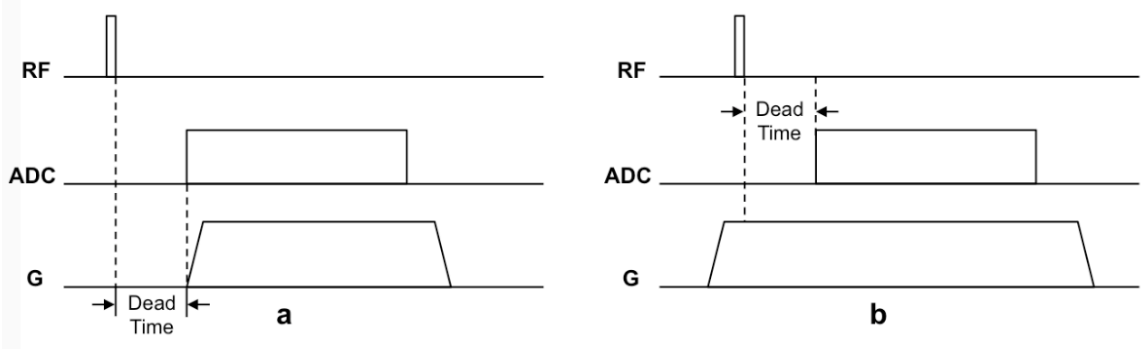

Figure 2.6 Sequence diagrams of a) UTE and b) ZTE.

A UTE sequence is characterized by the following features: first, with effective echo time limited only by the hardware's transmit/receive switch time (or receiver dead time), UTE is able to visualize spins with T_2* as short as a few hundred microseconds [45, 46]; second, the image is less prone to susceptibility artifacts due to the short TE.

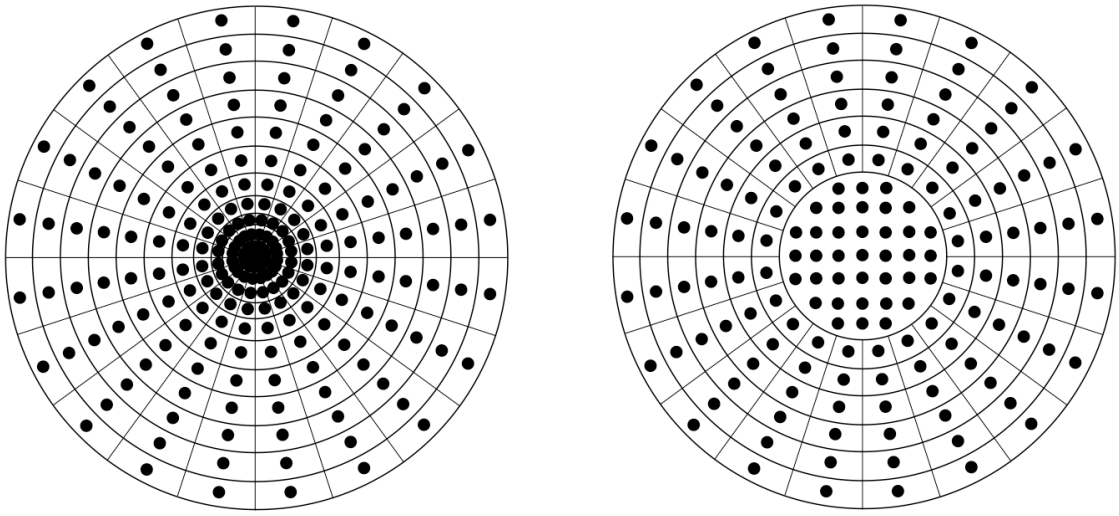

Figure 2.7 k-Space of a) UTE and b) ZTE-PETRA sequence. In UTE, k-space encoding starts during the ramp-up stage of the gradient. Therefore, sampling density is higher near the k-space center than in the outer region where the gradient reaches full strength. Encoding direction is altered from one TR to the next to cover the entire k-space. In ZTE, on the other hand, the gradient is fully ramped up prior to RF excitation, resulting in k-space data missing around the center due to the transmit/receive switch. In the case of ZTE-PETRA, the missing data points are recovered via single point imaging on a Cartesian grid through a second acquisition.

2.2.2 Zero Echo Time Imaging (ZTE)

Another powerful short-T_2 visualization technique is zero echo time (ZTE) imaging (**Figure 2.6b**). In contrast to UTE, the encoding gradient is fully ramped up prior to the RF pulse in ZTE, and data are collected immediately following the transmit/receive dead time. Since the gradient is always on, k-space encoding starts instantaneously after excitation (hence the name 'zero' echo time) and the data points encoded during dead time are lost. The missing data points are recovered via a second set of scans, where the inner k-space is filled either by FIDs acquired with lower bandwidth, as the SMRI [47]

used in WASPI [48], or with single point encoded with an incrementally-stepped gradient as in PETRA [49]. As shown in **Figure 2.7b**, a ZTE (PETRA in this case) k-space consists of two distinct regions. The peripheral portion corresponds to the initial radial acquisition, while the central portion corresponds to the second acquisition acquired on a Cartesian grid.

Although the effective echo time of ZTE is also determined by the hardware, as in UTE, the center portion of k-space is traversed faster because the encoding gradient is already at full strength. Further, the PETRA acquisition allows the data points near k-space center to be acquired at the same effective echo time. Therefore, ZTE images possess higher signal-to-noise ratio (SNR) and are less prone to blurring than UTE images.

One inherent drawback of ZTE is the presence of encoding gradient during excitation, which renders the RF pulse spatially selective. The varying excitation profile from k-space line to k-space line can result in undesirable shading artifacts and blurring throughout the reconstructed image. Since the frequency response of a RF pulse could be approximated by the Fourier transform of the pulse shape in the low flip-angle regime [50], the wider the pulse, the heavier the signal modulation. As well, restrictions on the specific absorption ratio (SAR) limit the peak B_1 power of the RF pulse. As a result, ZTE is restricted to low FA applications in humans.

2.2.3 UTE and ZTE Image Reconstruction

For MR data acquired in Cartesian k-space (as is the case for most clinical MRI sequences), images can be reconstructed via direct fast Fourier transform (FFT). For sequences acquiring data in non-Cartesian k-space such as UTE and ZTE, direct

application of FFT will not work. Instead, the radially collected data points must be first re-gridded onto a Cartesian coordinate. The re-gridded points are essentially the weighted sum of the neighboring original data. However, the varied distance of each raw data point to a specific point on the Cartesian grid determines they may not necessarily have the same contribution in this process. For instance, in **Figure 2.7,** the sampling pattern is generally denser in the inner k-space than in the outer. Therefore, a faithful image reconstruction relies on proper weight (or sampling density) compensation of the raw data [51]. Following the re-gridding procedure, the image is generated with FFT as in conventional MRI.

2.3 Separation of Different Bone Water Pools

2.3.1 Bone water separation techniques

In addition to capturing bone water signals, the ability to distinguish between water pools is equally important, as they are biomarkers for different characteristics of bone. A number of T_2*- and T_2-based techniques have been proposed for this purpose. Dual-echo subtraction is the simplest and most straightforward T_2*-based method, in which two echoes (one at a short, the other at a longer TE) are acquired following each excitation. While the first echo contains signals from both short- and long-T_2* components, only the long-lived signal persists in the second echo [45, 52]. Therefore, short-T_2* BW could be established by subtracting echo two from echo one. However, this is not an ideal method to suppress long-T_2* species since remnants of PW remain in the resulting image. A second T_2*-based technique is bi-exponential fitting, whereby images are acquired at multiple TEs and fitted to a bi-exponential decay model to extract the relative proportions of the two water pools [30, 53]. Unfortunately, this method is neither time efficient nor

robust across various field strengths [54]. Another problem associated with T_2*-based techniques is their difficulty differentiating BW from water in smaller pores, given their similar T_2*, which is not as much an issue for T_2-based methodologies. One T_2-based method is dual-band saturation preparation, where a long pulse with two spectral saturation bands (at water and fat resonances, respectively) is applied prior to readout. Although effective at isolating short-T_2 BW, its effectiveness may be compromised by spatial variations in either the B_0 or B_1 field. Another commonly used long-T_2 suppression technique is adiabatic inversion recovery (IR) [55]. An adiabatic (hyperbolic secant, for example) is first applied to selectively invert the long-T_2 spins while the short-T_2 spins are merely saturated due to their fast transverse relaxation during the pulse. This is followed by conventional short TE readouts at the nulling time of the long-T_2 spins, leaving only short-T_2 spins detected.

2.3.2 Adiabatic Inversion

Adiabatic inversion recovery is based on a phenomenon called adiabatic following. From the perspective of the rotating frame (the coordinate system rotating about the z axis at the Larmor frequency), the B_1 is the only magnetic field present when the RF pulse is applied on resonance. On the other hand, applying the pulse with a frequency offset ($\Delta\omega$) is equivalent to having a residual z component of magnetic field in addition to B_1. Instead of rotating about the B_1, the magnetization will rotate about an effective field (B_{eff}), which is the vector sum of the applied B_1 and the residual longitudinal field. According to **Figure 2.8**, the angle between B_{eff} and the z-axis of the rotating frame is determined by the amount of offset-frequency. In other words, the orientation of B_{eff} could be manipulated by adjusting the frequency of the RF pulse. As long as the adiabatic

condition described in **Equation 2.1** is satisfied, magnetization will follow the path of B_{eff} (hence the name 'adiabatic following'). To achieve adiabatic inversion, the frequency of the RF pulse is 'swept' from one side of the Larmor frequency to the other. As a result, magnetization is rotated from z-direction to –z direction by following the effective field.

$$\left|{}^{d\alpha}/_{dt}\right| \ll \left|\gamma B_{eff}\right| \qquad [2.1]$$

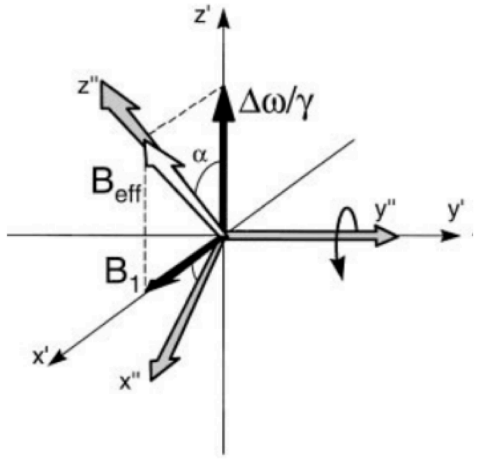

Figure 2.8 Vector diagram showing the effective field and its components. The thin black coordinate system (x', y' and z') is the rotating frame, while the thick gray coordinate system (x'', y'' and z'') is the frame for effective field [55].

The advantages of adiabatic IR include a narrow transition band (**Figure 2.9**) in frequency response and relative immunity to B_1 inhomogeneity and frequency offset. According to Li et al., the adiabatic inversion recovery-based technique achieves the best short-T_2 contrast [46].

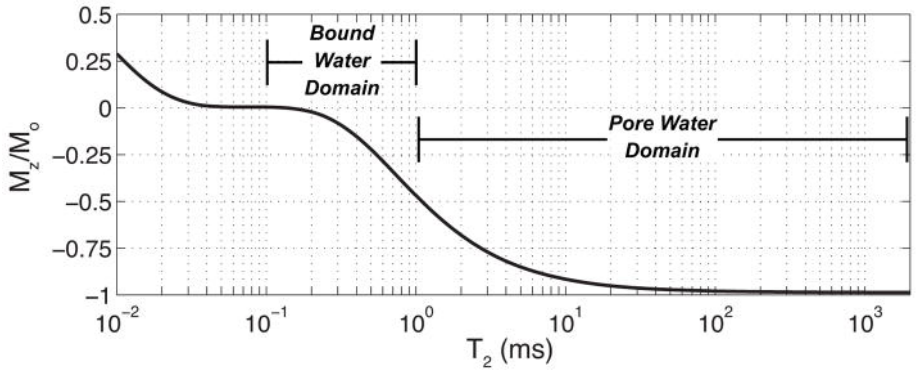

Figure 2.9 Response of magnetizations from different water pools to adiabatic inversion pulse as a function of T_2 [40].

2.4 Focus of This Dissertation: Cortical Bone

Over the past several decades, clinical investigations have focused on trabecular bone for two reasons [56-59]. First, most fracture sites are dominated by trabecular bone. Second, the faster remodeling rate of trabecular bone makes it a more convenient target than cortical bone to study the effectiveness of clinical intervention [60-64]. However, 80% of the skeletal system's mass consists of cortical bone. Although occurring at a lower rate, cortical bone also undergoes remodeling and major alteration due to aging or hormone depletion in women following menopause. The notion that stress is shared between cortical and trabecular bone at frequent fracture sites, such as the femoral neck, necessitates a better understanding of cortical bone as well. Therefore, the proposed project is fully dedicated to studying cortical bone.

2.5 Chapter Outline

This dissertation aims to explore the issues involved in establishing a protocol for MRI-based bone matrix and mineral examination in a clinical setting. In **Chapter 3**, the

feasibility of translating bone matrix and mineral quantification techniques previously developed and validated with animal and *ex vivo* experiments, to an *in vivo* application, is investigated. **Chapter 4** evaluates the *in vivo* values and inter-subject variation of bone ^{31}P relaxation times as well as their implication on bone mineral quantification. **Chapter 5** is dedicated to the impact of hardware imperfections on UTE image quality and image-based bone water quantification. **Chapter 6** presents an ongoing osteoporosis patient study that makes use of the techniques described in earlier chapters as well as some preliminary results. Major accomplishments of this dissertation and potential future works are summarized in **Chapter 7**.

CHAPTER 3: FEASIBILITY OF ASSESSING BONE MATRIX AND MINERAL PROPERTIES *IN VIVO* BY COMBINED SOLID-STATE ^{1}H AND ^{31}P MRI

3.1 Abstract

Purpose: To develop and evaluate an integrated imaging protocol for bone water and phosphorus quantification *in vivo* by solid-state ^{1}H and ^{31}P MRI.

Methods: All studies were health insurance portability and accountability act (HIPAA)-compliant and were performed with institutional review board approval and written informed consent. ^{1}H UTE and ^{31}P ZTE sequences were designed and implemented on a 3 T clinical MR scanner to quantify bone water and mineral *in vivo*. The left tibia of ten healthy subjects (including both genders, 49±15 y/o) was examined with a custom-built ^{1}H/^{31}P dual-frequency extremity RF coil. Total bone water (TW), water bound to the collagen matrix and bone phosphorus were quantified from MR images with respect to reference samples of known ^{1}H or ^{31}P concentration, and pore water was subsequently determined from total water and bound water. Porosity index (PI) was calculated as the ratio between UTE images acquired at two echo times. MRI parameters were compared with bone density measures obtained by high-resolution peripheral quantitative CT (HR-pQCT).

Results: The total scan time for the bone water and phosphorus quantification protocol was about 50 minutes. Average TW, BW, PW and ^{31}P concentrations were 13.99 ± 1.26, 10.39 ± 0.80, 3.34 ± 1.41 mol/L and 5.29 ± 1.15 mol/L for the studied cohort, respectively, in good agreement with previous results conducted *ex vivo*. Average intra-

subject coefficients of variation were 3.47%, 2.60% and 7.50% for TW, BW and PW and 5.60% for ^{31}P. Negative correlations were observed between PW and vBMD ($p < 0.05$) as well as between PI and ^{31}P ($p < 0.05$), while bone mineral content (BMC) estimated from ^{31}P MRI and HR-pQCT were strongly positively correlated ($p < 0.0001$).

Conclusion: This work demonstrates the feasibility of quantifying bone water and mineral phosphorus in human subjects in a single MRI session with a clinically practical imaging protocol.

3.2 Introduction

Cortical bone, which accounts for 80% of the skeleton by weight, consists of an organic substrate (also referred to as matrix) composed predominantly of type I collagen, interspersed with mineral crystals of non-stoichiometric calcium apatite. Blood supply occurs through a system of interconnected pores (Haversian and Volkmann canals). In osteoporosis, an increasingly prevalent condition afflicting the older population [12, 65], thinning of the cortical shell occurs, along with pore expansion and depletion of mineral and matrix, thereby compromising the bone's mechanical competence [66].

The current standard modality for osteoporotic fracture risk assessment is DXA, which measures gross density of bone material and, thus, cannot provide information on microstructure (such as cortical pore volume fraction and pore size distribution) or tissue mineralization. Consequently, DXA has low predictive accuracy — only 44% of non-vertebral fractures were found to occur in women with DXA-reported T-scores below -2.5 [23]. Similarly, DXA is unable to distinguish osteomalacia, a disorder in which bone is poorly mineralized but the pore volume fraction remains largely unchanged [67], from

osteoporosis, where pore volume fraction increases but the remaining bone is normally mineralized.

Risk assessment has recently been augmented with the fracture risk assessment tool (FRAX) [68]. However, alternative techniques that can directly evaluate bone matrix, pore space, and mineralization *in vivo* are needed to provide more complete insight into the determinants of the bone's mechanical competence.

Intra-cortical remodeling during aging, and more so in osteoporosis, involves expansion of pores [69]. Although most pores are beyond the resolution limit of *in vivo* imaging modalities, the portion of total bone water residing in the pore space scales inversely with matrix density [28] and has been shown to be quantifiable by MRI. On the other hand, although collagen protons themselves are not visible with clinical imaging equipment owing to their extremely short T_2 (tens of microseconds), water bound to collagen scales linearly with bone matrix density. It has been shown that these two water pools can be distinguished from one another given their very different T_2 [70] or T_2 relaxation times [53]. *Ex vivo* studies have demonstrated quantification of pore and bound water based on MR images of human cortical bone [27, 28], as well as the correlation between these water pools and bone mechanical strength [39, 71, 72]. Techawiboonwong et al. first quantified total bone water in the tibial cortex *in vivo* [73], while separation of the two water pools (BW and PW) *in vivo* has recently been reported by Manhard et al. using T_2-selective imaging sequences [29] and, more recently, by Chen et al. using bi-exponential fitting of the T_2 signal decay [30].

Quantitative MRI of ^{31}P would potentially provide complementary insight into bone

mineral properties. Animal studies have shown that ^{31}P MRI-based quantification is able to detect impaired mineralization density in hypophosphatemia-induced osteomalacia in a rabbit model, as well as effects of anti-resorptive treatment in ovariectomized rats at 9.4 T [31-33]. The feasibility of *in vivo* ^{31}P imaging in human subjects was shown first at 1.5 T [44] and, more recently at 3 T [42], albeit without quantification of ^{31}P. Seifert et al. measured phosphorus density by ^{31}P solid-state MRI of human cortical bone of the tibia *ex vivo* at 7 T using custom-designed RF coil and pulse sequences [27]. However, there have so far been no reports on quantification of ^{31}P density by *in vivo* human MRI.

The current work aims to demonstrate the feasibility of combined MRI-based *in vivo* bone water and mineral quantification, including discrimination of bound and pore water, as part of a single integrated imaging protocol.

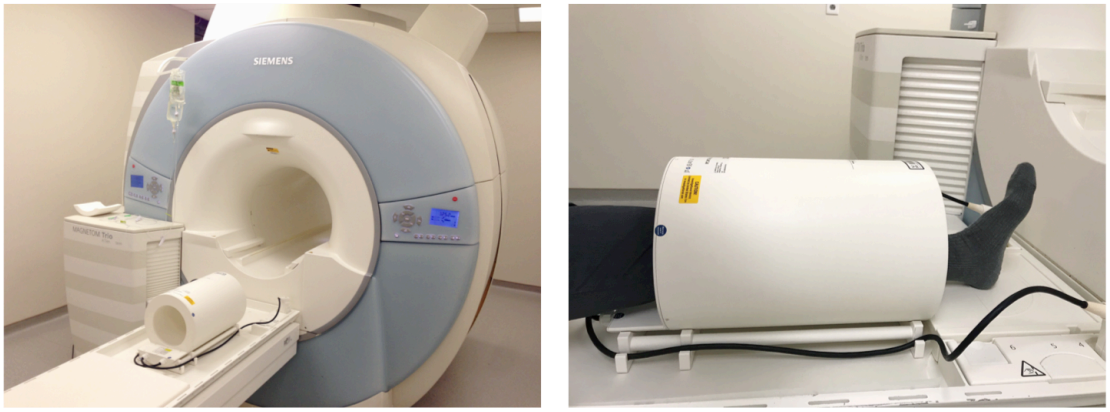

Figure 3.1 *In vivo* experiment set up. The experiment was performed on a Siemens 3 T Trio system with a Rapid ^{1}H/^{31}P dual-frequency birdcage calf coil.

3.3 Materials and Methods

3.3.1 Human Subjects

^{31}P ZTE's capability of detecting the ^{31}P signal in the tibial shaft was initially evaluated on a 32-year old male in the presence of hydroxyapatite samples with ^{31}P concentrations distributed in a wider range (3–7.5 mol/L). Subsequently, the entire protocol was executed in a cohort of healthy subjects. Inclusion criteria for enrollment were: 1) no medical history of diseases or treatments known to affect bone mineral homeostasis (e.g. mal-absorption syndromes, renal or hepatic disease, treatment with dexamethasone or methotrexate); 2) no conditions limiting normal physical activity (e.g. stroke, hip or leg fracture, rheumatoid arthritis); 3) body mass index < 30 kg/m^2. All *in vivo* studies were done in compliance with health insurance portability and accountability act (HIPAA) regulations, and were approved by the University of Pennsylvania's institutional review board (IRB) under protocol #823377. All subjects provided written informed consent. Ten healthy volunteers (two males, eight females, age range: 29 to 65 y/o, mean (SD) = 49 (15) y/o), recruited from the University of Pennsylvania (Philadelphia, PA), from July to August of 2016, participated in this study.

3.3.2 Imaging Protocol

MRI scans were performed on a 3 T TIM Trio system (Siemens Medical Solutions, Erlangen, Germany) using a custom-built transmit/receive ^{1}H (123 MHz)-^{31}P (49.9 MHz) dual-tuned birdcage coil (Rapid Biomedical, Rimpar, Germany). The hardware setup is shown in **Figure 3.1**. The complete protocol including localizer scans, ^{31}P transmit power

calibration and three radial imaging scans for quantification of bone water and phosphorus lasted approximately 50 minutes. The radial scans consisted of two ^{1}H UTE sequences for quantification of TW and BW (from which PW was indirectly determined) and one ^{31}P ZTE sequence for measuring bone phosphorus content. Details are given in the sub-sections below. All scans were carried out in the presence of a ^{1}H density calibration sample (20% H_2O/80% D_2O, doped with 27 mmol/L of $MnCl_2$, corresponding to a H_2O concentration of 11 mol/L, T_1 = 4.3 ms, T_2 = 320 μs) and two ^{31}P density calibration samples (one consisting of a mixture of hydroxyapatite and calcium sulfate powders, [^{31}P] = 7.5 mol/L, T_1 = 46.2 s, T_2 = 139 μs; and one consisting of pure hydroxyapatite powder, [^{31}P] = 9.5 mol/L, T_1 = 42.2 s, T_2 = 145 μs), positioned in close proximity and directly anterior to the section of tibia being examined. This MRI procedure was applied in ten subjects, and was repeated an additional two times in a subset of three subjects to evaluate test-retest repeatability. Each of these three subjects dismounted the table and was repositioned between successive repetitions on the same day, or was scanned on a different day within a three-week period. MRI scans were centered at 38% tibia (38% of the tibia length from the medial malleolus), where the cortical bone is thickest [27]. HR-pQCT was also performed for comparison with ^{31}P results.

^{1}H dual-echo UTE

Total water was imaged using a 3D ^{1}H dual-echo UTE sequence [46] (**Figure 3.2a**). An 80 μs rectangular RF pulse was used for excitation, and two 'echoes', were sampled at 50 μs (TE_1) and 4.6 ms (TE_2) after the RF pulse. The prescribed field of view (FOV) was $(250\ mm)^3$, TR was 10 ms, and FA was 16°. Fifty thousand radial spokes, distributed to

fully sample the spherical k-space, were collected at a dwell time of 4 µs in 8.3 min. The duration of the gradient ramp was 240 μs, and 158 points were acquired along each radial spoke to populate an image matrix of 256x256x256. Images were reconstructed at an isotropic voxel size of $(0.98\ \text{mm})^3$.

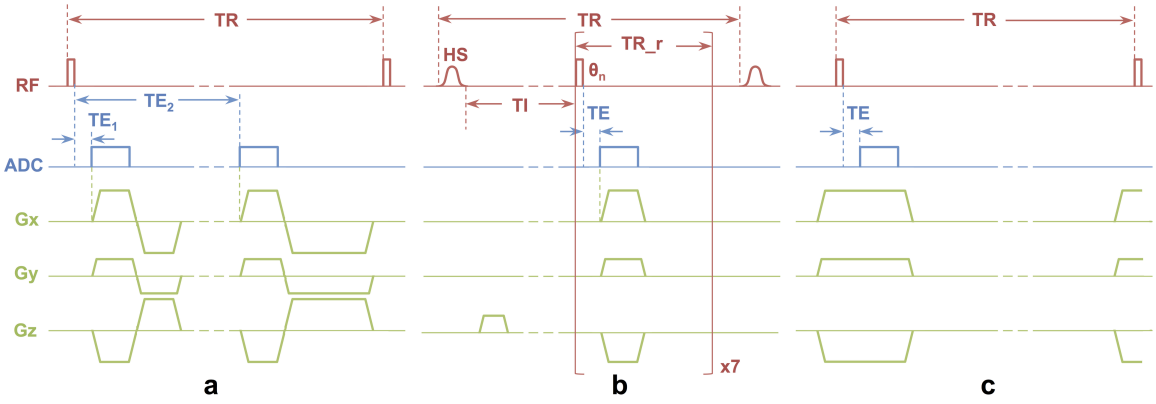

Figure 3.2 Diagrams of UTE and ZTE radial imaging sequences. a) ^{1}H dual-echo UTE and b) ^{1}H IR_rUTE sequences for bone water quantification and porosity evaluation. In (a), two FIDs were collected following each excitation, at TE_1 = 50 µs and TE_2 = 4.6 ms. Spins were rewound after collecting the first FID but spoiled after the second. In (b), an HS pulse was applied to specifically invert long-T_2 spins while saturating short-T_2 spins, followed by an inversion time TI to null long-T_2 spins, and seven UTE readouts. c) ^{31}P ZTE to quantify bone ^{31}P concentration. Readout gradients are switched on prior to the RF pulse to ensure k-space is traversed with full speed following excitation.

^{1}H IR-rUTE

Bound water was isolated and imaged using a 3D ^{1}H IR-prepared rapid UTE (IR-rUTE) sequence [46, 74] (**Figure 3.2b**), which takes advantage of the differences in both T_1 and T_2 of bound and pore water. Due to its T_2-selectivity, the adiabatic inversion pulse at the beginning of each TR inverts the long-T_2 pore water magnetization while only saturating the short-T_2 bound water spins [27]. After an appropriately chosen inversion recovery

delay (TI), at which time the longitudinal magnetization of pore water spins reaches zero while that of bound water has recovered to a positive value, a series of seven spokes were acquired [74]. Thus only bound water signal is detected within cortical bone. In the current implementation, adiabatic inversion was realized by a 5-ms, 5-kHz hyperbolic secant (HS) pulse, TI was set to 65 ms, and repetition time between consecutive inversions was 194 ms. Each of the seven UTE readouts was initiated by an 80 μs rectangular pulse, with flip angles increasing from 23° to 40° (variable flip angle scheme, VFA [74]) to create constant transverse magnetization from a diminishing reserve of longitudinal magnetization. The separation between each UTE readout was 2 ms. Twelve thousand spokes were collected at an effective TE of 50 μs resulting in 5.8 min total scan time. FOV, dwell time, number of points, and voxel size were the same as for dual-echo UTE.

^{31}P ZTE

Mineral phosphorus was imaged with the ZTE-PETRA technique [49] in lieu of the UTE strategy (**Figure 3.2c**). ZTE allows for faster k-space traversal, as no ramp sampling is involved. Therefore, given the extremely short T_2 (< 200 μs [42]), ZTE has been found to have superior SNR relative to UTE under similar sequence parameter settings [41]. Although the first several ZTE readout points are lost during the transmit/receive switching time, the PETRA technique recovers the lost data within this sphere via single point imaging (SPI, all at the same effective TE) — mitigating point spread function blurring of the image due to T_2 exponential modulation of the k-space. ^{31}P ZTE-PETRA was optimized for the experimentally observed relaxation parameters. TR and FA were 150 ms and 6.5°, rectangular RF pulse width was 16 μs, and 8000 spokes were sampled

at a dwell time of 8 μs. PETRA radius (equal to the number of readout samples lost during transmit/receive switching time) was set to 6 (hence, the effective TE was dwell time × PETRA radius = 48 μs), for a total of 895 single points [49]. FOV was matched to that of the two ^{1}H UTE sequences, but only 50 points along each spoke were acquired for reconstruction, leading to a reconstructed voxel size of $(2.5\ mm)^3$. Total scan time was 22.5 min. Since the scanner's transmit power auto-calibration was not operational for nuclei other than ^{1}H, the flip angle was calibrated for every subject prior to the ^{31}P ZTE scan by incrementally stepping the power and maximizing the equilibrium calf muscle phosphocreatine signal.

HR-pQCT

HR-pQCT scans were performed on an XtremeCT II system (Scanco Medical, Brüttisellen, Switzerland). X-ray tube was operating at voltage/current of 68 kVp/1.47 mA. A 140×140×10.2 mm^3 volume was imaged and reconstructed to a 2304×2304×168 matrix size, resulting in an isotropic spatial resolution of $(61\ \mu m)^3$. Only nine of the subjects received this scan because the scanner was unable to accommodate the limb size of one of the subjects.

3.3.3 Quantification

Images were reconstructed by re-gridding to Cartesian k-space and standard Fourier transform [49]. Cortical water concentrations were determined from ^{1}H images by referencing the signal within the tibial cortex to that of the $MnCl_2$ doped calibration sample, and ^{31}P concentrations were calculated similarly by referencing the tibial signal against that of the hydroxyapatite samples. Details on conversion of signal intensities to

concentration are given in the following sections. Both image reconstruction and quantification were performed with custom programs written in MATLAB (Mathworks, Natick, USA).

Bone water quantification

Total water was quantified from the central 45 slices (corresponding to a 44.1-mm thick slab) of the first echo image of the dual-echo UTE scan. Regions of interest (ROI) for cortical bone and calibration sample were drawn for each of these slices using a semi-automated segmentation algorithm [75]. The average intensity within the ROI of the calibration sample was used to compute the total water concentration within the cortical bone region on a pixel-by-pixel basis based on **Equation 3.1**:

$$\rho_{bone} = \rho_{ref} \frac{I_{bone} F_{ref}}{I_{ref} F_{bone}} e^{-TE\left(\frac{1}{T^*_{2\_ref}} - \frac{1}{T^*_{2\_bone}}\right)} \qquad [3.1]$$

where ρ_{ref} and ρ_{bone} are ^{1}H densities in reference sample and cortical bone respectively, I_{ref} and I_{bone} are image intensities, while F_{ref} and F_{bone} represent the fractions of magnetization available for signal detection (see **Appendix**).

We note that even though T_1 values of bone water and calibration samples differ, absolute concentrations can be computed from **Equation 3.1** since we know the chemical makeup, concentration and T_1 of the calibration sample. The same arguments also apply to quantification of ^{31}P mineral density below. Bound water maps were generated in the same way from the IR-rUTE images using the same ROIs based on **Equation 3.1**, but with F_{ref} and F_{bone} replaced by IR_F_{ref} and IR_F_{bone} respectively, which represent fractions of magnetization detected in IR-rUTE sequence (**Appendix**). Subtraction of the

Bound water from the total water maps yielded a parametric image of pore water. Median values were then used for statistical analysis. The following population average values for total and bound water relaxation times were used for bone water signal correction: T_{1_total} = 250 ms, T_{2_total} = 750 μs [75], T_{1_bound} = 145 ms, T_{2_bound} = 390 μs [54]. The ratio between the two images of dual-echo UTE sequence within the tibial cortex, referred to as porosity index [26], was also computed in a pixel-wise manner.

Bone phosphorus quantification

Due to the inherently lower SNR of ^{31}P images, ^{31}P concentration was quantified based on total signal within the volume of interest. To obtain the total ^{31}P signal 18 consecutive axial images (corresponding to the same volume over which bone water was evaluated) were first complex-summed along the slice direction to produce an axial projection image with adequate SNR to clearly delineate the tibia and calibration sample boundaries. An ROI fully encompassing the tibia was then selected. Then a second complex summation was performed for pixels within this ROI, resulting in a single value whose magnitude represents total ^{31}P signal. Signal from the reference samples was obtained in the same manner. Next, the actual volume of the tibial cortex was measured from the ROIs drawn for bone water quantification, whereas the volume of the HA sample was manually calculated using the inner diameter of the tubes. Volumetric average signal intensities of cortical bone and HA samples were subsequently determined, and after accounting for T_1 and T_2 differences, tibial ^{31}P concentration was estimated via **Equation 3.1**. Population averages of T_1 = 18 s and T_2 = 160 μs were taken for bone ^{31}P relaxation correction [42].

3.3.4 Statistical Analyses

Intra-subject coefficient of variation was calculated for all MRI-derived parameters for the three test-retest subjects. MRI-derived quantities were also compared with HR-pQCT reported volumetric bone mineral density (vBMD), and correlations among all parameters were determined. In addition, sub-region analysis was conducted by dividing the analysis slab into anterior, posterior, medial and lateral quadrants to determine possible regional differences in the measured parameters using analysis of variance (ANOVA), followed by post-hoc analysis. All statistical analyses were performed using JMP (SAS Institute Inc., Cary, USA).

3.4 Results

Figure 3.3a shows ^{31}P signal intensities of the mid-tibial cortex superimposed on a ^{1}H UTE image in one subject evaluated to determine feasibility of quantification along with HA reference samples. Average signal intensities of the four samples are plotted against their respective ^{31}P concentrations in **Figure 3.3b**, showing the expected linear relationship between actual concentration and signal intensities ($R^2 = 0.98$).

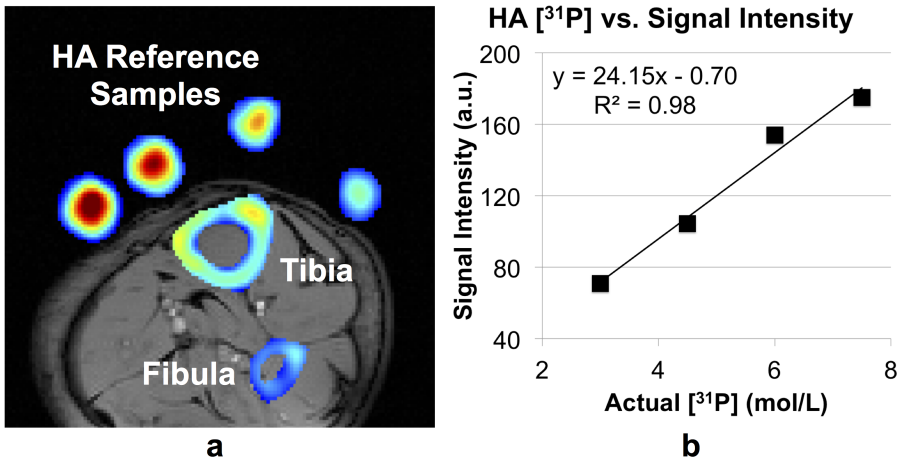

Figure 3.3 *In vivo* phosphorus intensity map and correlation with calibration samples. a) ^{31}P image acquired in a 32 y/o male corresponding to a projection from 6-cm thick slab showing tibia, fibula, as well as four HA reference samples, superimposed on a proton anatomic image. b) Average signal intensity vs. ^{31}P concentration for the four HA reference samples. Sample concentrations were 3, 4.5, 6 and 7.5 mol/L respectively.

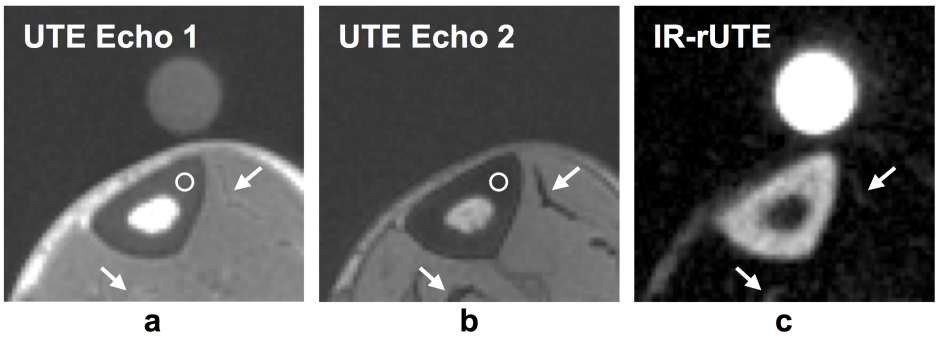

Figure 3.4 Total and bound water images of cortical bone. Bone water images from a 48 y/o male subject reconstructed from a) first and b) second echo of the dual-echo UTE sequence; c) Bound water image from the IR-rUTE sequence. Note that in (c) surrounding soft tissues as well as bone marrow within the medullary cavity is selectively suppressed via adiabatic inversion, leaving only short-T_2 ^{1}H density calibration sample and water tightly bound to collagen matrix. Image intensity measured from the circular ROI is noticeably higher in the first echo (0.32 versus 0.03 in the second echo). Also note similar intensity properties of the fasciae (arrows).

Representative dual-echo UTE and IR-rUTE images are displayed in **Figure 3.4a–c**. In

the two UTE images acquired at TE = 50 and 4600 μs the cortex appears dark with soft tissues slightly reduced in intensity at the longer echo time (**Figure 3.4a** and **3.4b**). However, the ROI (white circle) signal amplitude in the cortex is significantly greater for the first echo (0.32 versus 0.03). Also noticeable in **Figure 3.4b** are the fasciae (arrows), collagenous structures containing very short-T_2 hydration water, appearing with background intensity as does the cortex. Further, the ^{1}H reference sample present in the first echo image is no longer visible in the second echo image given the doped water's very short T_2 (~ 320 μs). In the inversion-recovery long-T_2 suppressed image of the same slice (**Figure 3.4c**), muscle, subcutaneous and marrow fat are almost invisible while the cortex and fasciae now appear bright as does the reference sample. Average SNR, here defined as the ratio of the mean signal amplitude within cortical bone to that of the background in magnitude images, measured across all subjects were 12 and 6 for the first and second-echo UTE images, respectively, and 17 in the IR-rUTE images. **Figure 3.5** demonstrates the ROIs generated using the semi-automatic segmentation algorithm.

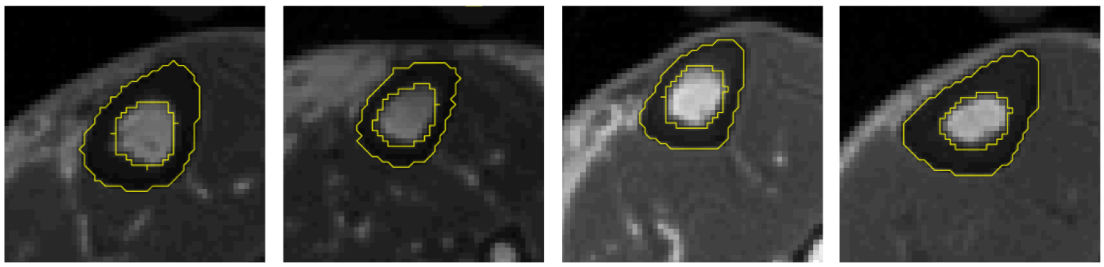

Figure 3.5 Cortical bone ROI generated using the semi-automatic algorithm from the first echo image of dual-echo sequence is shown for four subjects.

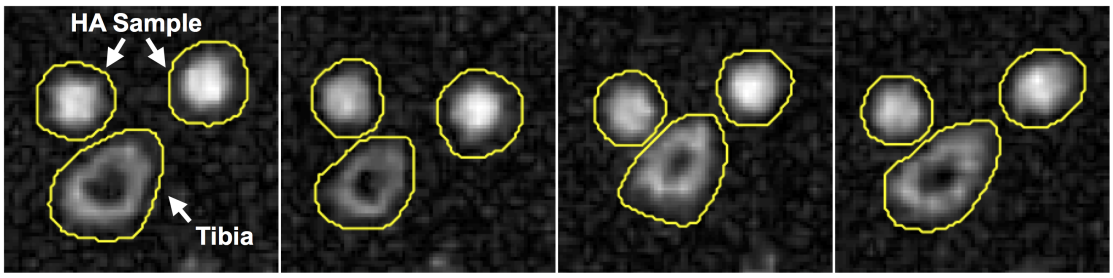

Figure 3.6 *In vivo* phosphorus images. ^{31}P projection images (complex summation of a 45-mm thick slab) of four subjects with ROIs overlaid.

Figure 3.6 displays ^{31}P projection images of four subjects (average SNR ~ 10 for tibia). The two HA reference samples and the tibia are unambiguously identified on this projection from a 45-mm thick volume, and the medullary cavity of the tibia is well delineated. **Figure 3.7** shows bone water and ^{31}P density color maps for five of the study subjects. Bone mineral content (BMC) based on MRI-quantified total ^{31}P content (assuming a bone apatite stoichiometry represented by $Ca_5(OH)(PO_4)_3$ is plotted against that measured by HR-pQCT in **Figure 3.8**, showing the two quantities to be strongly correlated.

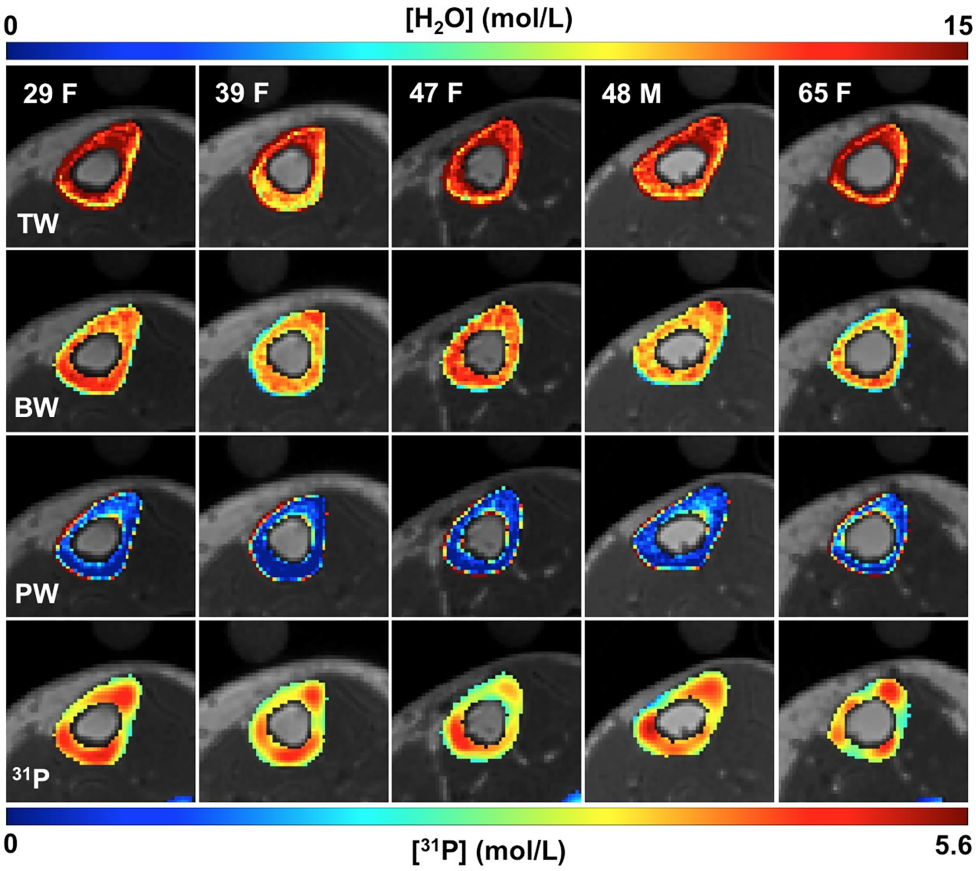

Figure 3.7 Bone water and phosphorus color maps for five of the ten study subjects. Differences in the distribution of both bone water and ^{31}P are visually apparent across subjects. ^{31}P maps were interpolated to match the resolution of the proton images.

MRI-derived parameters and HR-pQCT reported vBMD are summarized in **Table 3.1** for all ten subjects. For the three subjects participating in test-retest validation, average values from three measurements are reported in the table. Average TW, BW and PW concentrations within this subject cohort were 13.99 ± 1.26, 10.39 ± 0.80 and 3.34 ± 1.41 mol/L, respectively. The average PI was 0.34 ± 0.06, and bone ^{31}P concentration was 5.29 ± 1.15 mol/L.

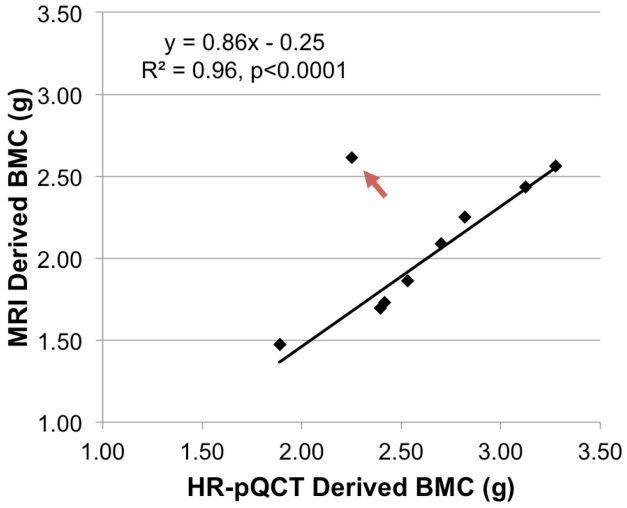

Figure 3.8 Comparison of BMCs estimated using MRI and HR-pQCT. BMC based on MRI-derived total ^{31}P content plotted against HR-pQCT derived BMC for a 1-cm thick slab of tissue for nine subjects (only nine of the subjects could be scanned because the scanner was unable to accommodate the limb size of one subject). For HR-pQCT, BMC was computed by multiplying the reported vBMD with the volume of a 1-cm slab. The fitted line was obtained after excluding the 62 y/o female subject with abnormally high MRI-derived ^{31}P concentration (red arrow).

Sub-region analysis revealed significant inter-site differences for some but not all of the parameters extracted, including pore water and total water fraction (ANOVA, $p < 0.001$). The significantly greater values for PW laterally suggest greater porosity at this location (**Figure 3.9**).

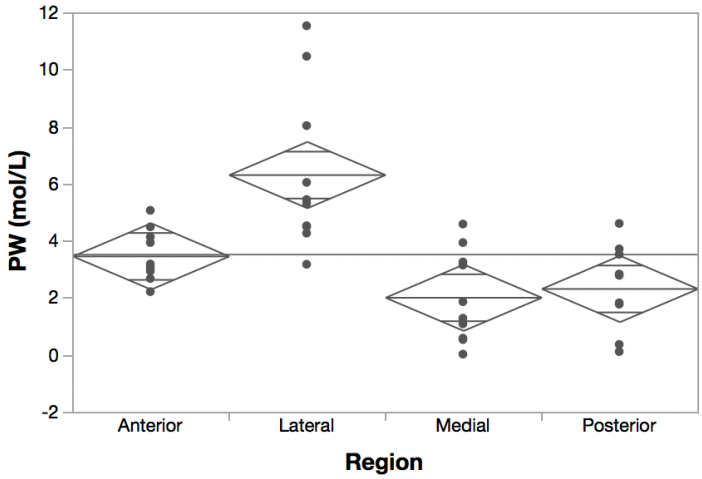

Figure 3.9 Regional dependence of pore water. In order to investigate potential spatial dependence of MRI-derived parameters, the tibial cortex of each subject was divided into four quadrants: anterior, posterior, medial and lateral. ANOVA was applied to compare each parameter among these spatial locations, and pore water was found to be significantly higher in the lateral region than in the other three quadrants.

A positive correlation was found between TW and PW ($R = 0.81$, $p < 0.005$) while PW was negatively correlated with vBMD ($R = -0.71$, $p < 0.05$), both expected. Both are plausible associations as a change in total water fraction is driven by the change in fractional pore space, and the latter is inversely related to osteoid volume fraction and thus, at constant mineralization, to BMD.

Table 3.1 Bone water, porosity and phosphorus quantification results for all ten subjects

Subject (Age/Gender)	Bone Water (mol/L)			PI	^{31}P (mol/L)	vBMD (mg/cm)
	TW	BW	PW			
29 F	13.87	11.02	2.50	0.32	5.18	1016.8
31 F	13.19	10.75	2.15	0.37	4.75	1005.8
32 M	15.23	9.59	5.58	0.44	4.35	N.A.
39 F	11.71	10.15	1.39	0.33	4.86	1013.5
47 F	13.96	11.42	2.28	0.35	4.79	1023.0
48 M	13.77	10.96	2.55	0.26	5.27	1006.6
62 F	12.62	8.87	3.45	0.24	8.41	1023.0
63 F	15.54	9.94	5.40	0.36	5.61	986.9
65 F	14.44	10.06	4.07	0.37	4.72	994.1
65 F	15.54	11.16	4.06	0.31	4.96	1000.2
Mean	**13.99**	**10.39**	**3.34**	**0.34**	**5.29**	**1007.8**
SD	**1.26**	**0.80**	**1.41**	**0.06**	**1.15**	**12.6**

Test-retest results are given in **Table 3.2**. The CVs for two directly measured water quantities, TW and BW, are below 5% for all three subjects, but somewhat greater for PW (up to 8.5%), since instead of being a directly quantified parameter, the latter was obtained as the difference between two relatively large quantities, making it susceptible to errors in measurement. The average CV was 3.8% for the PI and 5.7% for bone ^{31}P concentration.

Table 3.2 Test-retest repeatability in three subjects

Subject (Age/Gender)	29 F					32 M					48 M				
	TW	**BW**	**PW**	**PI**	**^{31}P**	**TW**	**BW**	**PW**	**PI**	**^{31}P**	**TW**	**BW**	**PW**	**PI**	**^{31}P**
Scan 1	14.16	11.24	2.59	0.33	4.91	15.35	9.61	5.71	0.43	4.37	13.05	10.42	2.34	0.26	5.32
Scan 2	14.08	11.10	2.63	0.34	5.55	15.56	9.69	5.87	0.43	4.56	14.19	11.20	2.77	0.26	5.53
Scan 3	13.36	10.73	2.29	0.30	5.08	14.77	9.48	5.16	0.45	4.11	14.07	11.27	2.55	0.27	4.97
Mean	**13.87**	**11.02**	**2.50**	**0.32**	**5.18**	**15.23**	**9.59**	**5.58**	**0.44**	**4.35**	**13.77**	**10.96**	**2.55**	**0.26**	**5.27**
SD	**0.44**	**0.26**	**0.19**	**0.02**	**0.33**	**0.41**	**0.11**	**0.37**	**0.01**	**0.23**	**0.63**	**0.47**	**0.22**	**0.01**	**0.28**
CV (%)	**3.18**	**2.39**	**7.42**	**6.44**	**6.40**	**2.69**	**1.10**	**6.67**	**2.64**	**5.20**	**4.55**	**4.30**	**8.42**	**2.19**	**5.36**

3.5 Discussion

By providing quantitative information on both bone water and ^{31}P — surrogate markers of the organic and mineral phases of bone, respectively — the proposed dual-nucleus protocol has the potential to differentiate osteoporosis from demineralizing disorders such as osteomalacia, which is not achievable with currently available non-invasive modalities. As the respective surrogate marker of bone mineral content and matrix, the ratio of ^{31}P and BW densities is expected to provide an indirect measure of the degree of mineralization. Because the two disorders differ in their underlying mechanisms, accurate diagnosis is crucial for effective medical intervention. Absence of ionizing radiation in MRI also makes it suitable for longitudinal studies involving one or more follow-up exams to monitor patient response to treatment (e.g. monitoring the response to anti-resorptive treatment for osteoporosis, or vitamin-D supplementation in osteomalacia).

Compared to bone water, ^{31}P in bone is considerably more challenging to image due to the nucleus' substantially shorter T_2 and much longer T_1 (160 μs and 18 s for ^{31}P, respectively at 3 T [42]). The rapidly decaying signal results in broadened point spread function (full width at half maximum ~ 4 mm at the gradient strength of 30mT/m used), potentially posing a hard limit on the maximally achievable spatial resolution. This limitation, however, is somewhat mitigated by the ZTE-PETRA sequence due to its more rapid traversal of k-space (no ramp-sampling), and constant TE within the central k-space (PETRA) region. The very short signal lifetime and long T_1 of ^{31}P also entail reduced SNR compared to that of ^{1}H imaging. ^{31}P also exists in lower concentration than ^{1}H (~ 7 versus ~ 28 mol/L of ^{1}H in bone water), and has a lower gyromagnetic ratio (by a factor of 2.5 relative to protons). The convergence of these factors renders *in vivo* phosphorus

imaging with adequate resolution and SNR extremely challenging. In fact, in order to achieve ^{31}P SNR per unit time comparable to that of bone water, Wehrli et al. projected that the spatial resolution would have to be relaxed by a factor of 20 [76].

In perhaps the first feasibility study of *in vivo* solid-state bone ^{31}P MRI by Robson et al. in the human tibia at 1.5 T [44], a 2D UTE sequence with a half-sinc pulse was used, requiring 64 averages to achieve sufficient SNR. The approximately 14-minute scan time, while clinically practical, yielded only a single slice of 60 mm thickness. Although quantification was performed in a whole-volume fashion in the current study as well, the ultimate goal is to be able to evaluate regional variations of ^{31}P density. More recently, in very elegant work, Wu et al. demonstrated the feasibility of *in vivo* 3D ^{31}P imaging of the human wrist at 3 T in 37 minutes [42], although no density quantification was performed. In their implementation, a ZTE-type sequence was used in combination with a custom wrist coil, which provides relatively high detection sensitivity due to its close proximity to the imaging volume. In the only MRI-based human bone ^{31}P quantification study to date, Seifert et al. reported an average ^{31}P concentration of 6.74 mol/L in tibia specimens [27], versus 5.29 ± 1.15 mol/L observed in the current *in vivo* work.

In the present study we utilized a birdcage coil with an inner diameter of 17 cm. Although some sensitivity is lost due to its large dimensions, it allows sufficient space for placement of calibration samples while providing a relatively large homogeneous B_1 region. Measurements in ^{1}H images of the homogeneous Siemens doped water phantom (3.75 g $NiSO_4$ $6H_2O$ + 5 g NaCl per 1000 g of H_2O) confirmed that signal variation was less than 10% within the volume of interest used in this study. Although the ^{31}P transmit B_1 was not measured directly, it was assumed to have similar homogeneity as that

generated by the concentric ^{31}P coil.

MRI-based bone water quantification at the mid-tibia has been reported in several prior studies. Techawiboonwong et al. reported an average TW concentration of 17.4% and 28.7% by volume (corresponding to 9.7 and 15.9 mol/L) in pre- and post-menopausal women, respectively [73]. More recently, Manhard et al. reported an average BW concentration of 13.9 mol/L and PW concentration of 3.7 mol/L in an *in vivo* study of a small group of subjects [29]. TW, BW and PW concentrations of 13.99 ± 1.26, 10.39 ± 0.80 and 3.34 ± 1.41 mol/L found in the current study are consistent with these earlier findings. Moreover, our test-retest experiments demonstrated repeatability for TW, BW and ^{31}P measurements *in vivo* on the order of 5–8%, therefore rendering the method well-suited for longitudinal studies.

Exclusion of an extreme outlier (see **Figure 3.8**) suggests negative correlations between vBMD and age ($R = -0.71$), and between BW and PI ($R = -0.65$) as well as a positive correlation between BW and vBMD ($R = 0.67$) although these associations did not quite reach statistical significance ($p < 0.08$), likely due to limited power of this feasibility study.

There was no significant correlation between MRI-derived ^{31}P concentration and HR-pQCT derived vBMD in contrast to a previous *ex vivo* study in human cortical samples using similar methodology [27] reporting a positive correlation between the MRI-derived ^{31}P concentration and CT-derived BMD ($R = 0.68$, $P < 0.005$). The same study also reported a positive correlation between BW and ^{31}P concentration ($R = 0.77$, $P < 0.005$). However, the current study did yield a strong positive correlation between BMC

measured with MRI and that measured with HR-pQCT ($R = 0.98$, $p < 0.0001$), as shown in **Figure 3.8**. Although this correlation was obtained with the same outlier exclusion stated above, statistical significance was still present even without exclusion of this particular subject ($R = 0.67$, $p < 0.05$).

The rationale behind choosing the tibia as the imaging location is based on the following considerations. First, its proximity to the body surface and the overall geometry of the lower leg makes the tibia technically more amenable to examine with an optimized RF coil than more deep-lying structures such as femoral neck. Second, the mid-tibial cortex is relatively thick (5–7 mm). Third, since at stance, for instance, a large proportion of stress that governs remodeling in bipeds is along the vertical axis of the body, it is plausible that bone loss at the tibia is similar to that at typical fracture sites such as the proximal femur and spine, but this conjecture obviously would require detailed scrutiny in future studies. Fourth, degenerative bone disease, notably osteoporosis, is a systemic disorder. It has long been known that age-related cortical bone pore volume expansion occurs at multiple anatomic locations, with detailed studies having been conducted at the humerus [77], the femoral shaft [78], radius [79], or ilium [80]. We also note that in prior work by some of the authors, MRI measures of the calcaneus, for instance, distinguished osteoporotic fracture patients from controls as well as or better than did BMD of the proximal femur or vertebrae [81]. Sub-region analysis showed site-specific differences for some of the parameters. While the clinical significance of such observations is currently not known and beyond the scope of this article, it is likely that remodeling-related effects in response to drug intervention are anatomic site-dependent.

In this work, UTE was used for imaging bone water and ZTE for bone phosphorus.

Seifert et al. showed experimentally that ZTE-PETRA provides SNR superior to its UTE counterpart for ^{31}P imaging [41]. Theoretically, bone water imaging should also benefit from ZTE for similar reasons. However, the peak B_1 of the coil limited the maximally achievable flip angle of a 16 μs rectangular pulse for ^{1}H to about 9°. In order to increase the flip angle (and SNR), pulse duration would have to be increased. This is not possible in ZTE: a pulse duration greater than twice the dwell time would cause severe excitation selectivity within the imaging field-of-view [50]. Therefore, UTE was utilized in lieu of ZTE for ^{1}H imaging so the flip angle could be optimized by increasing the RF pulse duration.

The present work has limitations. As a feasibility study it falls short of providing adequate power to test some of the associations examined. Second, the study used a 'population average' value of cortical bone T_1 values in computing the MR parameters. However, Seifert et al. demonstrated that the longitudinal relaxation time of bone ^{31}P scales with the degree of mineralization [41], thus the assumed T_1 may potentially deviate from actual values thereby adversely impacting quantification. This is less of a problem as long as the bone is normally mineralized (unlike in bone demineralizing disorders such as osteomalacia). The errors incurred from using an average ^{31}P T_1 value need be examined, as well as the feasibility of T_1 measurement within a maximum allowable procedure time of one hour. While deriving BW concentration from IR-rUTE images, BW magnetization was assumed to recover from zero after each inversion since the residual longitudinal magnetization immediately following the HS pulse has been found to be negligible [82]. Nevertheless, it is conceivable that saturation is not always complete. Further, a single inversion delay was used to null all long-T_2 species, as it has

been shown that the optimal delay is similar for tissue water and fat as long as TR < T_1 [46]. However, **Figure 3.4c** lends strong support of effective suppression of both bone marrow and surrounding soft tissues. Another potential source of systematic error is imperfect nulling of PW spins at the time of the excitation pulse given the wide range of their T_1 values [39].

3.6 Conclusion

In conclusion, the present feasibility study, while limited in scope, highlights the potential of solid-state MRI for the quantitative evaluation of cortical bone matrix and mineral properties in the form of an integrated, single-session quantitative study of bone water and mineral phosphorus.

3.7 Appendix

^{1}H UTE (^{31}P ZTE)

The transverse magnetization immediately after RF pulse in UTE and ZTE is given as:

$$F = M_{xy} = f_{xy} \cdot \frac{1 - e^{\frac{-TR}{T_1}}}{1 - f_z \cdot e^{\frac{-TR}{T_1}}}, \qquad [A\ 3.1]$$

where f_{xy} and f_z are mapping functions reflecting the response of longitudinal and transverse magnetization to a rectangle pulse the duration of which (τ) is comparable to the spin's effective transverse relaxation time (T_2*), and are defined as:

$$f_{xy} = \gamma B_1 \tau e^{\frac{-\tau}{2T_2^*}} \mathrm{sinc}\left(\sqrt{(\gamma B_1 \tau)^2 - \left(\frac{\tau}{2T_2^*}\right)^2}\right), \qquad [A\ 3.2]$$

and

$$f_z = e^{\frac{-\tau}{2T_2^*}}[\cos\sqrt{(\gamma B_1\tau)^2 - \left(\frac{\tau}{2T_2^*}\right)^2} + \frac{\tau}{2T_2^*}\,\mathrm{sinc}(\sqrt{(\gamma B_1\tau)^2 - \left(\frac{\tau}{2T_2^*}\right)^2})] \quad [A\ 3.3]$$

In the regime of τ << than T_2*, these two mapping functions reduce to $\sin(\gamma B_1\tau)$ and $\cos(\gamma B_1\tau)$ respectively.

^{1}H IR-rUTE

The signal of inversion recovery-prepared UTE is however, of a different steady-state. In order to derive an analytical solution, the magnetizations of bound water and reference sample were assumed to be fully saturated immediately after each adiabatic inversion (actually, numeric Bloch equation simulation indicated a residue of only ~5%), therefore, longitudinal magnetization of bound water (reference sample) right before the first UTE readout is:

$$M_z^-(1) = 1 - e^{-\frac{TI}{T_1}}, \quad [A\ 3.4]$$

with TI being the inversion recovery delay. And the longitudinal and transverse magnetization right after the RF pulse could be written as:

$$M_{xy}(1) = f_{xy} \cdot M_z^-(1), \quad [A\ 3.5]$$

$$M_z^+(1) = f_z \cdot M_z^-(1), \quad [A\ 3.6]$$

where f_{xy} and f_z are the same mapping function as described above. By the time of next RF excitation, transverse magnetization would completely vanish while longitudinal magnetization would have recovered for a period of (TR_r - τ) (**Fig 3.2b**), so the initial M_z

for all the rest six UTE readouts would be:

$$M_z^-(i) = 1 - [1 - M_z^+(i-1)]e^{-\frac{(TR_r - \tau)}{T_1}}, \qquad [A\ 3.7]$$

and the average value of transverse magnetization following all seven excitation is used to represent steady-state signal for bound water and reference sample:

$$IR_F = \frac{\sum_{i=1}^{7} M_{xy}(i)}{7}, \qquad [A\ 3.8]$$

CHAPTER 4: *IN VIVO* ^{31}P RELAXATION TIMES AND THEIR IMPLICATIONS ON MINERAL QUANTIFICATION

4.1 Abstract

Purpose: The inter-subject variations in bone phosphorus T_1 and T_2*, as well as the implications on *in vivo* ^{31}P MRI-based bone mineral quantification, were investigated at 3 T field strength.

Methods: A technique that isolates the bone signal from the composite *in vivo* ^{31}P spectrum was first evaluated via simulation and experiments *ex vivo* and subsequently applied to measure the T_1 of bone ^{31}P collectively with a spectroscopic saturation recovery sequence in a group of healthy subjects aged 26 to 76 years. T_2* was derived from the bone signal line width. The density of bone ^{31}P was derived for all subjects from ^{31}P zero TE images acquired in the same scan session using the measured relaxation times. Test–retest experiments were also performed to evaluate repeatability of this *in vivo* MRI-based bone mineral quantification protocol.

Results: The T_1 obtained *in vivo* using the proposed spectral separation method combined with saturation recovery sequence is 38.4 ± 1.5 s for the subjects studied. Average ^{31}P density found was 6.40 ± 0.58 mol/L (corresponding to 1072 ± 98 mg/cm^3 mineral density), in good agreement with an earlier study in specimens from donors of similar age range. Neither the relaxation times ($P = 0.18$ for T_1, $P = 0.99$ for T_2*) nor ^{31}P density ($P = 0.55$) was found to correlate with subject age. Average coefficients of variation for the repeat study were 1.5%, 2.6%, and 4.4% for bone ^{31}P T_1, T_2*, and

density, respectively.

Conclusion: Neither ^{31}P T_1 nor T_2* varies significantly in healthy adults across a 50-year age range, therefore obviating the need for subject-specific measurements.

4.2 Introduction

Recent advances in solid-state MRI have made possible imaging of the mineral portion of bone by means of ^{31}P UTE and ZTE pulse sequences [49, 83], including methods for quantification of ^{31}P density [27, 84]. The resulting measurements typically yield apparent density only, similar to 3D CT. However, MRI has the potential to quantify true mineralization density, often referred to as degree of mineralization of bone [85], which so far could be obtained only on specimens by means of autoradiography [86] or synchrotron radiation micro-tomography [87]. An assessment of degree of mineralization of bone requires knowledge of the unmineralized fraction of the bone, essentially the density of the collagen matrix [88]. The protons of collagen have T_2 on the order of 50 ms and are therefore not amenable to detection by *in vivo* MRI methods. However, as pointed out in a recent paper by Seifert et al., the collagen-associated water can be detected and quantified, thereby possibly serving as a surrogate for collagen itself [27].

Knowledge of degree of mineralization of bone is of interest because this quantity would allow differentiation of osteoporosis from osteomalacia. The former is characterized by loss of bone volume, with the remaining bone tissue properly mineralized, whereas in the latter case the osteoid is poorly mineralized even if the total volume may be normal. Of note is that current x-ray based densitometric techniques are unable to make this clinically important distinction. Both conditions are common in older people, but the

treatment of the two disorders is very different.

The practicality of accurate quantification of collagen-bound water has been demonstrated by several laboratories [30, 84, 88]. Quantification of mineral phosphorus by MRI in live human subjects, however, is far more difficult, although its feasibility has been reported recently [84]. Detection sensitivity scales as the ratio of T_2/T_1 ($\sim 10^{-5}$ for ^{31}P in apatite-like solids such as bone mineral), which is compounded by the ^{31}P nucleus' smaller gyromagnetic ratio ($\gamma_{31P}/\gamma_{1H} = 0.401$), lowering achievable SNR by another order of magnitude [76]. Further, quantification requires co-imaging a density calibration sample containing, for example, synthetic calcium hydroxyl apatite. Because the T_1 of the reference sample differs from that of bone, a signal intensity correction is needed to account for the differences. Thus, accurate knowledge of the ^{31}P relaxation properties of the bone is required to derive its density.

^{31}P T_1 relaxation in bone mineral is dominated by dipole–dipole relaxation with nearby protons, most likely crystal water or the hydroxyl ion. The relaxation rate ($1/T_1$) is proportional to the product of the squares of the gyromagnetic ratios of the interacting spins (^1H and ^{31}P) and inversely proportional to the sixth power of the inter-nuclear distance. It is the relative remoteness of nearby protons and their scarcity that renders this mechanism relatively ineffective. Nevertheless, as shown previously at 3 T, 80% of the relaxation rate is governed by ^1H-^{31}P dipole–dipole interaction, as determined by deuterium exchange of the labile protons [41]. On the other hand, the transverse relaxation rate ($1/T_2$) responsible for the very large line width of mineral ^{31}P has been attributed to homonuclear ^{31}P-^{31}P dipole–dipole coupling [89].

A number of previous studies have reported bone ^{31}P T_1 relaxation times [27, 41, 42, 44]. Seifert et al. measured bulk ^{31}P T_1 in lamb cortical bone [41] and subsequently in human bone specimens [27] using a saturation recovery (SR) method. Earlier, Robson et al. had reported image-based ^{31}P T_1 measurements in the human tibia *in vivo* with both SR and variable flip angle UTE at 1.5 T, finding average values of 8.6 s in seven subjects [44]. More recently, Wu et al. measured ^{31}P T_1 at 3 T in two subjects by means of a progressive saturation method, one spectroscopically (i.e., non-spatially resolved) and the other using a low-resolution image-based method, reporting values of 17 and 19 s, respectively [42]. The much longer values found at 3 T suggest a strong field dependence, which was studied systematically more recently by Seifert et al. [41], who found T_1 to increase mono-tonically with field strength in lamb cortical bone from 12.8 ± 0.5 s at 1.5 T to 97.3 ± 6.4 s at 11.7 T.

Most prior measurements, however, were either conducted *ex vivo* in various species, or *in vivo* using methods that required very long scan times. In addition, measurements *in vivo* may be affected by contributions from soft tissue ^{31}P signals arising from phosphorus metabolites. Robson et al. [44] discounted such effects as significant given that bone ^{31}P concentrations are larger by about three orders of magnitude than those of muscle metabolites. In the work by Wu et al., the experiments were conducted in the wrist [42], which is covered by only a thin layer of soft tissue. In the tibia, however, the volume fraction of muscle adjacent to bone is much larger. Thus, contribution of ^{31}P signal from metabolites could become more significant.

The primary objectives of the present work were to investigate means to isolate and measure bone ^{31}P T_1 values and to determine the implications of inter-subject variations

in T_1 on quantification of bone ^{31}P content. To this end, a technique to separate bone ^{31}P signal from those of the metabolites was first evaluated via simulation and *ex vivo* experiments and subsequently applied *in vivo* to measure bone ^{31}P T_1 relaxation times in a group of healthy subjects of wide age range. The measured relaxation properties were then used to estimate bone ^{31}P density from ZTE images. Finally, repeatability of the MRI-based bone mineral quantification protocol incorporating relaxation measurements was evaluated *in vivo*.

4.3 Materials and Methods

4.3.1 T_1 Measurement Sequence

T_1 of most tissues can be measured accurately by means of the inversion recovery strategy. However, due to its extremely short T_2, it is impossible to adequately invert the magnetization of bone ^{31}P. Therefore, an SR technique was used to measure ^{31}P T_1 [41]. Furthermore, the inherently low SNR of bone ^{31}P would make reliable image-based T_1 measurements prohibitively long. For this reason, a spatially non-selective spectroscopy-based method was implemented.

The SR spectroscopic sequence used starts off with a saturation (SAT) block to saturate the ^{31}P spins (**Figure 4.1**). Each of the 12 SAT pulses is followed by a spoiler gradient to enhance saturation and reduce echo formation using multiple gradient orientations [27]. After a saturation recovery delay (TSR), an FID is collected. TSR is stepped from one acquisition to the next to sample the T_1 recovery process. The set of TSRs chosen consisted of 2, 4, 8, 16, 32, 64, 128, and 256 s, resulting in a total scan time of 8.5 min. A $^{1}H/^{31}P$ dual-frequency birdcage coil (Rapid Biomedical, Rimpar, Germany) was used. At

maximum allowable peak power, a 60° nominal flip angle could be achieved at 120 μs pulse duration, which is less than ^{31}P T_2 in bone mineral. This flip angle was used for both saturation and excitation.

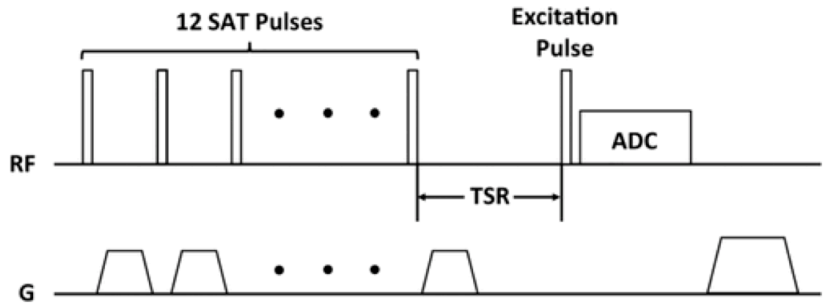

Figure 4.1 Diagram of the SR-prepared spectroscopy sequence, consisting of a saturation block of twelve 120-μs 60° hard pulses, 2 ms apart, and each followed by a spoiler. Spoilers are applied along different orientations for optimal de-phasing [27]. After a delay of TSR, signal is excited with another 120-μs 60° hard pulse and an FID is acquired at 250 kHz bandwidth. For further details, see text.

Bloch equation simulations showed that twelve 60° constant-phase RF pulses can achieve > 99.5% saturation for ^{31}P from both bone and metabolites. Signal was acquired 20 μs after excitation with a dwell time of 4 μs, and a total of 4096 data points were collected. However, the first eight points affected by coil ringing during transmit/receive switching were removed before reconstruction.

Whole-volume spectroscopy with short non-selective RF pulses was indicated to capture the short, low-SNR ^{31}P signal. However, this approach entails two potential problems: First, because the signal is the integral over the entire sensitivity region of the transmit/receive coil, ^{31}P signal from all tissues is detected, not only from bone. As demonstrated in **Figure 4.2**, ^{31}P peaks from muscle metabolites are superimposed on the

broad bone spectrum. Accurate measurement of bone phosphorus requires proper isolation of the bone peak from all other phosphorus signals. Second, whole-volume measurement is sensitive to B_1 inhomogeneity, which could adversely affect saturation. Both issues were investigated via simulation as well as experiment.

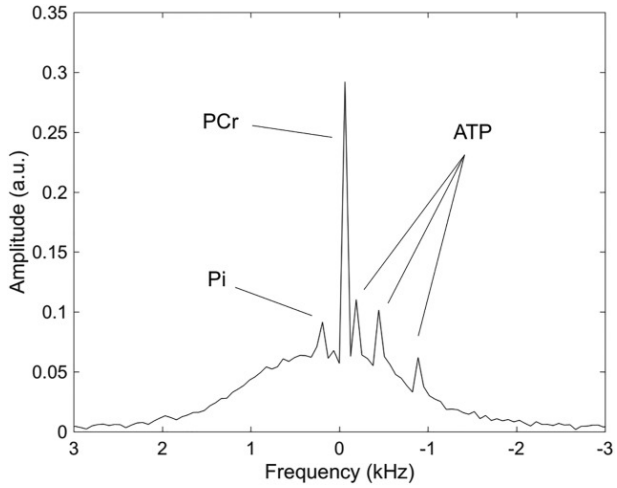

Figure 4.2 *In vivo* ^{31}P spectrum obtained from the calf of a healthy subject at 3 T. The broad peak corresponds to the ^{31}P in bone mineral, while the superimposed narrow peaks are from muscle metabolites.

4.3.2 Isolation of the Bone ^{31}P Spectrum

In order to separate the bone spectrum from the composite signal shown in **Figure 4.2**, a spectral subtraction method was used, yielding two spectra at each TSR during post-processing. Removal of the first 150 data points (corresponding to fast-decaying bone signal) from each FID results in a spectrum dominated by the much narrower metabolite signal components (Spec_Metabolite). The other spectrum was generated after removing 150 points from the end of the original FID, resulting in a composite spectrum consisting of both bone and metabolite peaks (Spec_Total). In this manner, both FIDs have the same

number of data points. After appropriate phase correction (both zeroth and first order), subtraction between the real parts of the two spectra yielded the bone ^{31}P spectrum (Spec_Subtract). Subsequently, the bone ^{31}P spectrum from each TSR was fitted to a Lorentzian. The processing steps are schematically illustrated in **Figure 4.3**. The total peak area is then fitted to the three-parameter model to estimate T_1 (**Equation 4.1**):

$$S = S_0 \cdot (1 - (1 - Q) \cdot e^{\frac{-TSR}{T_1}}) + N, \quad [4.1]$$

Where S_0 is the equilibrium signal of bone ^{31}P; Q represents the proportion of unsaturated ^{31}P spins in bone following the SAT pulses, which should ideally be zero for a perfect saturation; and N is noise. T_2* of bone ^{31}P was estimated as $1/(\pi \times \text{FWHM})$, for which FWHM is the full width at half maximum of the fitted Lorentzian. Although chemical shift anisotropy, homonuclear and heteronuclear scalar coupling are expected to cause deviations from Lorentzian line shape [90], we found the latter to be a reasonable approximation. Lastly, the Lorentzian conforms to the concept of T_2* as the time constant for mono-exponential decay.

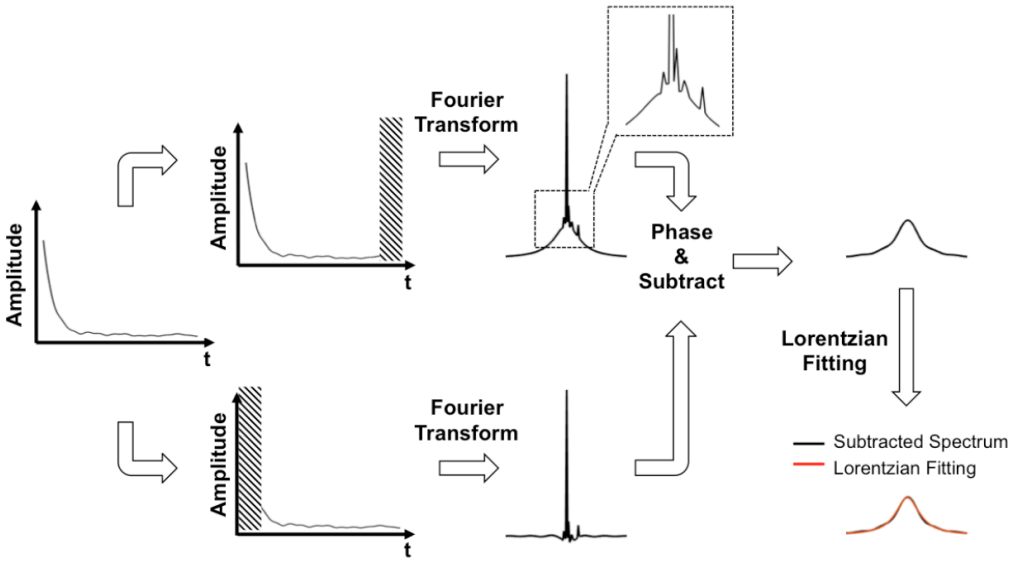

Figure 4.3 Workflow for isolating the bone ^{31}P spectrum from the composite signal containing both bone ^{31}P and ^{31}P metabolites. Spec_Total (overall signal) and Spec_Metabolite (predominantly metabolite signal) are generated from different portions of the FID. After phase correction, bone spectrum is obtained via subtraction of the two, which is subsequently fitted to a Lorentzian.

4.3.3 Simulation

Simulation experiments were carried out to investigate the accuracy of the proposed T_1 measurement method in the presence of ^{31}P-containing metabolites. Based on the *in vivo* ^{31}P spectrum observed both in this study as well as in the literature [91], five ^{31}P sources from metabolites — α-adenosine triphosphate (ATP), β-ATP, γ-ATP, PCr, and Pi — were considered. Chemical shifts of the metabolites were measured *in vivo*, whereas relaxation properties are based on values reported previously by Meyerspeer et al. [92]. T_1 and T_2* of bone ^{31}P were assumed to be 35 s and 200 μs based on an initial *in vivo* test scan. Bone ^{31}P concentration measured *ex vivo* by Seifert et al. [27], calf muscle metabolites concentrations measured *in vivo* by Kemp et al. [91], and volume of cortical

bone and muscle in the lower leg measured from conventional 3D gradient echo (GRE) images of four healthy subjects were used to estimate the proportions of bone and metabolites in the total signal. The simulation also incorporated B_1 field inhomogeneity along the z-axis (where most variation is expected for non-selective whole-volume measurements). The volume coil used is of a fixed birdcage design, with an inner diameter of 17.6 cm that is large enough to pass the foot through. It consists of two concentric-element coils, tuned to ^{1}H and ^{31}P, respectively. The two coils have the same physical size and number of rungs (eight), by are rotated relative to each other by 22.5°. Therefore, the B_1 fields of the two coils are expected to have similar characteristics. Because it is difficult to map the B_1 of the ^{31}P channel due to the inherently low SNR, the proton channel of the dual-frequency coil was used for B_1 mapping, which was accomplished with the Bloch-Siegert technique [93] by means of a homogeneous doped water phantom. Because the phantom was not sufficiently long to cover the entire sensitivity region of the coil, the measured B_1 profile was fitted to a Gaussian function to estimate B_1 in the missing outermost regions. Receive sensitivity (B_1^-) was assumed to be the same as transmit B_1 (B_1^+) from the principle of reciprocity as the same birdcage structure was used for both transmission and reception. Parameters of the simulated SR sequence were the same as described above.

4.3.4 *Ex Vivo* Validation

For further validation, two sets of *ex vivo* experiments were performed on a 3 T (49.9 MHz) TIM Trio system (Siemens Medical Solutions, Erlangen, Germany) with the $^{1}H/^{31}P$ dual-frequency coil. The first experiment was aimed at investigating the effect of inhomogeneous B_1 on the accuracy of T_1 measurements. Four lamb tibiae (with soft

tissue and articular cartilage removed) were cut into small sections of approximately 5 cm length, and T_1 and T_2* were measured with two different specimen placements: 1) all bone fragments were positioned within about 5 cm from the coil center, at which location the flip angle should be close to the nominal value; and 2) the fragments were evenly distributed ± 20 cm along the coil axis, which represents the entire sensitive region of the coil (**Figure 4.4a**), in order to cover the range of flip angles from the nominal value to near zero. In the second experiment, the performance of the proposed method for bone signal isolation was evaluated. To this end, a lamb hind leg, including femur, tibia, and surrounding muscles, was scanned in two different ways. T_1 and T_2* measurements were first done with soft tissue intact and the scan centered at the tibial mid-shaft. This measurement was repeated for four times with repositioning each time to test repeatability. Subsequently, the surrounding soft tissues (mostly muscle) were removed and the femur and tibia were harvested. The relaxation times of the two specimens were measured separately, with the specimen aligned along the long axis of the coil. Each bone was scanned three times with repositioning. These measurements were carried out within 24 hours of soft tissue removal, and caution was taken to maintain the hydration level of the bone during storage as well as the experiment. All specimens were collected from freshly slaughtered animals from the local market.

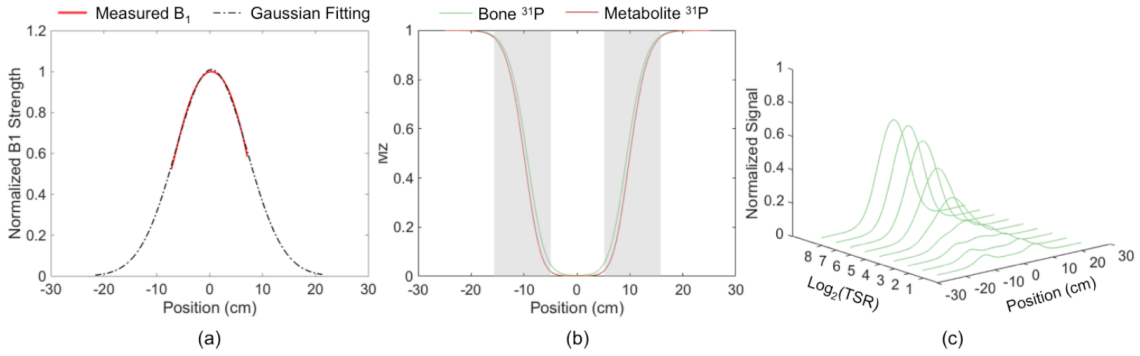

Figure 4.4 (a) Measured B_1^+ profile along z-axis of the coil and the fitted Gaussian. (b) Simulated saturation profile following the SAT module of the SR sequence in the presence of B_1^+ inhomogeneity depicted in (a) for different ^{31}P signal sources. (c) Relative amplitude of the signal as a function of spatial location plotted versus TSR. The pair of small peaks appearing at the shorter TSRs is due to incomplete saturation at the most distal coil locations.

4.3.5 *In Vivo* ^{31}P Imaging and Quantification

Ten healthy subjects of both genders (two males, eight females; age range: 26–76 years; mean (SD) = 50.4 (16.6) years old, BMI < 30) were recruited under an IRB-approved protocol. For each subject, the left mid-tibia (centered at 38% of tibia length from medial malleolus, where the cortical bone is the thickest [27]) was imaged with the same MRI system and coil used for the *ex vivo* experiment. After localization, ^{31}P transmit power was calibrated manually by incrementing the flip angle and maximizing the equilibrium calf muscle phosphocreatine signal [84]. Next, the SR-prepared spectroscopic sequence described above was applied to measure T_1 of bone ^{31}P. Three-dimensional ^{31}P images were subsequently acquired with a custom-designed ZTE-PETRA pulse sequence [84]. The ^{31}P ZTE-PETRA sequence was optimized for the experimentally observed relaxation parameters. Initial test scans in the tibia indicated an approximate bone ^{31}P T_1 of around 35 s. Therefore, flip angle was set to the Ernst angle of 5.3° (16-μs hard pulse) for a 150

ms TR. Sampling frequency bandwidth was 125 kHz, filling 3D spherical k-space with 8000 spokes and 895 single point acquisitions (PETRA radius = 6, hence, the effective TE was dwell time × PETRA radius = 48 μs), resulting in a total scan time of 22.5 min. An FOV of $(250\ mm)^3$ was prescribed, and 50 points along each spoke were acquired for reconstruction, leading to a nominal isotropic spatial resolution of 2.5 mm. Additionally, a ^{1}H image at the same location was also acquired with the manufacturer's 3D GRE sequence. From this, the tibial cortex was segmented using ITK-SNAP [94] to derive the bone volume, which was used for ^{31}P density calculation. Aside from the localizer and the 3D GRE sequence, all custom sequences were implemented in SequenceTree [95].

^{31}P ZTE-PETRA image data were acquired in the presence of a synthetic hydroxyapatite reference sample (Sigma-Aldrich, St. Louis, MO) with a known ^{31}P density of 9.5 mol/L (T_1 = 42.2 s, T_2^* = 145 μs) placed adjacent to the tibia. Following image reconstruction, signal intensity of cortical bone was compared to that of the reference sample to determine the amount of ^{31}P in bone as described in **Equation 3.1**, where I_{ref} and I_{bone} are image intensities measured within the reference sample and cortical bone. Whereas F_{ref} and F_{bone} (**Equation A 3.1**) are calculated steady-state signals using the respective relaxation properties given, where f_{xy} (**Equation A 3.2**), f_z (**Equation A 3.3**) are the mapping functions that describe the response of the magnetization to a constant-amplitude RF pulse, applicable when the pulse width s is comparable to or less than T_2^* [96]. Bone ^{31}P meets these requirements [27, 84] and, under some conditions, also those of bone water constituents [73].

To investigate repeatability, the above protocol was performed three times in three of the ten subjects, with repositioning between scans. Coefficients of variation were calculated

for cortical bone volume estimated from ITK-SNAP segmentation, relaxation times, and density of bone ^{31}P for each of the three test-retest subjects.

4.4 Results

4.4.1 Simulation

The B_1 field of the coil along its axis, measured by the Bloch-Siegert phase shift method [93] and the fitted Gaussian function, is shown in **Figure 4.4a**. **Figure 4.4b** depicts the simulated saturation profile for various ^{31}P-containing species in the presence of such B_1 inhomogeneity following the 12-pulse SAT module of the SR sequence. Due to the gradual decrease in the strength of the transmit field toward the edges of the coil, the saturation profile is characterized by a relatively large transition band (shaded area). As a result of its much shorter T_2, which causes the flip angle to deviate from the nominal value [97], the bone has a narrower full saturation region than that of the metabolites. **Figure 4.4c** shows the simulated profile of the received bone ^{31}P signal strength as a function of spatial location for different TSRs. It is worth noting that, although saturation is incomplete toward the edges of the coil due to rapid B_1 field drop-off, the contribution from the unsaturated spins is small because of the low coil sensitivity in those regions (**Figure 4.4c**).

Figure 4.5a shows the simulation results of the effects of metabolite signal fraction on the bone phosphorus relaxation times computed using the proposed spectral separation method and taking into account the B_1 inhomogeneity along the coil axis. T_1 is increasingly underestimated with increasing fraction of metabolite ^{31}P in the total signal, whereas T_2* is overestimated. If 15% of the total signal were to arise from metabolites,

the error in T_1 and T_2* would be approximately -10% and +24%, respectively. According to **Figure 4.5b**, which plots the error in quantified [^{31}P] as a function of T_1 and T_2* error, the above relaxation time errors result in [^{31}P] being underestimated by approximately 9.7%. Note that in the absence of metabolites, T_1 and T_2* errors are less than 1% and 3%, respectively, even in the presence of large B_1 field variations along the length of the coil.

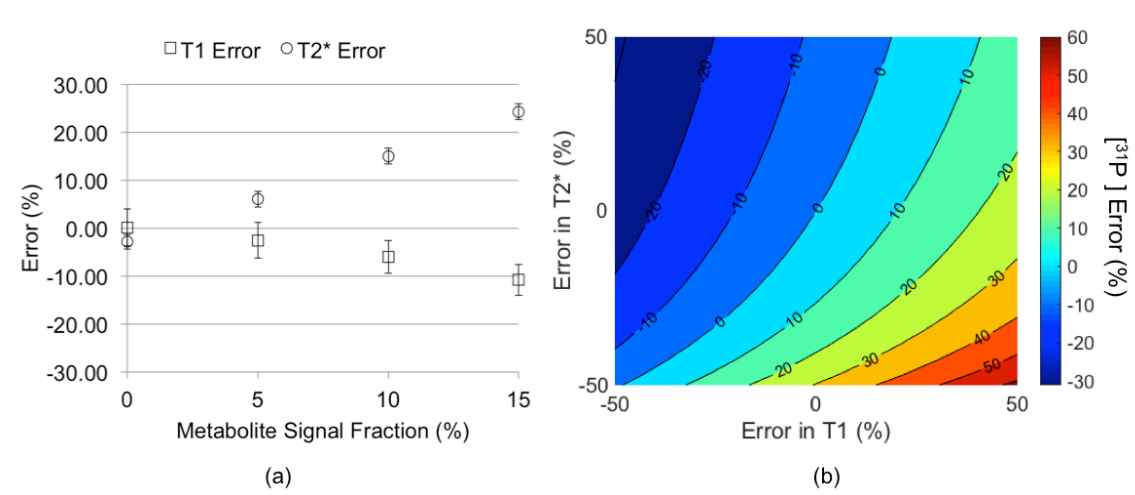

Figure 4.5 (a) Error in bone phosphorus relaxation times measured with the proposed method as a function of the fraction of metabolites in the total signal. (b) Error in quantified [^{31}P] as a function of error in T_1 and T_2*.

4.4.2 *Ex Vivo* Validation

In the *ex vivo* experiment that investigated the effect of B_1 inhomogeneity on relaxation measurement, the T_1 and T_2* were 26.7 s and 167.7 µs when all the lamb tibiae fragments were placed near the coil center. When the fragments evenly spanned the entire coil sensitivity region along its long axis, T_1 and T_2* were found to be 25.1 s and 173.6 µs, respectively. In the second *ex vivo* experiment that evaluated the impact of presence of soft tissue, the T_1 and T_2* of bone were 27.3 ± 0.6 s and 229.6 ± 1.5 µs, respectively, in

the presence of surrounding soft tissue. After soft tissue removal, T_1 and T_2* of tibia were measured to be 28.2 ± 0.8 s and 170.9 ± 0.8 μs, respectively, whereas those of femur were 26.7 ± 0.3 s and 168.7 ± 1.0 μs, respectively.

4.4.3 *In Vivo* ^{31}P Measurement and ^{31}P Quantification

Figure 4.6 illustrates the T_1 estimation using the proposed spectral separation method from an SR spectroscopic data set of one subject. **Figure 4.7** displays structural GRE images acquired from three subjects as well as the segmented tibia using ITK-SNAP for computing cortical bone volumes. Phosphorus images used for [^{31}P] quantification are also shown in **Figure 4.7**. Bone ^{31}P relaxation times and [^{31}P] measured for all ten subjects are given in **Table 4.1**. R^2 for Lorentzian fitting of the isolated bone spectrum (following subtraction of the metabolite spectrum) and subsequent mono-exponential T_1 fitting were greater than 0.97 and 0.99, respectively. To facilitate comparisons with x-ray based imaging modalities, **Table 4.1** also includes bone mineral density computed from our MR-measured [^{31}P], assuming $Ca_5(OH)(PO_4)_3$ as the mineral stoichiometry. Even though bone mineral was not measured independently by quantitative CT, the ^{31}P density-derived values are within the expected range of densitometric measurements.

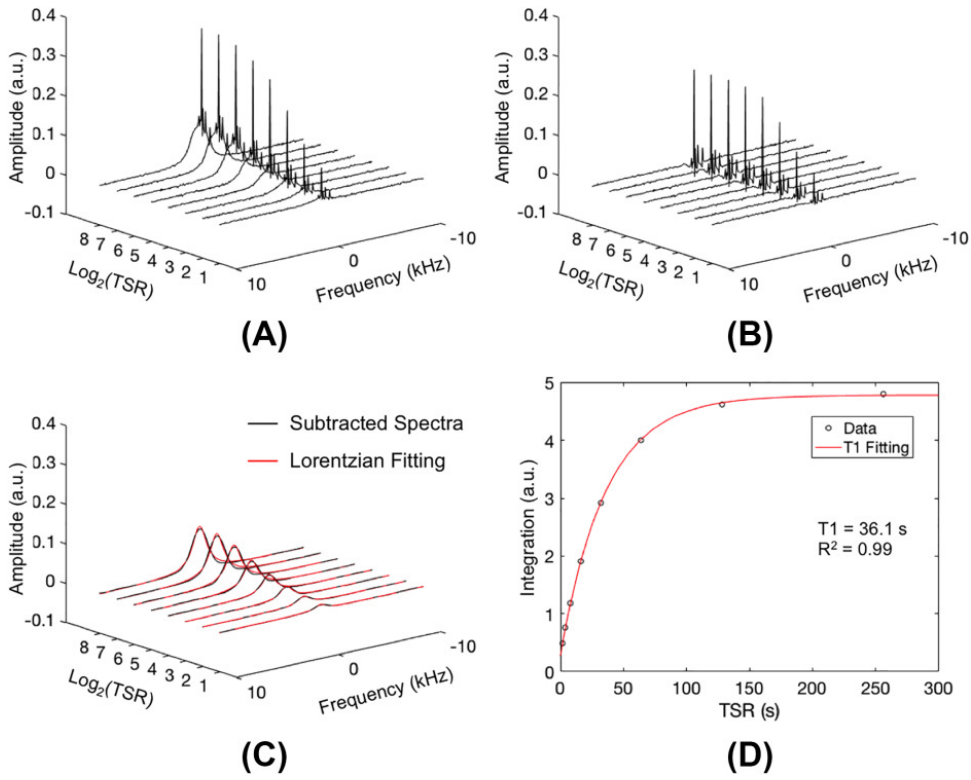

Figure 4.6 (a) Total and (b) metabolite spectra generated from an SR dataset of one of the subjects. (c) Isolated bone spectra and corresponding Lorentzian fits. (d) T_1 estimation via mono-exponential fitting of the integral of Lorentzian lines in (c).

Given the similarity in relaxation times across the ten subjects, ^{31}P concentrations were also computed using population-averaged T_1 and T_2* values, resulting in an average difference of about 2.4% compared to values computed using individually measured relaxation times. Because the muscle-to-bone ratio is expected to be largely invariant (e.g., Ref. [98]), a retrospective correction of the derived ^{31}P concentration, which accounts for the metabolite fraction, can also be applied. It is preferable, however, to apply the correction to the relaxation constants because the apparent ^{31}P concentrations are pulse sequence-dependent (**Equation 3.1** and **Equation A 3.1**). Doing so based on the 92.5% average bone ^{31}P fraction for the study group yielded T_1 and T_2* errors of

about -4.3% and +10.5%, respectively, resulting in a ^{31}P density error of approximately 4.6%. Relaxation times corrected for this error, as well as ^{31}P concentrations calculated using an average of the corrected T_1 and T_2* values, are given in **Table 4.1** too. None of the parameters — [^{31}P] ($P = 0.55$), T_1 ($P = 0.18$), or T_2* ($P = 0.99$) — was correlated with subject age. Coefficients of variation for cortical bone volume, T_1, T_2*, and [^{31}P] were 2.2%, 1.5%, 2.6%, and 4.4%, respectively (**Figure 4.8**).

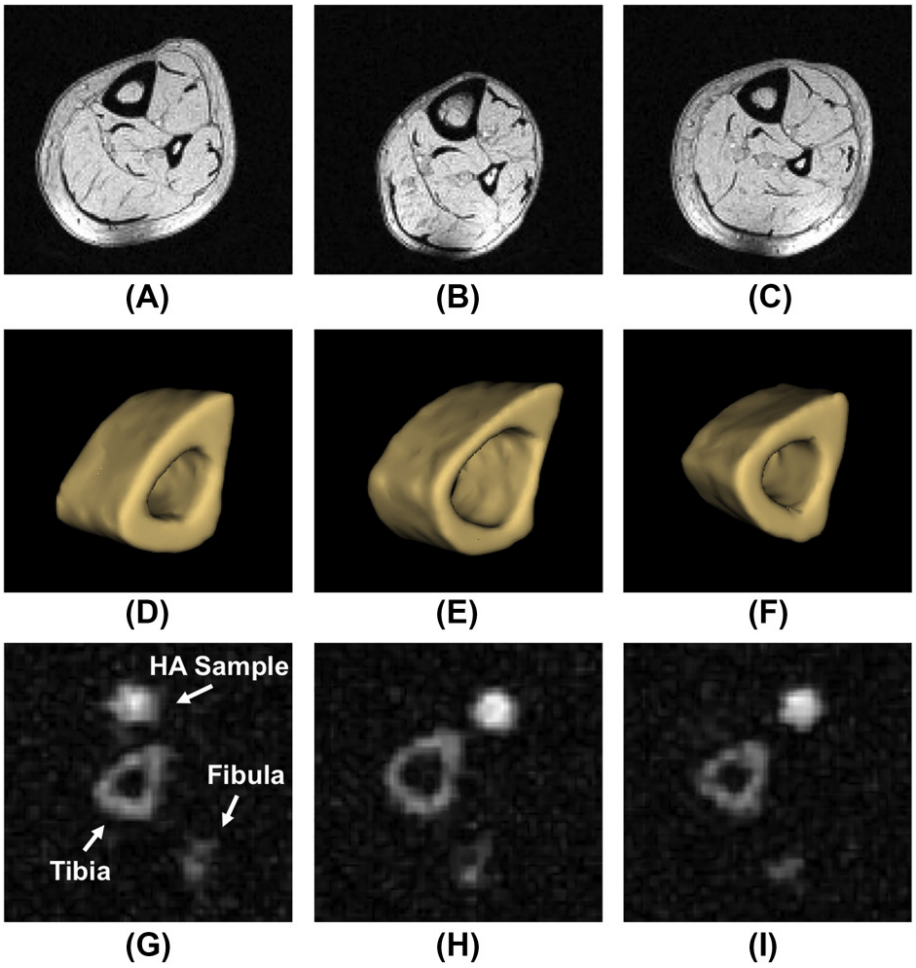

Figure 4.7 Axial 3D GRE images of the calf from (a) 30 y/o female, (b) 44 y/o male and (c) 51 y/o female. (d-f) Corresponding segmented cortical bone volumes. (g-i) ^{31}P ZTE image resulting from averaging of 18 slices.

4.5 Discussion

The present work sheds some light on the question of whether bone mineral ^{31}P T_1 and T_2* need to be measured individually to ensure quantitative accuracy in the measurement of phosphorus mineral density by solid-state MRI techniques or whether the use of global averages is adequate for quantification. The data obtained in the present work in the tibial cortex of ten healthy test subjects, ranging in age from 26 to 76 years, suggest only minimal inter-subject variations without a dependence on subjects' age or gender (**Table 4.1**).

Table 4.1 Cortical bone ^{31}P relaxation times and concentrations: MR = measured; CR = systematic error corrected using population-averaged relaxation times (for detail see text); $\Delta[^{31}P]$ (%) = estimated systematic error; BMD = bone mineral density computed from ^{31}P densities using stoichiometric calcium hydroxyapatite (for detail see text).

	MR		CR		$[^{31}P]$ (mol/L)		Error	BMD	
Age/Gender	**T_1 (s)**	**T_2* (µs)**	**T_1 (s)**	**T_2* (µs)**	**MR**	**CR**	**$\Delta[^{31}P]$ (%)**	**MR**	**CR**
26 M	36.1	185.7	37.7	168.1	5.56	5.81	4.50	931	973
30 F	35.7	202.7	37.3	183.4	6.45	6.94	7.60	1080	1162
33 M	34.7	213.9	36.3	193.6	5.97	6.61	10.72	1000	1107
44 M	38.7	190.1	40.4	172.0	7.57	7.68	1.45	1267	1286
51 F	37.8	191.8	39.5	173.5	6.50	6.69	2.98	1088	1120
58 F	37.6	188.6	39.3	170.7	5.92	6.08	2.70	991	1018
60 F	36.7	185.7	38.3	168.1	5.70	5.91	3.68	954	990
61 F	35.0	206.4	36.6	186.8	5.62	6.13	9.07	941	1026
65 F	36.9	206.5	38.6	186.9	5.61	5.96	6.24	939	998
76 F	38.5	198.4	40.2	179.5	6.02	6.19	2.82	1008	1036
Mean	**36.8**	**197.0**	**38.4**	**178.3**	**6.09**	**6.40**	**5.18**	**1020**	**1072**
SD	**1.4**	**10.0**	**1.5**	**9.0**	**0.62**	**0.58**	**3.09**	**103**	**98**

The measurement of the relaxation times, in particular T_1, was found not to be entirely straightforward. An image-based measurement, consisting of an appropriate SR preparation module preceding the ZTE excitation and readout, would be desirable because it would provide the spatial dependence of relaxation times. However, such an

approach is entirely impractical due to excessive scan times. We therefore elected a spectroscopic approach forgoing spatial selectivity, an approach previously chosen by Seifert et al. for T_1 quantification in human specimens [27]. The loss of spatial selectivity, one could argue, is acceptable given the systemic nature of most degenerative bone disorders. However, the presence of major muscle groups in the tibia poses unique challenges to the measurement of bone ^{31}P T_1 *in vivo*. The spectrum is a superposition of the spectra from bone and muscle phosphorus metabolites, and although the latter are far lower in concentration than mineral phosphate, this disparity is partially offset by the muscles' much larger volume. *In vivo* concentrations of three main ^{31}P-containing metabolites — PCr, Pi, and ATP — are approximately 33, 4.5, and 8.2 mM, respectively, in human calf muscle [91]. Average cortical bone ^{31}P concentration reported by Seifert et al. was 6.74 ± 1.22 mol/L in the tibial cortex of 16 donors, covering the entire adult age range [27]. These data, along with muscle and bone volumes estimated by standard GRE imaging in all ten subjects, suggest that tibial bone phosphorus accounts for > 90% of total amount of ^{31}P present *in vivo* at the tibial location. However, the much greater visibility of the metabolite signals, given their ^{31}P signal line widths being at least two orders of magnitude lower than those of the phosphate resonances from bone [92, 99], means that their contributions to the total signal cannot be ignored. Here, the authors made use of the large differential in T_2* between the two ^{31}P species and thus the lifetime of their FIDs for their separation. Another issue examined is the effect of RF inhomogeneity in the non-spatially selective measurement as the B_1 field falls off in axial direction from the center toward the coil boundaries, which raises the question as to the effectiveness of saturation of spins in more distant locations. However, the data obtained

by both simulation and experiment show that the 12-pulse saturation train is effective across a large range of excitation flip angles as they occur along the coil axis, yielding accurate T_1 and T_2* values in the absence of metabolites.

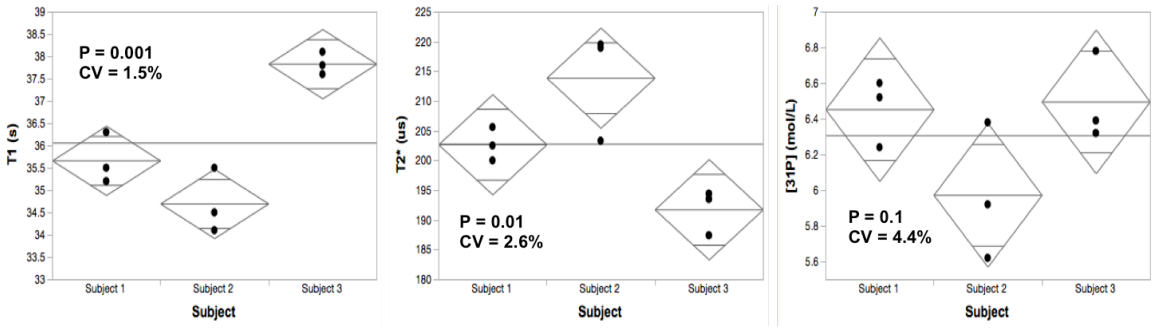

Figure 4.8 ANOVA analysis showing test-retest repeatability of bone phosphorus T_1, T_2* measured with proposed method, and bone phosphorus density estimated from ^{31}P ZTE image using measured relaxation times.

With bone comprising > 90% of the total signal, T_1 and T_2* errors are limited to about 6% and 15%, respectively (**Figure 4.5a**). The underestimation of T_1 and overestimation of T_2* both lead to lower computed phosphorus density. Because ZTE-PETRA is essentially a steady-state GRE sequence (**Equation A 3.1**), and therefore inherently T_1-weighted, lower computed T_1 translates into a higher calculated steady-state signal level (F_{bone} in **Equation 3.1**), and therefore lower estimated ^{31}P density, which scales as the ratio of observed image intensity to its predicted steady-state value. Overestimated T_2*, according to **Equation 3.1** (due to the exponential term), will also translate into lower computed ^{31}P density.

Several observations are worth noting from the specimen experiments. First, the very similar values of T_1 and T_2* obtained from the two arrangements of tibia specimens

confirm the simulation results, indicating that relaxation measurements are relatively insensitive to B_1 inhomogeneity. The likely reason for this finding is that, although inhomogeneous transmit fields cause imperfect saturation, the unsaturated spins have relatively small contribution to the total detected signal due to lower coil sensitivity in those regions. This holds true as long as the same coil is used for both transmission and reception, due to the principle of reciprocity, as it applies to the birdcage coil used. The close agreement between the bone T_1 values measured in the presence of soft tissue (27.3 ± 0.6 s) and those measured with soft tissue removed (tibia T_1 = 28.2 ± 0.8 s; femur T_1 = 26.7 ± 0.3 s) confirm the effectiveness of the proposed method at isolating bone spectrum from the composite signal. Furthermore, the T_1 values of lamb cortical bone measured *ex vivo* in the current study are consistent with those reported previously by Seifert et al. (T_1 = 26.0 ± 1.4 s; T_2* = 189 ± 2.2 μs), which were also obtained from the same animal species, anatomic location, and field strength [41]. However, the obviously elevated T_2* of bone in the presence of soft tissue is consistent with the result of the simulation experiment and may lead to underestimation in [^{31}P].

As noted above, the variation of T_1 across subjects (age range = 26–76 years) observed in this study is unexpectedly small (38.4 ± 1.5 s), a result suggestive of little variation in chemical makeup of the mineral over adult life. In fact, as noted above, there was no T_1 versus age correlation. This finding is consistent with the relatively small variation in T_1 for a group of 16 tibia specimens from donors aged 27 to 97 years (96.7 ± 10.8 s measured at 7 T), in which T_1-age correlation also was not found [27]. These observations indicate that relaxation measurements for bone ^{31}P quantification may be unnecessary. In addition, group average [^{31}P] quantified in the present study (6.40 ± 0.58

mol/L) is close to measurements *ex vivo* for a similar age range (6.74 ± 1.22 mol/L) [27] in which the experiment was free from interference of metabolites signal. For comparison, bone ^{31}P was also quantified using relaxation times reported by Wu et al. (T_1 =18 s; T_2* =160 μs) [42], yielding an average [^{31}P] of 4.9 mol/L for the ten subjects, which is around 20% lower as predicted (**Figure 4.5b**). Bone ^{31}P relaxation times published by Wu et al. were also used in an earlier work that investigated the feasibility of MRI-based bone matrix and mineral evaluation [84], and the average [^{31}P] of 5.29 mol/L found in the group of subjects for that study was likely an underestimation based on the relaxation data of the current study.

The absence of an association with age of the ^{31}P mineral density is unexpected but likely due to limited power with N = 10 subjects (despite the intentionally chosen relatively large age range). Interestingly, an earlier *ex vivo* study of mid-tibia specimens (N = 16) from donors aged 27 to 97 years showed the expected negative correlation of MR-measured bone phosphorus density with age ($R^2 = 0.39$, $P < 0.05$) [27]. However, when specimens of donors aged > 76 years are removed from their analysis, significance disappears (N = 11, $R^2 = 0.14$, $P = 0.26$). Thus, it is likely that an age dependence of phosphorus density would be observed for a greater number of study subjects or by expanding the age range.

Previously, Wu et al. performed both spectroscopic and image-based ^{31}P T_1 measurement of the bones in the wrist *in vivo* at 3 T. In their experiment, the steady-state ^{31}P signal was acquired by progressively increasing TR (0.5, 1, 2, 3, and 5 s). A T_1 range of 17 s to19 s was reported in two healthy subjects, which is about half the value found in the current work (average of 38.4 s in ten subjects). In contrast, *ex vivo* experiments by Seifert et al.,

T_1 of ^{31}P in lamb tibia yielded 26 s and 66 s at 3 T and 7 T, respectively, whereas T_1 of ^{31}P in the human tibia was found to be 96.7 s at 7 T [27, 41]. Because the T_1 of human bone is longer than that of lamb bone at 7 T, it is reasonable to expect a qualitatively similar relation at 3 T. Therefore, our value of 38.4 s is likely to be more accurate (> 26 s). There are several possible reasons for the disparity with our data: First, their spectroscopic measurement might have been affected by metabolite signal (**Figure 4.5a**), although the fraction of soft tissue is much less in the wrist than in the calf. Second, the relatively narrow range of TRs used, in particular the lack of a value close to equilibrium (two to three times T_1), is well known to underestimate T_1 with the progressive saturation technique, although an image-based measurement should be relatively immune to metabolite interference.

4.6 Conclusion

Quantification of bone ^{31}P concentration is critically dependent on T_1 and T_2*, which were measured *in vivo* in the tibia at 3 T field strength. The results show the two parameters to vary insignificantly across the adult age range, therefore obviating the need for subject-specific measurements.

CHAPTER 5: IMPACT OF GRADIENT IMPERFECTIONS ON BONE WATER QUANTIFICATION WITH UTE

5.1 Abstract

Purpose: The impact of gradient imperfections (time delay and eddy current) on UTE images as well as UTE image-based bone water quantification was investigated at 3 T field strength.

Methods: Simulation and phantom scans were performed to first study the effect of simple time delay on UTE image, and subsequently the effect of eddy current as well as the combined effect of eddy current and time delay. Healthy subjects were scanned to determine how is the bone water quantification influenced if the gradient errors are left uncorrected, only time delay is corrected and both delay and eddy current are corrected. *In vivo* experiments were also performed on two Siemens Trio systems to investigate the impact of such gradient imperfections on measurement agreement between scanners.

Results: Gradient delays from -1.3 μs to 3.9 μs were measured using Rapid birdcage calf coil and 12-channel Siemens phased array head coil on two Siemens 3 T Trio scanners. Total water, bound water and pore water were up to 17%, 2.2% and 52% off from value derived from fully corrected images if no correction is performed, while up to 10.8%, 2.2% and 32% off if only correcting for delay. Mean coefficient of variation between measurement from two Siemens Trio systems are 7.5%, 5.6% and 10.5% for total water, bound water and pore water without correction, 0.9%, 3.0% and 4.8% with delay correction only, and 1.3%, 2.7% and 7.8% with full trajectory correction.

Conclusion: k-Space trajectory mis-mapping due to gradient imperfections imposes spatially dependent artifact on UTE images, which compromise not only the bone water quantification accuracy but also undermines the inter-scanner measurement agreement if left unaccounted for.

5.2 Introduction

A number of studies in recent years have provided evidence that quantitative imaging of bone water with UTE and ZTE radial MRI is feasible [27, 29, 30]. Using similar technology, mineral phosphorus has been imaged by ^{31}P MRI in bone specimens [27, 31, 33] and also *in vivo* in humans [42, 44]. Collagen, the main component of bone matrix, is not directly visible by *in vivo* MRI due to its extremely short T_2* (tens of microseconds), however, the protons on water molecules bound to the matrix (bound water) are detectable [39, 40, 53, 70] and scale linearly with matrix density. Pore space in cortical bone can also be indirectly evaluated by capturing the signal from water residing within the pores (pore water) [39, 40, 53, 70]. Further, since phosphorus is a primary constituent of bone mineral (non-stoichiometric calcium hydroxyapatite), quantitative ^{31}P MRI can assess mineral density [42-44]. More recently, attempts have been made to quantify both bone water and bone mineral with an integrated *in vivo* protocol [84].

One potential problem with short-TE MRI techniques is caused by the radial acquisition scheme, which is more susceptible to gradient imperfections than their Cartesian counterparts [100-106]. Hardware related time delays and eddy current-induced waveform distortions [107] result in k-space trajectories deviating from their prescribed paths. In Cartesian scanning, k-space trajectory deviations are consistent between phase

steps and will only lead to an undetectable linear phase shift in magnitude images. In radial sequences the k-space trajectory error varies with view angle, and this inconsistent k-space encoding may result in artifacts in the magnitude image. Furthermore, since each view passes through the central k-space region and determines overall image contrast, signal intensity measurements could be adversely affected yielding inaccurate values. Importantly, the gradient imperfections are scanner hardware dependent, but once quantified, the gradient trajectory errors can be accounted for in the reconstruction code.

A number of techniques have been proposed to address this problem in UTE. Some are dedicated to the time delay correction only [106, 108], while others are designed to account for both the delay and waveform distortion [100, 106, 109-111]. Strategies correcting for both delay and eddy current generally fall into three categories. The first directly measures k-space trajectory along the three principal axes. Either a slice perpendicular to [100] or parallel with [109] the gradient direction is excited and the trajectory is tracked by following the phase evolution during the gradient ramp. The second category measures a finite portion of the readout gradient (including ramp) with a sequence designed to measure the gradient zeroth moment, from which the actual gradient waveform is extracted. The latter is subsequently used for UTE reconstruction [106]. A third category treats the gradient hardware as a system fully described by a gradient system transfer function (GSTF) or gradient impulse response function (GIRF), which can be measured either by a series of gradients of various shapes [110] or a single gradient waveform with broad frequency profile [111]. The actual gradient waveform, determined by operating the measured GSTF or GIRF on an ideal trapezoid shape, is applied to reconstruct the UTE image. However, to the best of the authors' knowledge,

except for the work by Latta et al. comparing relative proton density in brain white matter from images with and without trajectory correction [112], there has been no systematic investigation of how UTE image and image-based quantification are affected by gradient imperfections, and particularly, how such errors impact inter-scanner agreement.

This work is designed to evaluate the impact of gradient imperfections and consequential k-space trajectory mis-mapping on UTE image-based bone water quantification. Toward this end, simulation and phantom experiments were first performed to demonstrate image artifacts in the presence of different extents of k-space trajectory shift as well as the spatial dependence of the resulting artifacts. Bone water densities were then quantified and the results compared between human subject UTE images obtained without correction, with time delay correction, and both delay and eddy current correction. Finally, bone water densities obtained from two different MRI scanners were compared to evaluate the effect of image corrections on inter-scanner agreement.

5.3 Materials and Methods

5.3.1 Theory

Ignoring relaxation, the signal collected in an MRI experiment can be represented as

$$s(\boldsymbol{k}) = \int \rho(\boldsymbol{r})\, e^{-i2\pi \boldsymbol{k}\cdot\boldsymbol{r}}\, d\boldsymbol{r} \qquad [5.1]$$

with $\rho(\boldsymbol{r})$ being the position-dependent spin density, and $\boldsymbol{k}(t) = \frac{\gamma}{2\pi}\int \boldsymbol{G}(t)$, the time-dependent spatial frequency vector. The argument of the exponential in **Equation 5.1** denotes the instantaneous phase $\varphi(t) = 2\pi\, \boldsymbol{k}(t)\, \boldsymbol{r}$ of the k space signal at position $\boldsymbol{r}$. After appropriate re-gridding (as required, for instance, in radial encoding) the image

typically is reconstructed as the inverse Fourier transform of the k-space (**Equation 5.2**):

$$\rho(\boldsymbol{r}) = \int s(\boldsymbol{k})\, e^{i2\pi \boldsymbol{k}\cdot\boldsymbol{r}} d\boldsymbol{k} \qquad [5.2]$$

However, a realistic reconstruction requires accurate knowledge of the k-space trajectory, which is susceptible to inaccuracies in the gradient waveform $\boldsymbol{G}(t)$. Due to hardware imperfections such as time delays and effects of eddy currents, the actual gradient $\boldsymbol{G}'(t) \neq \boldsymbol{G}(t)$, i.e. the encoding gradient deviates from the prescribed waveform, and as a result, image quality is compromised by the mis-mapping of k-space data points.

In the following sections we illustrate the problem with actual data and describe a method for gradient waveform correction in UTE imaging, with a particular focus on quantification of bone water.

5.3.2 Gradient Delay, k-Space Trajectory Measurement and UTE Image Correction

The k-space trajectory was measured with an extension of the mapping technique disclosed in abstract form [109]. The technique was originally proposed to map x- and y-trajectories for 2D UTE, and was extended in this work for measurement along all three principal axes (**Figure 5.1a**). First, a 2D slice (5-mm thick) parallel to the targeted gradient direction was excited and phase-encoded along both directions, followed by a ramp-readout that is to be used for the UTE sequence. The two phase-encodings generate a series of 2D images, each corresponding to a single time-point along the readout gradient direction. Due to the presence of the gradient, each of these images presents a linear phase in the same direction, which progressively accumulates depending on the order of the image in this sequence (**Figure 5.1b**). From the phase $\varphi(r,t) = 2\pi\, k(t)\, r$,

the slope of the straight line fitted to the linear pattern on each of these phase maps corresponds to the instantaneous k-space location, which is proportional to the zeroth gradient moment (**Figure 5.1c**). The true gradient waveform is simply the time derivative of the gradient moment curve (**Figure 5.1d**). This measured k-space trajectory embodies the effects of both time delay and eddy current-induced waveform distortions. To determine the time delay, the mid-point of the linear portion of the ramp on the measured gradient is compared to the mid-point of ramp on a nominally trapezoidal gradient (**Figure 5.1e**). The measured trajectory or gradient delay can thus be used for either full trajectory correction or delay only correction during image reconstruction. For full correction, trajectories along three principal axes are measured as described above, while the ones along oblique directions are represented as linear combinations of them. This is because the gradient system can be regarded as linear time invariant [113]. Image is subsequently generated by re-gridding reconstruction. For delay only correction, trajectories of principal axes are calculated from assumed trapezoid gradient waveform, but with measured delay incorporated. The oblique trajectories are obtained in the same way as in full trajectory correction. For the most accurate measurements of k-space trajectories and gradient delays, scan parameters such as FOV, dwell time and gradient ramp times should be matched to those of the actual UTE imaging sequence.

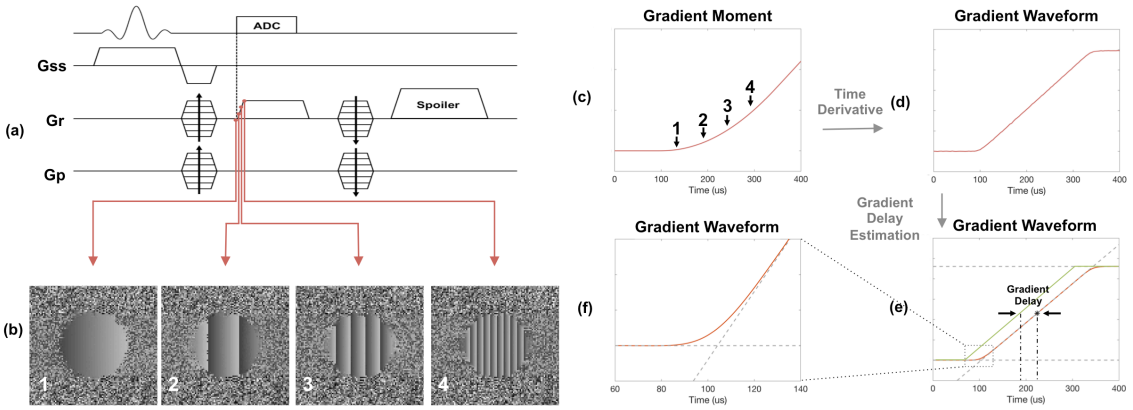

Figure 5.1 (a) Trajectory mapping sequence based on the technique proposed in [109]. (b) Phase maps acquired during ramp-up of the readout gradient. (c) Zeroth moment of the readout gradient (k-space trajectory) obtained by linear fitting the pattern of the phase maps along the gradient direction. (d) Time derivative of the gradient moment yields the true gradient waveform. (e) Gradient delay determined by comparing the mid-point of the measured gradient ramp with that of the ideal gradient (green line). (f) Actual gradient waveform deviates from nominal trapezoid due to eddy currents.

5.3.3 Simulation Experiments

Two sets of simulation experiments were performed. The first was to demonstrate the overall effect of various k-space shifts on the UTE image. Trajectories along the principal axes were calculated based on ideal trapezoidal gradient waveforms. Delays of -6 µs to +6 µs (hardware delays typically observed on clinical scanners [102, 108]) were introduced along the x-direction in 2-µs increments. Thereafter, the entire k-space was created as their linear combination. A more realistic scenario was simulated in the second experiment, where the actually measured delays and trajectories were used. Assumed scan parameters were: FOV = $(250\ mm)^2$, dwell time = 4 µs, ramp time = 240 µs; 158 points along each FID were collected to reconstruct an image of matrix size 256x256. Images were reconstructed as described in [114]. Two types of phantoms were

considered: (1) a single large cylindrical object (110 mm diameter, resembling the standard Siemens cylinder phantom) placed at the FOV center, and (2) five smaller cylindrical objects (18 mm diameter) placed in a row along the x-axis, to investigate the spatial dependence of image artifacts.

5.3.4 Phantom Imaging Experiments

Phantom experiments were performed on a Siemens 3 T Trio system (Siemens Medical Solutions, Erlangen, Germany) using a 3D UTE sequence. The standard Siemens cylindrical phantom (3.75 g $NiSO_4 \cdot 6H_2O$ + 5 g NaCl per 1000 g H_2O) was imaged with a birdcage calf coil (Rapid Biomedical, Rimpar, Germany) custom-made for ^{31}P and ^{1}H bone imaging of human subjects. In addition, five test-tubes of doped water (18 mm diameter, 20% H_2O/80% D_2O, doped with 27 mmol/L of $McCl_2$ to achieve a H_2O concentration of 11 mol/L, proton T_1 = 4.5 ms, T_2* = 327 μs) that served as ^{1}H density calibration samples in an earlier *in vivo* bone water quantification study [84] were imaged with a wider vendor supplied 12-channel Siemens head coil to evaluate the spatial dependence of gradient-waveform related artifacts. Scan parameters matched those in the simulation experiments. Following data acquisition, images were reconstructed in three ways: 1) no correction, 2) correction for gradient delay only (delay correction), and 3) correction for both delay and eddy current (full trajectory correction). In addition, the same series of delays used in the simulations were intentionally introduced into the full trajectory corrected k-space data to demonstrate the influence of varying delays on actual experimental data. All resultant images were compared with simulations.

5.3.5 *In Vivo* Imaging Experiments

To investigate the impact of gradient imperfections on bone water quantification, data acquired from a previous study in ten healthy subjects ranging in age from 29 to 65 years [84] were corrected with the measured gradient delay and k-space trajectories. The left mid-tibia of each subject was co-imaged with one ^{1}H calibration sample as mentioned above. Total bone water and bound water were imaged with ^{1}H UTE and ^{1}H rapid inversion recovery-prepared UTE (IR-rUTE) respectively. Following reconstruction, the pixel intensities within the mid-tibia cortex were compared to that within the calibration sample, after accounting for the different relaxation times, to determine bone water concentration. For comparison, the different bone water pools were quantified from images without correction, with delay correction only and with full k-space trajectory correction. To investigate the impact of gradient imperfections on inter-scanner quantification agreement, the above procedure was performed once, on two Siemens Trio systems, on three separate subjects. The agreement in bone water densities obtained from the two scanners was compared with and without image correction. Both the phantom and *in vivo* images were reconstructed using the same algorithm used for the simulation.

5.4 Results

5.4.1 Effects of Simple k-Space Shift on UTE Image

Simulated and experimentally acquired UTE images of a standard Siemens cylindrical phantom after introduction of gradient delays are shown in **Figure 5.2**. Most prominent are the edge effects, best seen in the profiles (**b**, **d**). Overall, there is close agreement between simulation and experiments except for some additional intensity modulation on

the experimentally acquired images (best visible on the profiles in **Figures 5.2b** and **d**), potentially caused by dielectric effects [115], as well as varying proximity to the coil elements. Intensity distortions worsen with increasing timing errors. Results from the five doped phantoms in **Figure 5.3** also reveal the high spatial dependency of these artifacts — the farther away an object is located from the FOV center, the more severe the distortion. The slightly elevated intensities observed for off-center samples on the experimental images is likely due to greater coil sensitivity at these locations.

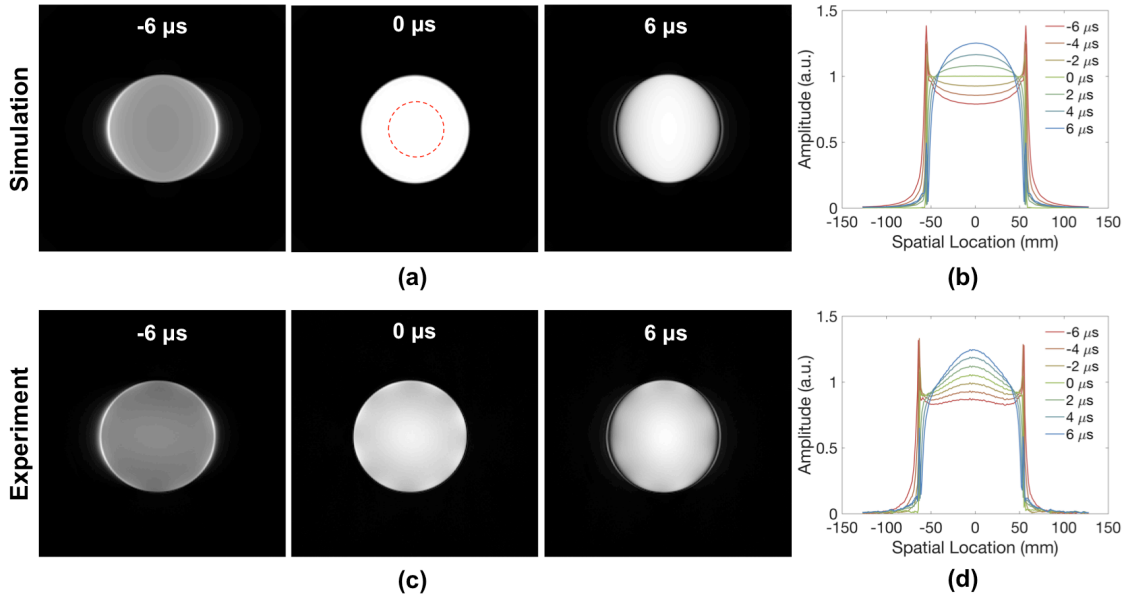

Figure 5.2 (a) Simulated and (c) experimentally acquired UTE images of a standard Siemens phantom in the presence of gradient delays up to ±6 µs along x-direction (left-right) and their horizontal cross-sectional profiles (b, d). Compared to the profile of simulated images, the slight unevenness of the signal intensity is likely due to B_1 inhomogeneity.

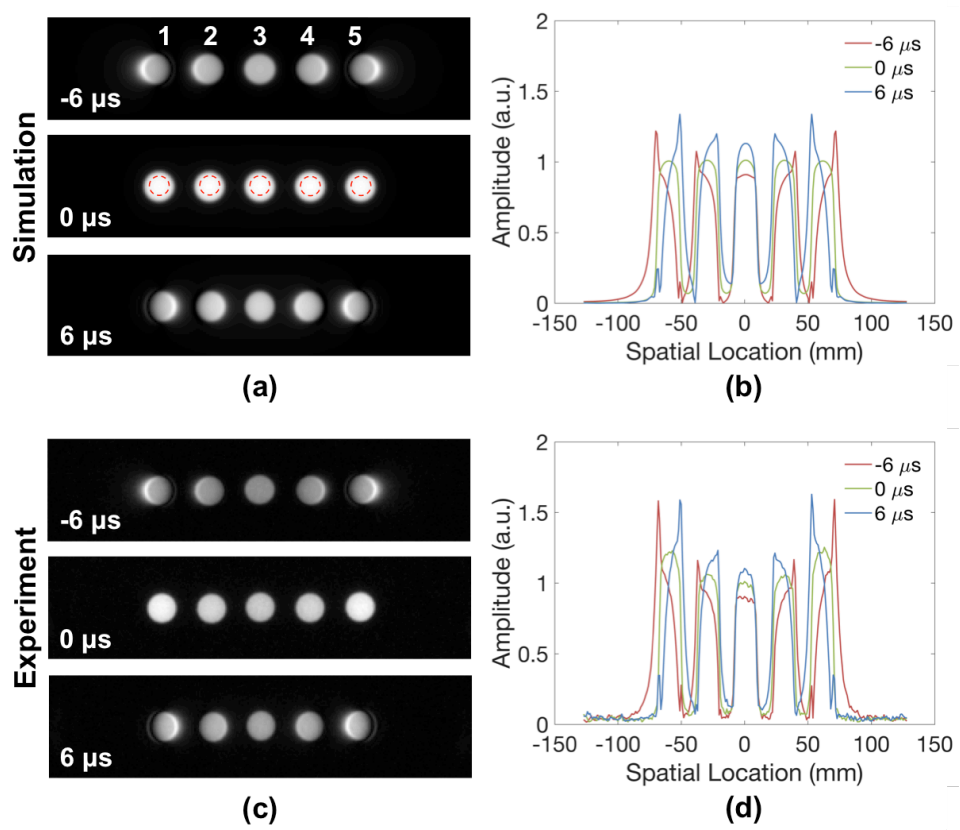

Figure 5.3 (a) Simulated and (c) experimentally acquired UTE images of five doped samples used for bone water calibration in the presence of different amounts of gradient delays along x-direction (left-right) and (b, d) their respective horizontal cross-sectional profiles. Greater signal intensities observed for the outer samples of the sample array images are likely due to increasing coil sensitivity nearer to the head coil elements.

To quantitatively determine the impact of such timing errors on image contrast, average intensities within the ROIs indicated in **Figure 5.2a** and **5.3a** (red dashed circles) were compared among images with and without gradient delay for each phantom. Fractional differences in intensity are summarized in **Table 5.1**. Close agreement is observed between the simulation and experimental data for both large and small phantoms. Interestingly, although intensity increases with positive gradient delay and decreases with negative delay for the inner samples, a net signal loss always occurs for the outer samples

as a result of greater image distortions farther away from the FOV center.

Table 5.1 Percent error in average intensity measured from ROIs in **Figure 5.2a** and **Figure 5.3a** as a function of gradient delay.

Phantom	Large		Small									
Delay (μs)	Simulation	Experiment	Simulation					Experiment				
			1*	2	3	4	5	1	2	3	4	5
-6	-20.2	-16.6	-24.0	-13.7	-9.5	-13.7	-28.7	-29.1	-15.0	-9.7	-16.2	-28.6
-4	-13.8	-11.2	-12.0	-8.3	-6.5	-8.3	-15.6	-16.0	-9.2	-6.6	-10.3	-15.1
-2	-7.0	-5.4	-3.6	-3.6	-3.6	-3.6	-5.4	-5.5	-3.9	-3.1	-4.4	-5.0
0	0.0	0.0	0.0	0.0	0.0	0.0	0.0	0.0	0.0	0.0	0.0	0.0
2	7.4	6.1	-2.4	2.4	3.6	2.4	0.6	0.0	2.4	3.1	2.9	-0.8
4	15.0	11.8	-10.8	4.2	7.1	4.2	-5.4	-5.5	3.4	5.6	3.9	-7.1
6	22.8	16.6	-25.7	3.6	10.7	3.6	-17.4	-15.6	3.4	7.7	3.9	-18.1

* Sample number as indicated in **Figure 5.3**.

5.4.2 Effects of Gradient Imperfections on Phantom UTE Images

The gradient delays measured with the various combinations of coils and scanners used in this study are summarized in **Table 5.2**. **Figure 5.4** illustrates the effects of eddy currents alone (after correcting for time delay) as well as the combined effect of delays and eddy currents (no correction at all) on UTE images via simulation and with actual experimental data. For the Siemens phantom, there appears to be some over-compensation for delay correction only. For the calibration samples, on the other hand, delay correction achieves an intermediate result between no correction and full trajectory correction.

Table 5.2 Gradient delays (μs) measured from two Siemens 3 T Trio scanners with two different coils.

Scanner	1		2
Coil	Rapid	Siemens	Rapid
X Gradient	2.2	0	2.8
Y Gradient	1.0	-1.3	1.5
Z Gradient	1.0	-0.5	3.9

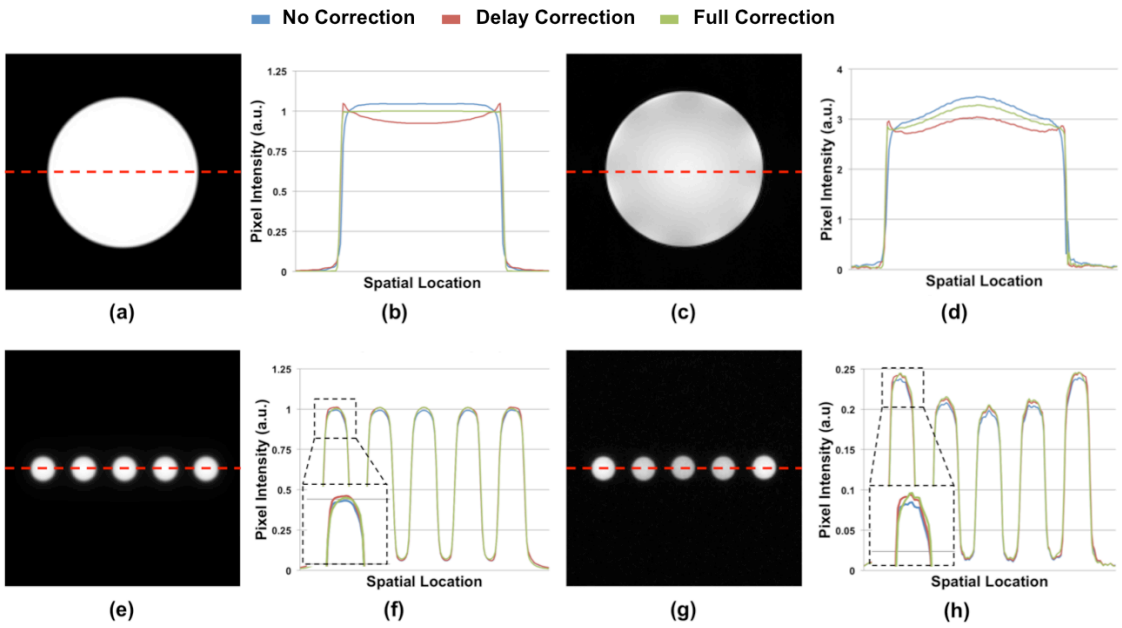

Figure 5.4 (a, e) Simulated and (c, g) experimentally acquired UTE images of Siemens phantom and calibration samples. (b, d, f, h) Profiles (as indicated by the red dashed line) taken from images reconstructed with no correction, with gradient delay correction only, and with full trajectory correction are compared.

5.4.3 Effects of Gradient Imperfections on *In Vivo* UTE Images

Figure 5.5 displays the UTE and IR-rUTE images of a healthy subject reconstructed with and without gradient imperfection compensation. A cross-sectional profile through the calibration sample and the subcutaneous fat-muscle boundary is also plotted. As before, although the shapes of profiles are improved after accounting for gradient errors, a slight 'over-compensation' was observed for delay only correction. **Table 5.3** lists the percent errors in bone water derived from images with no correction and delay only correction relative to that derived from images with full correction. **Figure 5.6** shows the percent variation in average pixel intensity within cortical bone and calibration sample with

respect to full trajectory correction. **Figure 5.7** presents *in vivo* results obtained from two different MRI scanners. Inter-scanner agreement is improved with correction, as suggested by the lowered coefficient of variation.

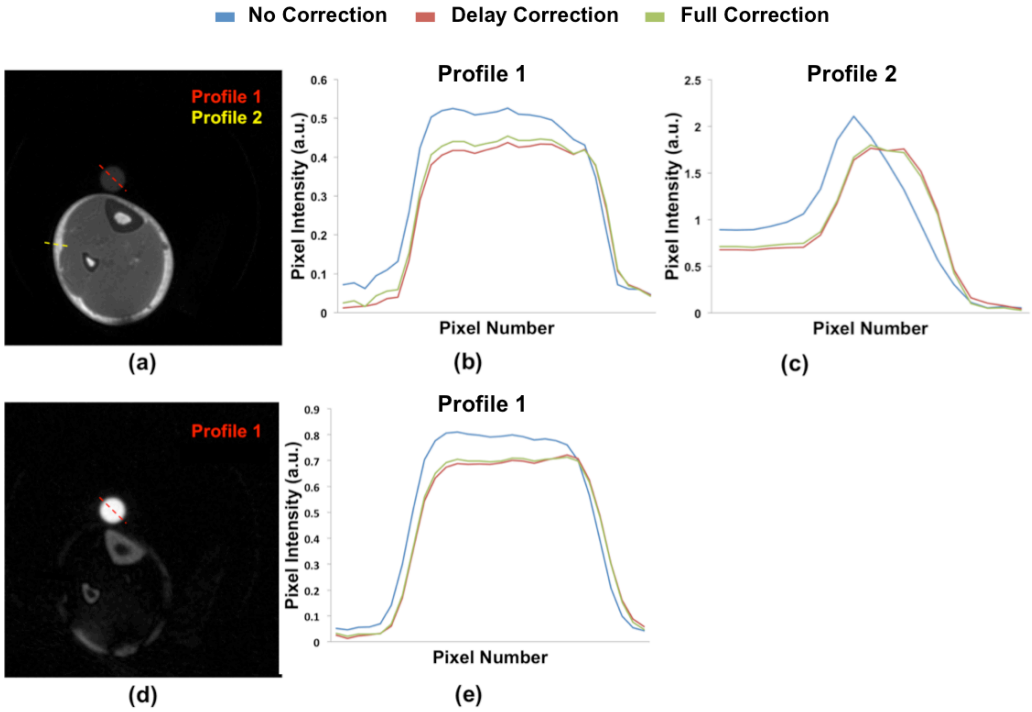

Figure 5.5 Axial view of 3D (a) UTE and (d) IR-rUTE images of the calf of a healthy subject acquired with dual-frequency calf coil. (b, c, e) Profiles as indicated in the cross-sectional images to illustrate effect of different reconstruction methods.

Table 5.3 Percent errors in bone water densities quantified from *in vivo* UTE images with no correction and delay only correction versus those with full trajectory correction.

	Total Water		Bound Water		Pore Water	
Subject	**A**	**B**	**A**	**B**	**A**	**B**
1	15.6	-10.4	0.0	-0.9	48.3	-30.0
2	16.6	-10.8	0.0	-1.9	52.0	-32.0
3	16.9	-10.1	1.7	-0.9	46.7	-28.3
4	13.9	-7.3	-2.2	-2.2	38.6	-17.5
5	15.7	-9.4	-1.0	0.0	34.8	-19.1
6	16.4	-8.5	-1.0	0.0	40.0	-20.0
7	16.2	-7.9	0.0	0.0	39.0	-19.5
8	17.0	-9.1	0.9	-0.9	49.2	-27.1
9	13.7	-7.7	2.1	-1.0	28.6	-15.5
10	14.1	-8.6	0.0	-0.9	43.6	-25.5

A: Uncorrected image relative to fully corrected image.
B: Delay corrected image relative to fully corrected image.

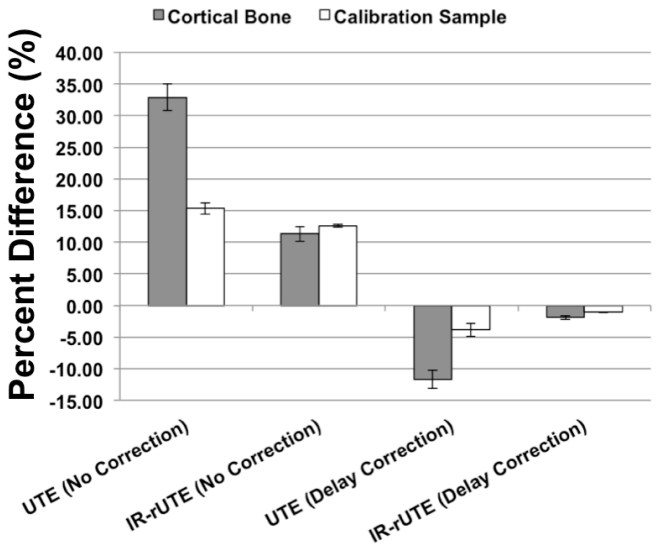

Figure 5.6 Percent difference in the average pixel intensity within cortical bone or calibration sample relative to the case of full trajectory correction.

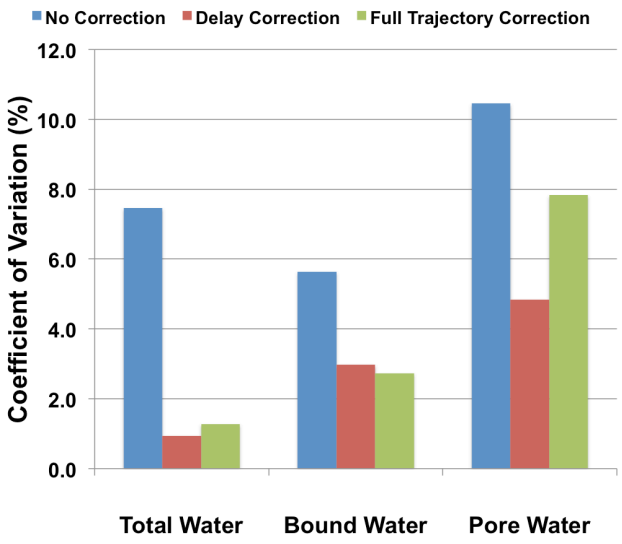

Figure 5.7 Average inter-scanner coefficients of variation from three subjects chosen to test the impact of image correction on the inter-scanner agreement.

5.5 Discussion

Reconstructing non-Cartesian MRI data requires re-sampling (or re-gridding) collected data points onto a Cartesian grid before Fourier transformation. However, k-space value at each time point during readout might deviate from the nominal one due to the influences of time delays and eddy currents [105, 107, 113 116]. Compared to other radial MRI techniques collecting full echo, UTE (center-out) is particularly sensitive to eddy currents in that the k-space center, which dominates the image contrast, is directly impacted by them [107].

As **Figures 5.4** and **5.5** suggest, correcting for time delay alone does not fully remedy the problem. Eddy current effects must also be taken into account. Delay only correction achieved an outcome intermediate between no correction and full correction for small phantoms imaged with the Siemens head coil (**Figure 5.4f** and **h**), while appearing to

overcompensate for the large phantom imaged with the Rapid calf coil (**Figure 5.4b** and **d**) due to the residual effect of eddy current-induced gradient waveform distortion following delay correction, being equivalent to a negative time delay (**Figure 5.1f**). After accounting for the positive x-delay that accompanied the calf coil, it is this eddy current-induced gradient distortion that remains. Conversely, the Siemens head coil did not have any delay to correct along the x-axis in the first place; the shape distortion observed in that direction (**Figure 5.4h**) is mainly due to the eddy current effects themselves. The increase in magnitude from profile with no correction to profile with delay only correction (**Figure 5.4h**) is due to correction of time delay existing in the other two directions (**Table 5.2**).

Both time delay and eddy current are analogous to radially translating k-space data, which imparts a phase in that direction in the image domain — the farther away from the isocenter, the greater the phase accumulated. Therefore, the image artifact demonstrates the same spatial dependency (most clearly seen in **Figures 5.2** and **5.3**). This is of importance to quantification because the positioning of a subject and the calibration sample may vary from scan to scan. The measured signal intensity within the tibial cortex and the sample may be affected to different extents depending on their spatial locations within the FOV in the absence of a correction. In addition, the distorted intensity profile of an uncorrected image (**Figure 5.3**) may also make quantification sensitive to ROI placement. Accounting for these gradient imperfections is expected to improve not only intra-subject test-retest repeatability, but also augment the sensitivity to differentiate bone water concentrations between subjects.

Furthermore, the gradient errors are not only direction-, but also hardware-dependent

(**Table 5.2**), and compensating for them does improve inter-scanner concordance (**Figure 5.7**). Before correction, the CVs of TW and BW between two scanners (7.5% and 5.6%) are higher than those reported in an earlier study performed on a single scanner (3.5% and 2.6%) [84], but are reduced to 1.3% and 2.7% respectively following correction.

Both **Table 5.3** and **Figure 5.7** indicate that the quantification of total water is more sensitive to k-space trajectory errors than bound water. The former is due to signal contamination from soft tissue in the absence of long-T_2 suppression. In UTE images, the signal from soft tissues (such as muscle and bone marrow) may be interfering with the signal from cortical bone in the presence of gradient error (**Figure 5.3**). In IR-rUTE images, on the other hand, soft tissues are suppressed and signal contamination is therefore not an issue. As a result, the intensity change in cortical bone is more consistent with that of the calibration sample in IR-rUTE (**Figure 5.6)**, leading to a less variable bound water quantification result (**Table 5.3**). By contrast, cortical bone had a drastically different change in intensity as compared to the calibration sample in UTE, and caused larger variations in total water quantification (**Table 5.3**).

Several trajectory correction methods able to handle both time delay and eddy current [100, 105, 106, 109-111] have been proposed for UTE. The technique designed by Magland et al. [109] was chosen for the current study because it is simple to implement, it does not rely on any models where assumptions might have been made, and it directly measures the trajectory of the exact gradient waveform used for UTE imaging.

Although the current study focuses on bone water quantification, the conclusions are equally applicable to evaluation of bone mineral. Both UTE and ZTE have previously

been explored as an alternative to CT for bone mineral interrogation via ^{31}P MRI [27, 42, 44, 84]. Similar artifacts were observed during our ZTE experiments (not shown here). Although neither gradient delay nor eddy current-induced gradient waveform distortion matter in ZTE, potential problems might be due to timing errors in other hardware components such as the frequency demodulation unit [103].

5.6 Conclusion

In conclusion, the present study shows that gradient delay and eddy current-induced gradient waveform distortion compromise not only UTE image quality but, more importantly, bone water quantification. Correcting for these gradient system imperfections effectively alleviates image artifacts and substantially improves *in vivo* bone water quantification inter-scanner concordance.

CHAPTER 6: OSTEOPOROSIS TREATMENT STUDY

6.1 Abstract

Purpose: To test the ability of the previously described bone water and phosphorus MRI protocol to 1) differentiate osteoporotic patients from control subjects, and 2) reflect treatment outcomes in the patient cohort.

Methods: Thirty post-menopausal women with osteoporosis and 30 age-, race- and BMI-matched healthy control subjects were planned to be recruited in an ongoing treatment study. All subjects will undergo the bone water and phosphorus MRI protocol described in **Chapter 3** at baseline, 12 months and 24 months. Patients are given an intravenous zoledronic acid (zoledronate) infusion after the first and second imaging session. The surrogate markers for bone matrix density, porosity, and bone mineral density are derived from the acquired images and compared between the two groups.

Results: Baseline data on nine subjects (seven controls, two patients) have been collected prior to submission of this writing. While the density of the surrogate marker for bone matrix, bound water, was found to be lower in the osteoporotic group, the density of the surrogate marker for porosity, pore water, was higher as predicted. The osteoporotic cohort also had a lower average phosphorus density as compared to the control group, suggesting a reduction in bone mineral content resulting from the disease. No obvious differences were observed in DMB between the two groups.

Conclusion: Overall, baseline data obtained thus far suggest that this MRI protocol may be able to differentiate osteoporotic subjects from normal controls.

6.2 Introduction

Patients with osteoporosis are often treated with bisphosphonates [1, 2], a group of medications that reduce bone resorption by inhibiting osteoclast cell activity [3]. Following anti-resorptive treatment, the density of bone matrix increases while the level of porosity decreases. Further, the decrease in turnover rate allows newly formed bone tissue additional time to undergo mineralization, thereby elevating bone mineral density. The purpose of the research summarized in this chapter is to investigate whether the bone water and phosphorus MRI protocol described in **Chapter 3** can: 1) differentiate osteoporotic subjects from healthy controls; 2) track the treatment response in osteoporotic subjects. The ability to non-invasively detect changes in cortical porosity, and possibly DMB (both metrics have previously been shown to be altered in iliac bone biopsies [4, 5]), may allow for improved monitoring of treatment effects and provide further insight into the mechanism by which bisphosphonates decrease fracture risk. Toward this end, a group of osteoporotic patients and healthy controls are being recruited to participate in a 24-month clinical study.

6.3 Materials and Methods

The study design is illustrated in **Figure 6.1**. A cohort of 60 post-menopausal women, 30 osteoporotic patients and 30 healthy controls, are being recruited. The primary source of patients is Penn Medicine's Bone Center. Osteoporotic women are also recruited from primary care, obstetrics and gynecology, and endocrinology clinics at Penn Medicine, all of which routinely screen and treat patients with osteoporosis. Control subjects are recruited through localized postings of rack cards and flyers and email

blasts to the University of Pennsylvania and Penn Medicine community, methods that have previously proven effective. The patient group includes post-menopausal women, ages 50–75 years with a BMD T-score ≤ -2.5 at either the spine, total hip or femoral neck, as determined by DXA, who have not had a menstrual period for at least two years. The control group includes women without osteoporosis who are age-, race- and BMI-matched to subjects in the osteoporotic group. Exclusion criteria are: (a) current or prior use of medications known to affect bone (bisphosphonates, calcitonin, denosumab, teriparatide, estrogen, estrogen agonists/antagonists, thiazolidinediones, glucocorticoids, phenobarbital, phenytoin); (b) diseases known to affect bone (hyperparathyroidism, hyperthyroidism, diabetes, inflammatory bowel disease, liver or kidney disease), severe cardiac disease, current alcohol or drug abuse, 25-OH vitamin D level less than 20 ng/ml; (c) contraindications to bisphosphonates; (d) contraindications for MRI. All subjects undergo the bone water and phosphorus protocol described in **Section 3.3.2** at baseline, 12 months and 24 months. One intravenous infusion of zoledronic acid (a type of bisphosphonate medicine, also know as zoledronate [6]) is administered to the osteoporotic group immediately after the first and second MRI exam, while no medical intervention is performed in the control group. MRI-based surrogate markers are derived and their values compared between the two groups at each time point, and longitudinally within each group via ANOVA.

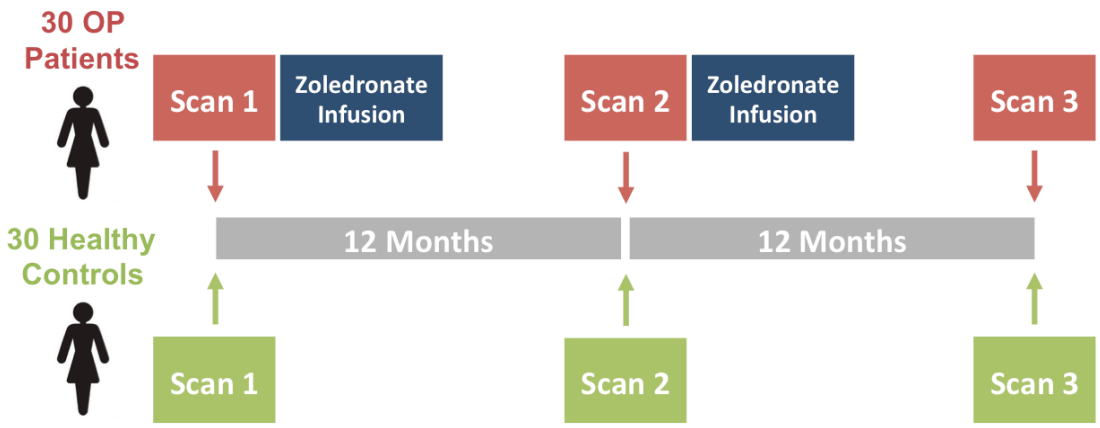

Figure 6.1 Illustration of the clinical study design. A total of 60 post-menopausal women are being recruited, 30 osteoporotic patients and 30 healthy controls. The osteoporotic group receives a two-year zoledronate treatment (one annual intravenous infusion) while the control group does not get any intervention. Both cohorts undergo the bone water and phosphorus MRI protocol described in previous chapters at three time points: baseline, 12 months and 24 months.

6.4 Baseline Results Obtained So Far

Baseline data for nine subjects (two osteoporotic patients, seven control subjects) have been collected at the time of this writing. Representative total water, bound water, and phosphorus images are shown in **Figure 6.2**. **Figure 6.3** compares surrogate marker color maps of a healthy control with those of a patient. The DXA-reported BMD, T-score and MR image-derived surrogate markers of all nine subjects are summarized in **Table 6.1**. DMB is represented as the ratio between [^{31}P] and [BW], with [^{31}P] being a volumetric quantity as described in **Chapter 3** (including the phosphorus signal within the entire bone region).

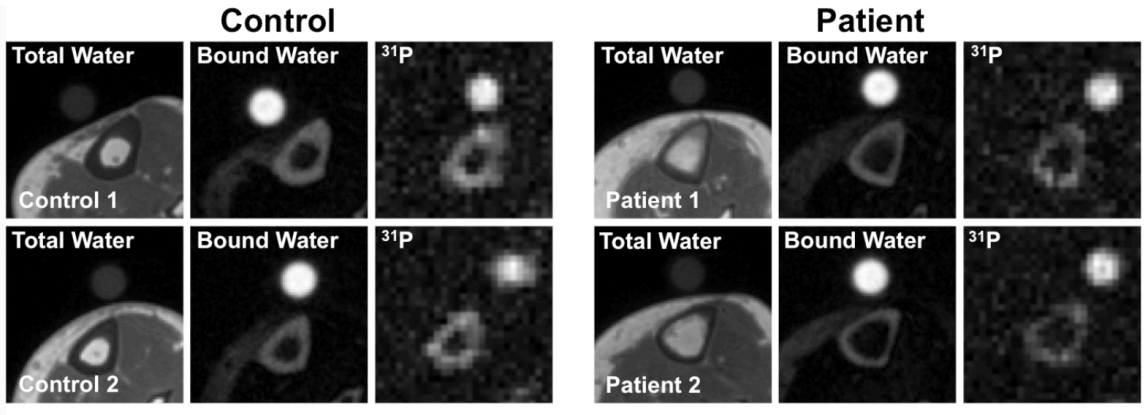

Figure 6.2 Bone water and phosphorus images of two healthy control subjects and two osteoporotic patients. Compared with healthy controls, osteoporotic subjects have thinner cortical bone, higher total water signal and lower phosphorus signal.

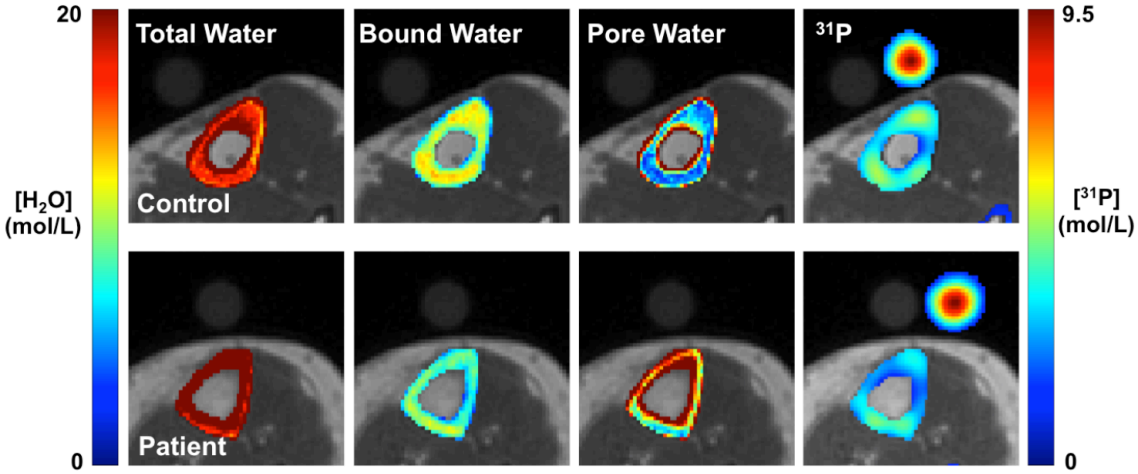

Figure 6.3 Color maps of surrogate markers for a healthy control and an osteoporotic patient.

Table 6.1 DXA-reported BMD, T-score and MRI-derived surrogate marker densities of healthy and osteoporotic subjects recruited to date.

Controls											
	T-Score			BMD (g/cm^2)			Bone Water (mol/L)			^{31}P (mol/L)	$^{31}P/BW$
Age	Femoral Neck	Total Hip	Total Lumbar	Femoral Neck	Total Hip	Total Lumbar	TW	BW	PW		
55	-0.2	-0.3	0.1	0.831	0.905	1.055	20.6	10.6	10.0	5.2	0.49
58	-2.0	-1.0	-0.9	0.623	0.824	0.951	21.4	9.2	12.2	5.5	0.60
61	-1.7	-1.0	-1.1	0.665	0.824	0.921	22.5	10.3	12.4	5.5	0.53
62	0.1	0.5	0.2	0.864	0.997	1.065	19.6	11.2	8.2	6.6	0.59
65	-0.7	-0.7	1.2	0.774	0.861	1.175	18.6	10.1	8.3	5.9	0.58
67	-1.2	-0.6	-1.3	0.713	0.872	0.908	17.4	9.8	7.3	5.6	0.57
68	-1.5	-0.3	-1.8	0.678	0.906	0.844	19.4	9.9	9.4	5.9	0.60
Mean	**-1.0**	**-0.5**	**-0.5**	**0.735**	**0.884**	**0.988**	**19.9**	**10.2**	**9.7**	**5.7**	**0.57**
Patients											
	T-Score			BMD (g/cm^2)			Bone Water (mol/L)			^{31}P (mol/L)	$^{31}P/BW$
Age	Femoral Neck	Total Hip	Total Lumbar	Femoral Neck	Total Hip	Total Lumbar	TW	BW	PW		
66	-2.4	-2.3	-2.6	0.586	0.666	0.761	26.3	8.9	17.4	4.7	0.53
69	-3.0	-2.1	-1.2	0.514	0.690	0.917	22.6	8.1	14.9	5.0	0.62
Mean	**-2.7**	**-2.2**	**-1.9**	**0.550**	**0.678**	**0.839**	**24.5**	**8.5**	**16.1**	**4.9**	**0.58**

6.5 Discussion

Several observations are expected throughout the course of this study. First, due to loss of bone tissue and its accompanying increase in porosity, bound water and phosphorus density measured from osteoporotic subjects should be lower, while pore water density should be higher than in control subjects at baseline. Second, women with osteoporosis should have a lower DMB than their non-osteoporotic counterparts due to a shorter period of secondary mineralization from the fast turnover rate [4, 7] at the baseline. Third, the aforementioned differences between the two groups are expected to reduce following administration of zoledronate.

As suggested by the data in **Figure 6.2**, patients are characterized with thinner cortical bone, a higher total water signal and a lower phosphorus signal. These observations are

confirmed in the color maps in **Figure 6.3**. Notably, bound water density is lower while pore water is higher in patients as compared to controls, suggesting that the elevated total water signal seen in the patients in **Figure 6.2** is mainly due to increased porosity. Quantification results in **Table 6.1** also indicate that osteoporotic patients present an increased average porosity level as compared to their healthy counterparts. The surrogate of bone mineral, phosphorus density, also appears lower in the osteoporotic subjects. The overall trend of the baseline data acquired to date is consistent with expectations. Although additional data are needed to establish the statistical significance of the baseline results and to evaluate the effectiveness of the proposed protocol in monitoring treatment response, the present preliminary work provides confidence in achieving these goals.

CHAPTER 7: CONCLUSIONS AND FUTURE WORK

7.1 Conclusions

The main results of this dissertation are summarized as follows:

7.1.1 Feasibility of MRI-Based Bone Matrix and Mineral Quantification *In Vivo*

In **Chapter 3**, the feasibility of quantifying bone water, the surrogate marker for bone matrix, and ^{31}P, the surrogate marker for bone mineral content, with solid-state MRI in a single session (within one hour) *in vivo* was investigated. The average concentrations for TW, BW and PW were 13.99 ± 1.26, 10.39 ± 0.80 and 3.34 ± 1.41 mol/L respectively, while the ^{31}P concentration was 5.29 ± 1.15 mol/L in a group of ten healthy subjects ranging in age from 29 to 65. These quantities were comparable to the *ex vivo* results published earlier with test-retest CV of 3.5%, 2.6 %, 6.5 % and 5.7 % for TW, BW, PW and ^{31}P respectively. The negative correlations between PW density and HR-pQCT derived BMD ($p < 0.05$), PI and ^{31}P ($p < 0.05$), and the positive correlations between TW and PW ($R = 0.81$, $p < 0.005$), between BMC estimated from ^{31}P MRI and HR-pQCT ($p < 0.0001$), further enhanced the credibility of this study. The findings in this chapter demonstrate the potential of MRI as a clinical tool to evaluate the bone health.

7.1.2 *In Vivo* Bone ^{31}P Relaxation Time Measurements and Their Implications in Mineral Quantification

In **Chapter 4**, a spectrum-based technique proposed to measure bone ^{31}P relaxation times *in vivo* was initially evaluated via simulation and then in an *ex vivo* experiment, and subsequently applied to ten healthy subjects. Although subject's age range spanned 50 years (26 to 76), the bone ^{31}P relaxation times were relatively tightly distributed: T_1 =

38.4 ± 1.5 s, T_2* = 178.3 ± 9.0 μs. Bone ^{31}P density was estimated to be 6.40 ± 0.58 mol/L for the same group of subjects using measured relaxation times. The average CV's were 1.5%, 2.6% and 4.4% for ^{31}P density, T_1 and T_2*, respectively. Based on these observations, individually measuring relaxation properties for healthy subjects may not be necessary.

7.1.3 The Importance of Gradient Error Correction on UTE-Based Bone Water Quantification

In **Chapter 5**, both simulation and phantom experiments demonstrated that gradient imperfections (time delay and eddy current-induced waveform distortion) lead to errors in k-space trajectory and spatially dependent object distortions in reconstructed UTE images. Quantitative analyses further revealed that gradient errors undermine not only the image-based quantification but also the measurement agreement between different scanners. The work in this chapter emphasizes the necessity of correcting gradient errors for quantitative studies involving UTE imaging.

7.2 Future Work

Based on the results presented in this dissertation, the following issues are worthy of further investigation:

7.2.1 Influence of Hardware Imperfections on ^{31}P ZTE-Based Bone Mineral Quantification

Chapter 5 demonstrated that imperfections in the encoding gradient substantially impacted both UTE image quality and image-based bone water quantification. Although not discussed here, similar artifacts were observed by the author in ZTE experiments.

Since encoding gradients are already fully ramped up prior to excitation in ZTE, k-space mis-mapping should not stem from gradient delay or waveform distortion as in UTE. Rather, mis-mapping is more likely due to the relative timing error between the RF pulse and data acquisition (ADC). It would be of interest to explore the effects of such hardware timing errors on ^{31}P ZTE-based bone mineral quantification.

7.2.2 The Ongoing Clinical Study

Only a small number of subjects had undergone a baseline MRI exam at the time of this writing (**Chapter 6**), which limited the statistical power of the data. Statistically significant differences between average bone water and phosphorus quantities at baseline should be observed between patients and healthy controls with the addition of more study subjects. Further, as zoledronate has been demonstrated to increase bone volume in ovariectomized animal models (simulating estrogen depletion-induced osteoporosis during post-menopause) [9, 10] and to increase BMD in osteoporotic patients [6, 11, 12], a treatment dependent reduction in surrogate marker differences between the two groups is expected at the second and third time points.

7.2.3 Imaging Protocol Acceleration with Interleaved ^{1}H/^{31}P Acquisition

The proposed *in vivo* bone water and phosphorus imaging protocol consists of one ^{1}H UTE sequence for imaging of total water (8.3 min), one ^{1}H IR-rUTE sequence for imaging of bound water (5.8 min) and one ^{31}P ZTE for imaging of bone phosphorus (22.5 min). For the spoiled steady-state gradient sequence (which the ^{31}P ZTE is analogous to), SNR time efficiency is relatively constant for a wide range of TRs as long as the corresponding Ernst angle is used. The particular TR and Ernst angle combination used in

our ^{31}P ZTE application results in less than 1% of the entire TR being spent on encoding and acquiring data while the remaining 99% is idle time. If this idle time within the ^{31}P sequence could be utilized for ^{1}H acquisition, the entire protocol could be accelerated by almost 50%. As illustrated in **Figure 7.1**, the entire ^{31}P ZTE can potentially be divided into two halves. The first half is interleaved with multiple TRs of ^{1}H dual-echo UTE (**Figure 7.1a**) while the second half is interleaved with one TR of ^{1}H IR-rUTE (**Figure 7.1b**). Since ^{1}H and ^{31}P sequences operate at very different frequencies (due to their distinct gyromagnetic ratio), they should not interfere with each other and therefore maintain their respective steady-state.

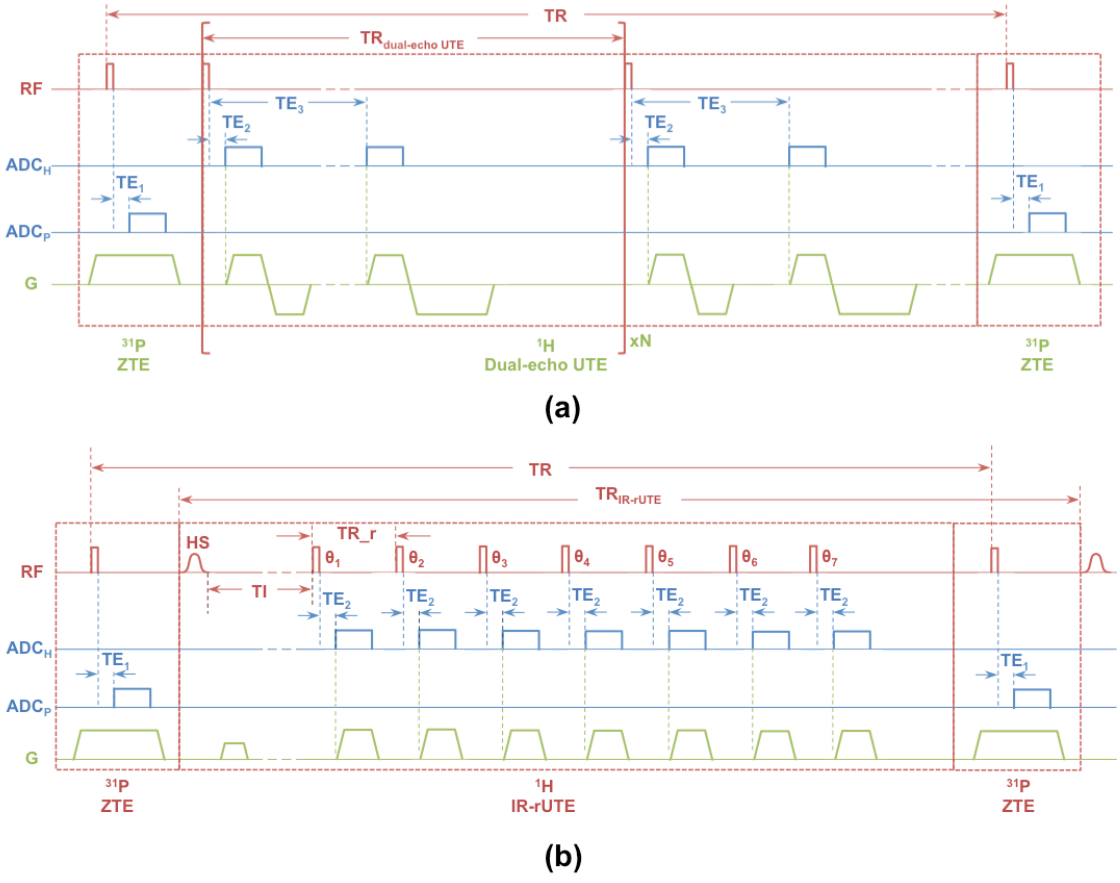

Figure 7.1 Schematic plot of interleaved ^{1}H/^{31}P sequence: a) ^{31}P ZTE interleaved with ^{1}H dual-

eco UTE; b) ^{31}P ZTE interleaved with ^{1}H IR-rUTE.

7.2.4 Potential to Differentiate Bone Diseases

Routinely used x-ray based bone examination techniques have certain limitations. For instance, DXA makes a diagnosis based on 2D projection and is consequently prone to bias from bone size and shape. Further, its reported BMD does not reflect a true mineralization level as the modality cannot distinguish between bone tissue and pore space. Nor are 3D clinical techniques, such as pQCT, able to provide true BMD due to their limited spatial resolution. Therefore, these exams cannot definitively differentiate bone diseases such as osteoporosis, characterized by a loss of bone volume with the remaining tissue properly mineralized, or osteomalacia, a condition distinguished by poor mineralization and intact total bone volume. With the ability to separately interrogate bone's organic and mineral phase, the proposed protocol may have the potential to distinguish these two conditions from each other. Because osteoporosis and osteomalacia have distinct underlying mechanisms and require different treatment plans, a non-invasive efficient method of differentiation would be of considerable clinical interest.

BIBLIOGRAPHY

1. Clarke B. Normal bone anatomy and physiology. Clin J Am Soc Nephrol. 2008;3 Suppl 3:S131-9. doi: 10.2215/CJN.04151206. PubMed PMID: 18988698; PubMed Central PMCID: PMCPMC3152283.
2. Rubin CT, Lanyon LE. Kappa Delta Award paper. Osteoregulatory nature of mechanical stimuli: function as a determinant for adaptive remodeling in bone. J Orthop Res. 1987;5(2):300-10. doi: 10.1002/jor.1100050217. PubMed PMID: 3572599.
3. https://www.majordifferences.com/2013/02/difference-between-bone-and-cartilage.html#.XS0o3pNKhDM
4. https://depts.washington.edu/bonebio/ASBMRed/structure.html.
5. Granke M, Does MD, Nyman JS. The Role of Water Compartments in the Material Properties of Cortical Bone. Calcif Tissue Int. 2015;97(3):292-307. doi: 10.1007/s00223-015-9977-5. PubMed PMID: 25783011; PubMed Central PMCID: PMCPMC4526331.
6. Burr DB, Allen MR. Basic and applied bone biology. Amsterdam: Elsevier/Academic Press; 2013.
7. Bonjour JP. Calcium and phosphate: a duet of ions playing for bone health. J Am Coll Nutr. 2011;30(5 Suppl 1):438S-48S. PubMed PMID: 22081690.
8. Boivin G, Farlay D, Bala Y, Doublier A, Meunier PJ, Delmas PD. Influence of remodeling on the mineralization of bone tissue. Osteoporos Int. 2009;20(6):1023-6. doi: 10.1007/s00198-009-0861-x. PubMed PMID: 19340504; PubMed Central PMCID: PMCPMC2904474.
9. McCalden RW, McGeough JA, Barker MB, Court-Brown CM. Age-related changes in the tensile properties of cortical bone. The relative importance of changes in porosity, mineralization, and microstructure. J Bone Joint Surg Am. 1993;75(8):1193-205. PubMed PMID: 8354678.
10. https://naturalhistory.si.edu/education/teaching-resources/written-bone/skeleton-keys/how-bone-biographies-get-written.
11. Manolagas SC. Birth and death of bone cells: basic regulatory mechanisms and implications for the pathogenesis and treatment of osteoporosis. Endocr Rev. 2000;21(2):115-37. doi: 10.1210/edrv.21.2.0395. PubMed PMID: 10782361.
12. Wright NC, Looker AC, Saag KG, Curtis JR, Delzell ES, Randall S, et al. The recent prevalence of osteoporosis and low bone mass in the United States based on bone mineral density at the femoral neck or lumbar spine. J Bone Miner Res. 2014;29(11):2520-6. doi: 10.1002/jbmr.2269. PubMed PMID: 24771492.
13. Day J. Population Projections of the United States by Age, Sex, Race, and Hispanic Origin: 1995 to 2050. Washington, DC: U.S. Government Printing Office, 1996.
14. Weiss NS, Liff JM, Ure CL, Ballard JH, Abbott GH, Daling JR. Mortality in women following hip fracture. J Chronic Dis. 1983;36(12):879-82. PubMed PMID: 6655032.
15. Fisher ES, Baron JA, Malenka DJ, Barrett JA, Kniffin WD, Whaley FS, et al. Hip fracture incidence and mortality in New England. Epidemiology. 1991;2(2):116-22. PubMed PMID: 1932308.
16. Cooper C, Atkinson EJ, Jacobsen SJ, O'Fallon WM, Melton LJ, 3rd. Population- based study of survival after osteoporotic fractures. Am J Epidemiol. 1993;137(9):1001-5. PubMed PMID: 8317445.
17. Cauley JA, Thompson DE, Ensrud KC, Scott JC, Black D. Risk of mortality following clinical fractures. Osteoporos Int. 2000;11(7):556-61.
18. Cooper C, Campion G, Melton LJd. Hip fractures in the elderly: a world-wide projection. Osteoporosis International. 1992;2(6):285-9.

19. Reginster JY, Burlet N. Osteoporosis: a still increasing prevalence. Bone. 2006;38(2 Suppl 1):S4-9. doi: 10.1016/j.bone.2005.11.024. PubMed PMID: 16455317.
20. Watts NB, Bilezikian JP, Camacho PM, Greenspan SL, Harris ST, Hodgson SF, et al. American Association of Clinical Endocrinologists Medical Guidelines for Clinical Practice for the diagnosis and treatment of postmenopausal osteoporosis: executive summary of recommendations. Endocr Pract. 16(6):1016-9. Epub 2011/01/11. doi: H77351T7813V7248 [pii]. PubMed PMID: 21216723.
21. Burge R, Dawson-Hughes B, Solomon DH, Wong JB, King A, Tosteson A. Incidence and Economic Burden of Osteoporosis-Related Fractures in the United States, 2005–2025. Journal of Bone and Mineral Research. 2007;22(3):465-75. doi: 10.1359/jbmr.061113.
22. Kanis JA, Melton LJ, 3rd, Christiansen C, Johnston CC, Khaltaev N. The diagnosis of osteoporosis. J Bone Miner Res. 1994;9(8):1137-41. Epub 1994/08/01. doi: 10.1002/jbmr.5650090802. PubMed PMID: 7976495.
23. Siris ES, Brenneman SK, Barrett-Connor E, Miller PD, Sajjan S, Berger ML, et al. The effect of age and bone mineral density on the absolute, excess, and relative risk of fracture in postmenopausal women aged 50-99: results from the National Osteoporosis Risk Assessment (NORA). Osteoporos Int. 2006;17(4):565-74. PubMed PMID: 16392027.
24. Prevrhal S, Engelke K, Genant HK. Radiology of Osteoporosis: Springer, Berlin, Heidelberg; 2008.
25. Li C, Seifert AC, Rad HS, Bhagat YA, Rajapakse CS, Sun W, et al. Cortical bone water concentration: dependence of MR imaging measures on age and pore volume fraction. Radiology. 2014;272(3):796-806. doi: 10.1148/radiol.14132585. PubMed PMID: 24814179.
26. Rajapakse CS, Bashoor-Zadeh M, Li C, Sun W, Wright AC, Wehrli FW. Volumetric Cortical Bone Porosity Assessment with MR Imaging: Validation and Clinical Feasibility. Radiology. 2015;276(2):526-35. doi: 10.1148/radiol.15141850. PubMed PMID: 26203710; PubMed Central PMCID: PMC4517853.
27. Seifert AC, Li C, Rajapakse CS, Bashoor-Zadeh M, Bhagat YA, Wright AC, et al. Bone mineral 31P and matrix-bound water densities measured by solid-state 31P and 1H MRI. NMR in Biomedicine. 2014;27(7):739-48. doi: 10.1002/nbm.3107.
28. Seifert AC, Li C, Wehrli SL, Wehrli FW. A Surrogate Measure of Cortical Bone Matrix Density by Long T2 -Suppressed MRI. J Bone Miner Res. 2015;30(12):2229-38. doi: 10.1002/jbmr.2580. PubMed PMID: 26085307; PubMed Central PMCID: PMC4683123.
29. Manhard MK, Horch RA, Gochberg DF, Nyman JS, Does MD. In Vivo Quantitative MR Imaging of Bound and Pore Water in Cortical Bone. Radiology. 2015;277(1):221-9. doi: 10.1148/radiol.2015140336.
30. Chen J, Carl M, Ma Y, Shao H, Lu X, Chen B, et al. Fast volumetric imaging of bound and pore water in cortical bone using three-dimensional ultrashort-TE (UTE) and inversion recovery UTE sequences. NMR Biomed. 2016;29(10):1373-80. doi: 10.1002/nbm.3579. PubMed PMID: 27496335; PubMed Central PMCID: PMCPMC5035210.
31. Anumula S, Magland J, Wehrli SL, Zhang H, Ong H, Song HK, et al. Measurement of phosphorus content in normal and osteomalacic rabbit bone by solid-state 3D radial imaging. Magn Reson Med. 2006;56(5):946-52. Epub 2006/10/17. doi: 10.1002/mrm.21050. PubMed PMID: 17041893.
32. Anumula S, Magland J, Wehrli SL, Ong H, Song HK, Wehrli FW. Multi-modality study of the compositional and mechanical implications of hypomineralization in a rabbit model of osteomalacia. Bone. 2008;42(2):405-13. Epub 2007/12/07. doi: S8756-3282(07)00786-7 [pii] 10.1016/j.bone.2007.10.011. PubMed PMID: 18053788; PubMed Central PMCID: PMC2259120.
33. Anumula S, Wehrli SL, Magland J, Wright AC, Wehrli FW. Ultra-short echo- time MRI detects changes in bone mineralization and water content in OVX rat bone in response to

alendronate treatment. Bone. 2010;46(5):1391-9. Epub 2010/01/26. doi: S8756-3282(10)00378-9 [pii] 10.1016/j.bone.2010.01.372. PubMed PMID: 20096815; PubMed Central PMCID: PMC2854263.
34. Bernstein MA, King KF, Zhou ZJ. Handbook of MRI pulse sequences. Amsterdam; Boston: Academic Press; 2004.
35. Bloch F. Nuclear Induction. Physical Review. 1946;70:460-74.
36. Chavhan GB, Babyn PS, Thomas B, Shroff MM, Haacke EM. Principles, techniques, and applications of T2*-based MR imaging and its special applications. Radiographics. 2009;29(5):1433-49. doi: 10.1148/rg.295095034. PubMed PMID: 19755604; PubMed Central PMCID: PMCPMC2799958.
37. Ridgway JP. Cardiovascular magnetic resonance physics for clinicians: part I. J Cardiovasc Magn Reson. 2010;12:71. doi: 10.1186/1532-429X-12-71. PubMed PMID: 21118531; PubMed Central PMCID: PMCPMC3016368.
38. Stanisz GJ, Odrobina EE, Pun J, Escaravage M, Graham SJ, Bronskill MJ, et al. T1, T2 relaxation and magnetization transfer in tissue at 3T. Magn Reson Med. 2005;54(3):507-12. doi: 10.1002/mrm.20605. PubMed PMID: 16086319.
39. Horch RA, Gochberg DF, Nyman JS, Does MD. Non-invasive predictors of human cortical bone mechanical properties: T(2)-discriminated H NMR compared with high resolution X-ray. PLoS One. 2011;6(1):e16359. doi: 10.1371/journal.pone.0016359. PubMed PMID: 21283693; PubMed Central PMCID: PMCPMC3025007.
40. Horch RA, Gochberg DF, Nyman JS, Does MD. Clinically compatible MRI strategies for discriminating bound and pore water in cortical bone. Magn Reson Med. 2012. Epub 2012/02/02. doi: 10.1002/mrm.24186. PubMed PMID: 22294340.
41. Seifert AC, Wright AC, Wehrli SL, Ong HH, Li C, Wehrli FW. 31P NMR Relaxation of Cortical Bone Mineral at Multiple Magnetic Field Strengths and Levels of Demineralization. NMR in Biomedicine. 2013;26(9):1158-66. Epub 2013 Mar 18.
42. Wu Y, Reese TG, Cao H, Hrovat MI, Toddes SP, Lemdiasov RA, et al. Bone mineral imaged in vivo by (31) P solid state MRI of human wrists. J Magn Reson Imaging. 2011;34(3):623-33. Epub 2011/07/16. doi: 10.1002/jmri.22637. PubMed PMID: 21761459; PubMed Central PMCID: PMC3197865.
43. Wu Y, Ackerman JL, Chesler DA, Li J, Neer RM, Wang J, et al. Evaluation of bone mineral density using three-dimensional solid state phosphorus-31 NMR projection imaging. Calcif Tissue Int. 1998;62(6):512-8. PubMed PMID: 9576979.
44. Robson MD, Gatehouse PD, Bydder GM, Neubauer S. Human imaging of phosphorus in cortical and trabecular bone in vivo. Magn Reson Med. 2004;51(5):888-92. PubMed PMID: 15122669.
45. Robson MD, Gatehouse PD, Bydder M, Bydder GM. Magnetic resonance: an introduction to ultrashort TE (UTE) imaging. J Comput Assist Tomogr. 2003;27(6):825-46. PubMed PMID: 14600447.
46. Li C, Magland JF, Rad HS, Song HK, Wehrli FW. Comparison of optimized soft- tissue suppression schemes for ultrashort echo time MRI. Magn Reson Med. 2011;68(3):680-9. Epub 2011/12/14. doi: 10.1002/mrm.23267. PubMed PMID: 22161636.
47. Wu Y, Dai G, Ackerman JL, Hrovat MI, Glimcher MJ, Snyder BD, et al. Water- and fat-suppressed proton projection MRI (WASPI) of rat femur bone. Magn Reson Med. 2007;57(3):554-67. PubMed PMID: 17326184.
48. Wu Y, Ackerman JL, Chesler DA, Graham L, Wang Y, Glimcher MJ. Density of organic matrix of native mineralized bone measured by water- and fat-suppressed proton projection MRI. Magn Reson Med. 2003;50(1):59-68. PubMed PMID: 12815679.
49. Grodzki DM, Jakob PM, Heismann B. Ultrashort echo time imaging using pointwise encoding time reduction with radial acquisition (PETRA). Magn Reson Med. 2012;67(2):510-8. Epub 2011/07/02. doi: 10.1002/mrm.23017. PubMed PMID: 21721039.

50. Li C, Magland JF, Seifert AC, Wehrli FW. Correction of excitation profile in Zero Echo Time (ZTE) imaging using quadratic phase-modulated RF pulse excitation and iterative reconstruction. IEEE Trans Med Imaging. 2014;33(4):961-9. doi: 10.1109/TMI.2014.2300500. PubMed PMID: 24710164; PubMed Central PMCID: PMCPMC4136480.
51. Pipe JG, Menon P. Sampling density compensation in MRI: rationale and an iterative numerical solution. Magn Reson Med. 1999;41(1):179-86. PubMed PMID: 10025627.
52. Gatehouse PD, Bydder GM. Magnetic resonance imaging of short T2 components in tissue. Clin Radiol. 2003;58(1):1-19. PubMed PMID: 12565203.
53. Biswas R, Bae W, Diaz E, Masuda K, Chung CB, Bydder GM, et al. Ultrashort echo time (UTE) imaging with bi-component analysis: bound and free water evaluation of bovine cortical bone subject to sequential drying. Bone. 2012;50(3):749-55. Epub 2011/12/20. doi: 10.1016/j.bone.2011.11.029. PubMed PMID: 22178540; PubMed Central PMCID: PMC3463503.
54. Seifert AC, Wehrli SL, Wehrli FW. Bi-component T2 * analysis of bound and pore bone water fractions fails at high field strengths. NMR Biomed. 2015;28(7):861-72. doi: 10.1002/nbm.3305. PubMed PMID: 25981785; PubMed Central PMCID: PMCPMC4478152.
55. Tannus A, Garwood M. Adiabatic pulses. NMR Biomed. 1997;10(8):423-34. PubMed PMID: 9542739.
56. Gomberg BG, Saha PK, Song HK, Hwang SN, Wehrli FW. Application of topological analysis to magnetic resonance images of human trabecular bone. IEEE Transactions on Medical Imaging. 2000;19:166-74.
57. Carballido-Gamio J, Krug R, Huber MB, Hyun B, Eckstein F, Majumdar S, et al. Geodesic topological analysis of trabecular bone microarchitecture from high-spatial resolution magnetic resonance images. Magn Reson Med. 2009;61(2):448-56. Epub 2009/01/24. doi: 10.1002/mrm.21835. PubMed PMID: 19161163.
58. Saha P, Xu Y, Duan H, Heiner A, Liang G. Volumetric Topological Analysis: A Novel Approach for Trabecular Bone Classification on the Continuum between Plates and Rods. IEEE Trans Med Imaging. 2010. Epub 2010/06/22. doi: 10.1109/TMI.2010.2050779. PubMed PMID: 20562041.
59. Wald MJ, Magland JF, Rajapakse CS, Bhagat YA, Wehrli FW. Predicting trabecular bone elastic properties from measures of bone volume fraction and fabric on the basis of micromagnetic resonance images. Magn Reson Med. 2012;68(2):463-73. Epub 2011/12/14. doi: 10.1002/mrm.23253. PubMed PMID: 22162036; PubMed Central PMCID: PMC3374911.
60. Benito M, Vasilic B, Wehrli FW, Bunker B, Wald M, Gomberg B, et al. Effect of testosterone replacement on bone architecture in hypogonadal men. J Bone Miner Res. 2005;20(10):1785-91.
61. Wehrli FW, Ladinsky GA, Jones C, Benito M, Magland J, Vasilic B, et al. In vivo magnetic resonance detects rapid remodeling changes in the topology of the trabecular bone network after menopause and the protective effect of estradiol. J Bone Miner Res. 2008;23(5):730-40. PubMed PMID: 18251704.
62. Folkesson J, Goldenstein J, Carballido-Gamio J, Kazakia G, Burghardt AJ, Rodriguez A, et al. Longitudinal evaluation of the effects of alendronate on MRI bone microarchitecture in postmenopausal osteopenic women. Bone. 2011;48(3):611-21. Epub 2010/11/10. doi: S8756-3282(10)01999-X [pii] 10.1016/j.bone.2010.10.179. PubMed PMID: 21059422.
63. Hansen S, Hauge EM, Jensen JE, Brixen K. Differing effects of PTH 1-34, PTH 1-84 and zoledronic acid on bone microarchitecture and estimated strength in postmenopausal women with osteoporosis. An 18 month open-labeled observational study using HR-pQCT.

J Bone Miner Res. 2012. Epub 2012/10/10. doi: 10.1002/jbmr.1784. PubMed PMID: 23044908.
64. Rajapakse CS, Leonard MB, Bhagat YA, Sun W, Magland JF, Wehrli FW. Micro-MR imaging-based computational biomechanics demonstrates reduction in cortical and trabecular bone strength after renal transplantation. Radiology. 2012;262(3):912-20. Epub 2012/02/24. doi: 10.1148/radiol.11111044. PubMed PMID: 22357891; PubMed Central PMCID: PMC3285225.
65. Zarowitz BJ, Cheng LI, Allen C, O'Shea T, Stolshek B. Osteoporosis prevalence and characteristics of treated and untreated nursing home residents with osteoporosis. J Am Med Dir Assoc. 2015;16(4):341-8. doi: 10.1016/j.jamda.2015.01.073. PubMed PMID: 25726417.
66. Seeman E, Delmas PD. Bone quality--the material and structural basis of bone strength and fragility. N Engl J Med. 2006;354(21):2250-61. PubMed PMID: 16723616.
67. Grynpas M. Age and disease-related changes in the mineral of bone. Calcif Tissue Int. 1993;53(Suppl 1):S57-64.
68. Kanis JA, Johnell O, Oden A, Johansson H, McCloskey E. FRAX and the assessment of fracture probability in men and women from the UK. Osteoporos Int. 2008;19(4):385-97. Epub 2008/02/23. doi: 10.1007/s00198-007-0543-5. PubMed PMID: 18292978; PubMed Central PMCID: PMC2267485.
69. Seeman E. Age- and menopause-related bone loss compromise cortical and trabecular microstructure. J Gerontol A Biol Sci Med Sci. 2013;68(10):1218-25. Epub 2013/07/09. doi: 10.1093/gerona/glt071. PubMed PMID: 23833200.
70. Horch RA, Nyman JS, Gochberg DF, Dortch RD, Does MD. Characterization of 1H NMR signal in human cortical bone for magnetic resonance imaging. Magn Reson Med. 2010;64(3):680-7. Epub 2010/09/02. doi: 10.1002/mrm.22459. PubMed PMID: 20806375; PubMed Central PMCID: PMC2933073.
71. Fernandez-Seara MA, Wehrli SL, Takahashi M, Wehrli FW. Water content measured by proton-deuteron exchange NMR predicts bone mineral density and mechanical properties. J Bone Miner Res. 2004;19(2):289-96. doi: 10.1359/JBMR.0301227. PubMed PMID: 14969399.
72. Nyman JS, Ni Q, Nicolella DP, Wang X. Measurements of mobile and bound water by nuclear magnetic resonance correlate with mechanical properties of bone. Bone. 2008;42(1):193-9. PubMed PMID: 17964874.
73. Techawiboonwong A, Song HK, Leonard MB, Wehrli FW. Cortical bone water: in vivo quantification with ultrashort echo-time MR imaging. Radiology. 2008;248(3):824-33. PubMed PMID: 18632530.
74. Li C, Magland JF, Zhao X, Seifert AC, Wehrli FW. Selective in vivo bone imaging with long-T2 suppressed PETRA MRI. Magn Reson Med. 2016. doi: 10.1002/mrm.26178. PubMed PMID: 26914767.
75. Rad HS, Lam SC, Magland JF, Ong H, Li C, Song HK, et al. Quantifying cortical bone water in vivo by three-dimensional ultra-short echo-time MRI. NMR in Biomedicine. 2011;24(7):855-64. Epub 2011/01/29. doi: 10.1002/nbm.1631. PubMed PMID: 21274960.
76. Wehrli FW, Fernandez-Seara MA. Nuclear magnetic resonance studies of bone water. Ann Biomed Eng. 2005;33(1):79-86. PubMed PMID: 15709708.
77. Laval-Jeantet AM, Bergot C, Carroll R, Garcia-Schaefer F. Cortical bone senescence and mineral bone density of the humerus. Calcified Tissue Int. 1983;35:268-72.
78. Bousson V, Bergot C, Meunier A, Barbot F, Parlier-Cuau C, Laval-Jeantet AM, et al. CT of the middiaphyseal femur: cortical bone mineral density and relation to porosity. Radiology. 2000;217(1):179-87. PubMed PMID: 11012442.
79. Patsch JM, Burghardt AJ, Yap SP, Baum T, Schwartz AV, Joseph GB, et al. Increased cortical porosity in type 2 diabetic postmenopausal women with fragility fractures. J Bone

Miner Res. 2013;28(2):313-24. Epub 2012/09/20. doi: 10.1002/jbmr.1763. PubMed PMID: 22991256; PubMed Central PMCID: PMC3534818.
80. Roschger P, Rinnerthaler S, Yates J, Rodan GA, Fratzl P, Klaushofer K. Alendronate increases degree and uniformity of mineralization in cancellous bone and decreases the porosity in cortical bone of osteoporotic women. Bone. 2001;29(2):185-91. PubMed PMID: 11502482.
81. Wehrli F, Hilaire L, Fernández-Seara M, Gomberg B, Song H, Zemel B, et al. Quantitative magnetic resonance imaging in the calcaneus and femur of women with varying degrees of osteopenia and vertebral deformity status. J Bone Min Res. 2002;17:2265-73.
82. Chen J, Carl M, Shao H, Chang E, Bydder G, Du J, editors. Fast volumetric mapping of bound and pore water content in cortical bone in vivo using 3D Cones sequences. Proc ISMRM 24th Scientific Meeting; 2016; Singapore: ISMRM.
83. Pauly JM, Conolly S, Nishimura D, Macovski A, editors. A Slice-selective excitation for very short T2 species. SMRM 8th Annual Meeting; 1989; Amsterdam, The Netherlands.
84. Zhao X, Song HK, Seifert AC, Li C, Wehrli FW. Feasibility of assessing bone matrix and mineral properties in vivo by combined solid-state 1H and 31P MRI. PLoS One. 2017;12(3):e0173995. doi: 10.1371/journal.pone.0173995. PubMed PMID: 28296979; PubMed Central PMCID: PMCPMC5352014.
85. Follet H, Boivin G, Rumelhart C, Meunier PJ. The degree of mineralization is a determinant of bone strength: a study on human calcanei. Bone. 2004;34(5):783-9. doi: 10.1016/j.bone.2003.12.012. PubMed PMID: 15121009.
86. Riggs BL, Jr., Bassingthwaighte JB, Jowsey J, Pequegnat EP. Autoradiographic method for quantitation of deposition and distribution of radiocalcium in bone. J Lab Clin Med. 1970;75(3):520-8. PubMed PMID: 5416906; PubMed Central PMCID: PMCPMC2942796.
87. Nuzzo S, Lafage-Proust MH, Martin-Badosa E, Boivin G, Thomas T, Alexandre C, et al. Synchrotron radiation microtomography allows the analysis of three-dimensional microarchitecture and degree of mineralization of human iliac crest biopsy specimens: effects of etidronate treatment. J Bone Miner Res. 2002;17(8):1372-82. PubMed PMID: 12162491.
88. Cao H, Ackerman JL, Hrovat MI, Graham L, Glimcher MJ, Wu Y. Quantitative bone matrix density measurement by water- and fat-suppressed proton projection MRI (WASPI) with polymer calibration phantoms. Magn Reson Med. 2008;60(6):1433-43. PubMed PMID: 19025909.
89. Wu Y, Glimcher MJ, Rey C, Ackerman JL. A unique protonated phosphate group in bone mineral not present in synthetic calcium phosphates. Identification by phosphorus-31 solid state NMR spectroscopy. J Mol Biol. 1994;244:423-35.
90. Wu Y, Ackerman JL, Strawich ES, Rey C, Kim HM, Glimcher MJ. Phosphate ions in bone: identification of a calcium-organic phosphate complex by 31P solid-state NMR spectroscopy at early stages of mineralization. Calcif Tissue Int. 2003;72(5):610-26. Epub 2003/05/02. doi: 10.1007/s00223-002-1068-8. PubMed PMID: 12724829.
91. Kemp GJ, Meyerspeer M, Moser E. Absolute quantification of phosphorus metabolite concentrations in human muscle in vivo by 31P MRS: a quantitative review. NMR Biomed. 2007;20(6):555-65. doi: 10.1002/nbm.1192. PubMed PMID: 17628042.
92. Meyerspeer M, Krssak M, Moser E. Relaxation times of 31P-metabolites in human calf muscle at 3 T. Magn Reson Med. 2003;49(4):620-5. doi: 10.1002/mrm.10426. PubMed PMID: 12652531.
93. Sacolick LI, Wiesinger F, Hancu I, Vogel MW. B1 mapping by Bloch-Siegert shift. Magn Reson Med. 2010;63(5):1315-22. doi: 10.1002/mrm.22357. PubMed PMID: 20432302; PubMed Central PMCID: PMCPMC2933656.
94. Yushkevich PA, Piven J, Hazlett HC, Smith RG, Ho S, Gee JC, et al. User-guided 3D active contour segmentation of anatomical structures: significantly improved efficiency and

reliability. Neuroimage. 2006;31(3):1116-28. doi: 10.1016/j.neuroimage.2006.01.015. PubMed PMID: 16545965.
95. Magland JF, Li C, Langham MC, Wehrli FW. Pulse sequence programming in a dynamic visual environment: SequenceTree. Magn Reson Med. 2016;75(1):257-65. doi: 10.1002/mrm.25640. PubMed PMID: 25754837; PubMed Central PMCID: PMCPMC4561593.
96. Hu BS, Conolly SM, Wright GA, Nishimura DG, Macovski A. Pulsed saturation transfer contrast. Magn Reson Med. 1992;26(2):231-40. PubMed PMID: 1325023.
97. Carl M, Bydder M, Du J, Takahashi A, Han E. Optimization of RF excitation to maximize signal and T2 contrast of tissues with rapid transverse relaxation. Magn Reson Med. 2010;64(2):481-90. Epub 2010/07/29. doi: 10.1002/mrm.22433. PubMed PMID: 20665792.
98. Schoenau E. From mechanostat theory to development of the "Functional Muscle-Bone-Unit". J Musculoskelet Neuronal Interact. 2005;5(3):232-8. PubMed PMID: 16172514.
99. Bogner W, Chmelik M, Schmid AI, Moser E, Trattnig S, Gruber S. Assessment of (31)P relaxation times in the human calf muscle: a comparison between 3 T and 7 T in vivo. Magn Reson Med. 2009;62(3):574-82. doi: 10.1002/mrm.22057. PubMed PMID: 19526487.
100. Duyn JH, Yang Y, Frank JA, van der Veen JW. Simple correction method for k-space trajectory deviations in MRI. J Magn Reson. 1998;132(1):150-3. doi: 10.1006/jmre.1998.1396. PubMed PMID: 9615415.
101. Alley MT, Glover GH, Pelc NJ. Gradient characterization using a Fourier-transform technique. Magn Reson Med. 1998;39(4):581-7. PubMed PMID: 9543420.
102. Peters DC, Derbyshire JA, McVeigh ER. Centering the projection reconstruction trajectory: reducing gradient delay errors. Magn Reson Med. 2003;50(1):1-6. PubMed PMID: 12815671.
103. Jung Y, Jashnani Y, Kijowski R, Block WF. Consistent non-cartesian off-axis MRI quality: calibrating and removing multiple sources of demodulation phase errors. Magn Reson Med. 2007;57(1):206-12. doi: 10.1002/mrm.21092. PubMed PMID: 17139618.
104. Tan H, Meyer CH. Estimation of k-space trajectories in spiral MRI. Magn Reson Med. 2009;61(6):1396-404. doi: 10.1002/mrm.21813. PubMed PMID: 19353671; PubMed Central PMCID: PMCPMC3256576.
105. Atkinson IC, Lu A, Thulborn KR. Characterization and correction of system delays and eddy currents for MR imaging with ultrashort echo-time and time-varying gradients. Magn Reson Med. 2009;62(2):532-7. doi: 10.1002/mrm.22016. PubMed PMID: 19353662.
106. Latta P, Starcuk Z, Jr., Gruwel ML, Weber MH, Tomanek B. K-space trajectory mapping and its application for ultrashort Echo time imaging. Magn Reson Imaging. 2017;36:68-76. doi: 10.1016/j.mri.2016.10.012. PubMed PMID: 27742433.
107. Takizawa M, Hanada H, Oka K, Takahashi T, Yamamoto E, Fujii M. A robust ultrashort TE (UTE) imaging method with corrected k-space trajectory by using parametric multiple function model of gradient waveform. IEEE Trans Med Imaging. 2013;32(2):306-16. doi: 10.1109/TMI.2012.2226050. PubMed PMID: 23144030.
108. Herrmann KH, Kramer M, Reichenbach JR. Time Efficient 3D Radial UTE Sampling with Fully Automatic Delay Compensation on a Clinical 3T MR Scanner. PLoS One. 2016;11(3):e0150371. doi: 10.1371/journal.pone.0150371. PubMed PMID: 26975051; PubMed Central PMCID: PMCPMC4790903.
109. Magland JF, Saligheh-Rad H, Wehrli FW, editors. Correcting for Gradient Imperfections in Ultra-Short Echo Time Imaging. 18th Annual ISMRM Scientific Meeting; 2010; Stockholm, Sweden: ISMRM.
110. Stich M, Pereira LM, Wech T, Weng AM, Ringler R, Bley TA, et al., editors. Trajectory correction for a 3D-Ultrashort Echo Time (UTE) sequence using the gradient system transfer function. 26th Annual ISMRM Scientific Meeting; 2018; Paris, France: ISMRM.

111. Kronthaler S, Rahmer J, Bornert P, Karampinos D, editors. Trajectory correction for ultrashort echo-time (UTE) imaging based on the measurement of the gradient impulse response function (GIRF) with a thin-slice method. 27th Annual ISMRM Scientific Meeting; 2019; Montreal, Canada: ISMRM.
112. Latta P, Starcuk Z, Jr., Gruwel MLH, Lattova B, Lattova P, Stourac P, et al. Influence of k-space trajectory corrections on proton density mapping with ultrashort echo time imaging: Application for imaging of short T2 components in white matter. Magn Reson Imaging. 2018;51:87-95. doi: 10.1016/j.mri.2018.04.020. PubMed PMID: 29729437.
113. Brodsky EK, Samsonov AA, Block WF. Characterizing and correcting gradient errors in non-cartesian imaging: Are gradient errors linear time-invariant (LTI)? Magn Reson Med. 2009;62(6):1466-76. doi: 10.1002/mrm.22100. PubMed PMID: 19877274; PubMed Central PMCID: PMCPMC2857383.
114. Zwart NR, Johnson KO, Pipe JG. Efficient sample density estimation by combining gridding and an optimized kernel. Magn Reson Med. 2012;67(3):701-10. doi: 10.1002/mrm.23041. PubMed PMID: 21688320.
115. Collins CM, Liu WZ, Schreiber W, Yang QX, Smith MB. Central brightening due to constructive interference with, without, and despite dielectric resonance. Journal of Magnetic Resonance Imaging. 2005;21(2):192-6. doi: 10.1002/jmri.20245. PubMed PMID: WOS:000226728300014.
116. Margosian PT, T; Takizawa, M Practical Implementation of UTE Imaging. Encyclopedia of Magnetic Resonance. 2012.
117. Brown DL, Robbins R. Developments in the therapeutic applications of bisphosphonates. J Clin Pharmacol. 1999;39(7):651-60. PubMed PMID: 10392318. 118. Marcus R, Wong M, Heath H, 3rd, Stock JL. Antiresorptive treatment of postmenopausal osteoporosis: comparison of study designs and outcomes in large clinical trials with fracture as an endpoint. Endocr Rev. 2002;23(1):16-37. PubMed PMID: 11844743.
118. Marcus R, Wong M, Heath H, 3rd, Stock JL. Antiresorptive treatment of postmenopausal osteoporosis: comparison of study designs and outcomes in large clinical trials with fracture as an endpoint. Endocr Rev. 2002;23(1):16-37. PubMed PMID: 11844743.
119. Fleisch H. Bisphosphonates: mechanisms of action. Endocr Rev. 1998;19(1):80-100. doi: 10.1210/edrv.19.1.0325. PubMed PMID: 9494781.
120. Boivin GY, Chavassieux PM, Santora AC, Yates J, Meunier PJ. Alendronate increases bone strength by increasing the mean degree of mineralization of bone tissue in osteoporotic women. Bone. 2000;27(5):687-94. PubMed PMID: 11062357. 121. Borah B, Dufresne T, Nurre J, Phipps R, Chmielewski P, Wagner L, et al. Risedronate Reduces Intracortical Porosity in Women with Osteoporosis. J Bone Miner Res. 2009. PubMed PMID: 19580469.
121. Borah B, Dufresne T, Nurre J, Phipps R, Chmielewski P, Wagner L, et al. Risedronate Reduces Intracortical Porosity in Women with Osteoporosis. J Bone Miner Res. 2009. PubMed PMID: 19580469.
122. Black DM, Delmas PD, Eastell R, Reid IR, Boonen S, Cauley JA, et al. Once-yearly zoledronic acid for treatment of postmenopausal osteoporosis. N Engl J Med. 2007;356(18):1809-22. doi: 10.1056/NEJMoa067312. PubMed PMID: 17476007.
123. Green JR, Rogers MJ. Pharmacologic profile of zoledronic acid: A highly potent inhibitor of bone resorption. Drug Develop Res. 2002;55(4):210-24. doi: 10.1002/ddr.10071. PubMed PMID: WOS:000176615900003.
124. Shuai B, Shen L, Yang Y, Ma C, Zhu R, Xu X. Assessment of the Impact of Zoledronic Acid on Ovariectomized Osteoporosis Model Using Micro-CT Scanning. PLoS One. 2015;10(7):e0132104. doi: 10.1371/journal.pone.0132104. PubMed PMID: 26148020; PubMed Central PMCID: PMCPMC4492783.
125. Lambrinoudaki I, Vlachou S, Galapi F, Papadimitriou D, Papadias K. Once-yearly zoledronic acid in the prevention of osteoporotic bone fractures in postmenopausal women.

Clin Interv Aging. 2008;3(3):445-51. PubMed PMID: 18982915; PubMed Central PMCID: PMCPMC2682377.

126. Liu M, Guo L, Pei Y, Li N, Jin M, Ma L, et al. Efficacy of zoledronic acid in treatment of osteoporosis in men and women-a meta-analysis. Int J Clin Exp Med. 2015;8(3):3855-61. PubMed PMID: 26064284; PubMed Central PMCID: PMCPMC4443118.